Effect of Aging time on Corrosion-induced Hydrogen Trapping in High-Strength Al-Alloy 2024

By
Floratos Panagiotis

THESIS
Submitted in partial fulfillment of the requirements for the degree of bachelor in mechanical Engineering

Laboratory of materials

Department of Mechanical Engineering

University Of Thessaly

Supervisor:
Dr H. Kamoutsi

Volos, 13 July, 2016

Summary

Corrosion presents a major concern to the structural integrity of aging aircraft structures and in many other applications. The effect of corrosion on the damage tolerance ability of advanced aluminum alloys calls for a very diligent consideration of the problems associated with the combined effect of corrosion and embrittling mechanisms. The present thesis is a continuation on previous worked performed in the Laboratory of Materials that connected corrosion attack with hydrogen embrittlement in aluminum alloy 2024. The present work focuses the effect of aging on corrosion-induced hydrogen trapping of Al alloy 2024 and tries to answer the key question on how the microstructural characteristics of the alloy interact with the produced hydrogen.

The experimental procedures involved the following actions: (1) thermal treatment comprising solid solution, quenching and artificial aging of the specimens (SQA), (2)accelerated corrosion testing (using the EXCO procedure), (3) detailed microstructural investigation of the evolution of corrosion damage by employing SEM and metallography, (4) hydrogen measurements by employing an in-house thermal desorption – gas chromatography system.

The major results reached are the following:

Corrosion damage in the alloy starts with pitting and develops to a network of intergranular corrosion leading to exfoliation of material. An increase in exposure time to the corrosive environment leads to increase in the depth of attack and weight loss. Similar behavior is observed with the increase of aging time during artificial aging. When aging times increase there the depth of attack and weight loss of the material also increase.

Hydrogen is produced during the corrosion process and is being trapped in distinct energy states, which correspond to different microstructural traps. These traps are activated and liberate hydrogen at different temperatures. In alloy 2024, four traps T1 to T4 were identified. Trap T1 is considered to be a reversible trap, which liberates hydrogen continuously at low temperatures. Traps T2, T3 and T4 saturate with exposure time and are considered to be irreversible. As discussed in previous work trapping state T1 corresponds to hydrogen at interstitial sites. Trapping state T4 is the strongest trap and its temperature range corresponds to the dissolution of the strengthening precipitate in alloy 2024.

It has been discussed in previous work that, T3 is associated with dislocation. Coherent / semicoherent interfaces are made up of dislocation arrays. As the particle size increases with aging time, the density of interfacial dislocation increases leading to increase in H2 with aging time. After the peak, the coherency is lost and the density of interfacial dislocation is reduced leading to a reduction of trapping hydrogen.

The study of artificial aging for alloy 2024 revealed that after solid solution and aging at 170^{o}C the maximum peak for the mechanical properties (microhardness, yield) of the alloy is reached after aging between 24 and 48 hours. The behavior of the T2 trapping state is connected to the peak hardness of the materials. Hydrogen is attracted to the strain fields associated with coherent and semi-coherent interfaces. As the particle size increases with ageing time, the hardness increases due to coherency hardening, at the same time H_2 increases. After the peak, the interfaces loose coherency and the strain fields diminish. The hardness drops and follows Orowan-mechanism. At the same time, H_2 drops since H2 is absorbed to the T4 state.

This result is a major breakthrough as it helps elucidate the effect of different precipitates on hydrogen trapping in aluminum alloy 2024, especially at state T2

Table of contents

Chapter 1. Introduction 11
Description of the problem 12
Thesis objectives 14
Thesis methodology 14
Thesis outline 14
Chapter 2 - Literature Review 15
2.1 The aircraft aluminium alloys of the 2xxx series 15
Metallurgical characteristics and hardening processes 15
Corrosion and Residual life 18
2.2 The corrosion of high-strength aluminium alloys 19
2xxx wrought alloys 19
Intergranular Corrosion 20
Stress corrosion cracking and Corrosion fatigue 21
Exfoliation corrosion 22
Accelerated corrosion tests 22
2. 3 Hydrogen Damage in Alloys 23
General classification of hydrogen damage 23
Mechanisms of Hydrogen Embrittlement 25
Hydrogen damage in Al alloys 28
Chapter 3 - Experimental procedures 31
3.1 Materials Studied 31
3.2 Microstructural characterization 32
3.3 Accelerated corrosion testing 32
3.4 Heat treatment 33
3.5 Scanning Electron Microscopy (SEM) 33
3.6 Hydrogen measurements 34
Chapter 4 – Results and Discussion 36
4.1 Metallography –Microstructural Characterization 36

Objective 36
4.2 Accelerated corrosion testing of the as received material 38
Corrosion Exposure 12 Hours 38
Corrosion Exposure 24 Hours 39
Corrosion Exposure 48 Hours 40
Corrosion Exposure 72 Hours 42
4.3 Effect of aging on the exfoliation corrosion 43
Corrosion Exposure 2 Hours 45
Corrosion Exposure 24 Hours 59
4.5 Scanning Electron Microscopy (SEM) 71
Corrosion Exposure 2 Hours 71
Corrosion Exposure 24 Hours 80
4.6 Microhardness measurements 84
4.7 Hydrogen measurements 85
Chapter 5 - Conclusions 92
Chapter 6 – Proposed Future Work 94
References 95

Table of Figures

Fig.4.1: As received aluminum alloy 2024-T351. Metallographic images in the longitudinal direction (LS plane) for magnifications (a) x100, (b) x500 and (c) x200 respectively..... 37
Fig.4.2. As received aluminum alloy 2024-T351. Metallographic images from the surface of the specimen (LT plane) for magnifications (a) x50,(b) x100,(c) x200 respectively. 37
Fig.4.3: As received aluminum alloy 2024-T351. Metallographic images in the transverse direction (ST plane) for magnifications (a) x200,(b) x100 and(c) x200 respectively. 38
Fig. 4.4: Aluminum alloy 2024-T351 after exposure to EXCO solution for 12 h. Images (a) to (b) depict exfoliation in the ST plane. Magnification is x50 respectively. Maximum depth of attack was measured 411 μm as illustrated in Table 3. 39
Fig. 4.5: Aluminium alloy 2024-T351 after exposure to EXCO solution for 24 h. Images (a) to (c) depict exfoliation in the ST plane. Magnification is x50, x100, and x50 respectively. Maximum depth of attack was measured 366 μm at fig (b) (as illustrated in table 1).Images (d) to (f) depict exfoliation in the LS plane, magnification is x50, x100, x200 and x50 respectively. Maximum depth of attack was measured 428 μm as illustrated in Table 3..... 40
Fig. 4.6.: Aluminum alloy 2024-T351 after exposure to EXCO solution for 48 h. Images (a) to (c) depict exfoliation in the ST plane. Magnification is, x200 x50, x100 respectively. Maximum depth of attack was measured 451 μm at fig (b) (as illustrated in table 1).Images (d) to (g) depict exfoliation in the LS plane, magnification is x200, x100, and x200 respectively. Maximum depth of attack was measured 217 μm at fig (f) as illustrated in Table 3. 41
Fig. 4.7: Aluminium alloy 2024-T351 after exposure to EXCO solution for 72 h. Images (a) to (c) depict exfoliation in the ST plane. Magnification is x50. Maximum depth of attack was measured 428 μm at fig (c) as illustrated in table 1.Images (d) to (f) depict exfoliation in the LS plane, magnification is x50, x50 and x100, respectively. Maximum depth of attack was measured 229 μm at fig (e) as illustrated in Table 3. 42
Fig. 4.8. Maximum depth of attack, of not heat treated aluminum alloy 2024-T351 specimens after exposure to EXCO solution..... 43
Fig. 4.9: Exfoliation corrosion for alloy 2024-T351 after aging for 30 min at T=170^{o}C. Images (a) to (c) depict exfoliation in the ST plane. Magnification is x50, x100, x200 respectively. Maximum depth of attack was measured 70,6 μm at fig (c). 45
Fig.4.10 Exfoliation corrosion for alloy 2024-T351 after aging for 1 hour at T=170^{o}C. Images (a) to (c) depict exfoliation in the ST plane. Magnification is x50, x100, x200 respectively. Maximum depth of attack was measured 82,42 μm at fig (b) as illustrated in Table 4. 46
Fig.4.11: Exfoliation corrosion for alloy 2024-T351 after aging for 2 h at T=170^{o}C. Images (a) to (c) depict exfoliation in the ST plane. Magnification is x50, x100, x200 respectively . Maximum depth of attack was measured 76,97 μm at fig (c) as illustrated in Table 4..... 47

Fig. 4.12: Exfoliation corrosion for alloy 2024-T351 after aging for 4 h at T=170ºC. Images (a) to (c) depict exfoliation in the ST plane. Magnification is x50, x100, x200 respectively .Maximum depth of attack was measured 141,21 μm at fig (b) as illustrated in Table 4. 49
Fig. 4.13: Exfoliation corrosion for alloy 2024-T351 after aging for 6 h at T=170ºC. Images (a) to (c) depict exfoliation in the ST plane. Magnification is x50, x100, x200 respectively. Maximum depth of attack was measured 126,0610 μm, at fig(a) as illustrated in Table 4. 50
Fig4.14 Exfoliation corrosion for alloy 2024-T351 after aging for 9 h at T=170ºC. Images (a) to (c) depict exfoliation in the ST plane. Magnification is x50, x100, x200 respectively. Maximum depth of attack was measured 93,94 μm, as illustrated in Table 4..... 51
Fig. 4.15. Exfoliation corrosion for alloy 2024-T351 after aging for 15 h at T=170ºC. Images (a) to (c) depict exfoliation in the ST plane. Magnification is x50, x100, x200 respectively. Maximum depth of attack was measured 114,25 μm at fig (d) as illustrated in Table 4. 52
Fig.4.16 Exfoliation corrosion for alloy 2024-T351 after aging for 24 h at T=170ºC. Images (a) to (c) depict exfoliation in the ST plane. Magnification is x50, x100, x200 respectively. Maximum depth of attack was measured 113,03 μm at fig.(c) or 208,54 μm at fig.(a) as illustrated in Table 4. 53
Fig4.17 Exfoliation corrosion for alloy 2024-T351 after aging for 48 h at T=170ºC. Images (a) to (c) depict exfoliation in the ST plane. Magnification is x50, x100, x200 respectively. Maximum depth of attack was measured 102, 46 μm at fig (b) as illustrated in Table 4. 54
Fig.4.18 . Exfoliation corrosion for alloy 2024-T351 after aging for 63 h at T=170ºC. Images (a) to (c) depict exfoliation in the ST plane. Magnification is x50, x100, x200 respectively .Maximum depth of attack was measured 186.69 μm at fig (a) as illustrated in Table 4. 55
Fig.4.19 Exfoliation corrosion for alloy 2024-T351 after aging for 98 h at T=170ºC. Images (a) to (c) depict exfoliation in the ST plane. Magnification is x50, x100, x200 respectively. Maximum depth of attack was measured 167,27 μm. Images (d) to (f) depict exfoliation in the LS plane. Magnification is x50, x100, x200 respectively. Maximum depth of attack was measured 82,92 μm. 56
Fig. 4.20. Maximun depth of attack for the different times of aging for the ST and LS plane after 2 hours of EXCO exposure. 57
Fig. 4.21. Weight loss of the specimens, were introduced in the EXCO solution for 2 hours after aging in different conditions. 58
Fig. 4.22.Weight loss percentage of the specimens, were introduced in the EXCO solution for 2 hours after aging in different conditions. 58
Fig.4.23: Exfoliation corrosion of 24h, for aluminum alloy 2024-T351, after aging for 30 min at T=170oC. Image (a) depicts exfoliation in the ST plane. Magnification is x200. Maximum depth of attack was measured 118,78 μm at fig (a) .Images (d) to (f) depict exfoliation in the LS plane. Magnification is x50, x100, x200 respectively. Maximum depth of attack was measured 54,54 μm at fig (b) 59

Fig.4.24: Exfoliation corrosion of 24h, for aluminum alloy 2024-T351, after aging for 1 hour at T=170°C. Images (a) to (c) depict exfoliation in the ST plane. Magnification is x50, x100, x200 respectively. Maximum depth of attack was measured 165,85 μm at fig(a).Images (d) to (f) depict exfoliation in the LS plane. Magnification is x50, x100, x200 respectively. Maximum depth of attack was measured 220 μm at fig (e). 60
Fig.4.25: Exfoliation corrosion of 24h, for aluminum alloy 2024-T351, after aging for 2 hours at T=170°C. Images (a) to (c) depict exfoliation in the ST plane. Magnification is x50, x100, x200 respectively. Maximum depth of attack was measured 158,53 μm at fig (a).Images (d) to (f) depict exfoliation in the LS plane. Magnification is x50, x100, x200 respectively. 61
Fig.4.26: Exfoliation corrosion of 24h, for aluminum alloy 2024-T351, after aging for 4 hours at T=170°C. Images (a) to (c) depict exfoliation in the ST plane. Magnification is x50, x100, x200 respectively. Images (d) to (f) depict exfoliation in the LS plane. Magnification is x50, x100, x200 respectively. 62
Fig.4.27: Exfoliation corrosion of 24h, for aluminum alloy 2024-T351, after aging for 6 hours at T=170°C. Images (a) to (c) depict exfoliation in the ST plane. Magnification is x50, x100, x200 respectively. Images (d) to (f) depict exfoliation in the LS plane. Magnification is x50, x100, x200 respectively. 63
Fig.4.28: Exfoliation corrosion of 24h, for aluminum alloy 2024-T351, after aging for 9 hours at T=170°C. Images (a) to (c) depict exfoliation in the ST plane. Magnification is x50, x100, x200 respectively. Images (d) to (f) depict exfoliation in the LS plane. Magnification is x50, x100, x200 respectively. 64
Fig.4.29: Exfoliation corrosion of 24h, for aluminum alloy 2024-T351, after aging for 15 hours at T=170°C. Images (a) to (c) depict exfoliation in the ST plane. Magnification is x50, x100, x200 respectively. Images (d) to (f) depict exfoliation in the LS plane. Magnification is x50, x100, x200 respectively. 65
Fig.4.30: Exfoliation corrosion of 24h, for aluminum alloy 2024-T351, after aging for 24 hours at T=170°C. Images (a) to (c) depict exfoliation in the ST plane. Magnification is x50, x100, x200 respectively. Images (d) to (f) depict exfoliation in the LS plane. Magnification is x50, x100, x200 respectively. 66
Fig.4.31: Exfoliation corrosion of 24h, for aluminum alloy 2024-T351, after aging for 48 hours at T=170°C. Images (a) to (c) depict exfoliation in the ST plane. Magnification is x50, x100, x200 respectively. Images (d) to (f) depict exfoliation in the LS plane. Magnification is x50, x100, x200 respectively. 67
Fig.4.32: Exfoliation corrosion of 24h, for aluminum alloy 2024-T351, after aging for 63 hours at T=170°C. Images (a) to (c) depict exfoliation in the ST plane. Magnification is x50, x100, x200 respectively. Images (d) to (f) depict exfoliation in the LS plane. Magnification is x50, x100, x200 respectively. 68

Fig.4.33: Exfoliation corrosion of 24h, for aluminum alloy 2024-T351, after aging for 98 hours at T=170°C. Images (a) to (c) depict exfoliation in the ST plane. Magnification is x50, x100, x200 respectively. Images (d) to (f) depict exfoliation in the LS plane. Magnification is x50, x100, x200 respectively. 69
Fig. 4.34. Weight loss of the specimens, were introduced in the EXCO solution for 24 hours after aging in different conditions. 70
Fig. 4.35. Weight loss percentage of specimens, were introduced in the EXCO solution for 24 hours after aging in different conditions. 70
Fig. 4.36 : SEM topographies of alloy 2024-T351 after aging for 30 min at T=170°C and 2 hours exposure in the EXCO solution. Magnification is (a) x200, (b) x500, (c) x750, (d)x1500, (e)x5000 and (f) x10000 respectively 71
Fig. 4.37: SEM topographies of alloy 2024-T351 after aging for 1 h at T=170°C and 2 hours exposure in the EXCO solution. Magnification is (a) x500, (b) x750, (c) x1000, (d) x7500 and (e) 10000 respectively. 72
Fig. 4.38 :SEM topographies of alloy 2024-T351 after aging for 2 h at T=170°C and 2 h exposure in the EXCO solution. Magnification is (a) x200, (b) x500 and (c) x1000 respectively 73
Fig. 4.39 : SEM topographies of alloy 2024-T351 after aging for 6 h at T=170°C and 2 hours exposure in the EXCO solution. Magnification is (a)x100 and (b) x200respectively. 74
Fig. 4.40: SEM topographies of alloy 2024-T351 after aging for 9 h at T=170°C and 2 hours exposure in the EXCO solution. Magnification is x200, x500, x1500, x2000, x3500 and x7500 respectively. 75
Fig. 4.41: SEM topographies of alloy 2024-T351 after aging for 15 h at T=170°C and 2 hours exposure in the EXCO solution. Magnification is x200, x500, x750, x1000 and x3500 respectively. 76
Fig. 4.42 : SEM topographies of alloy 2024-T351 after aging for 15 h at T=170°C and 2 hours exposure in the EXCO solution. Magnification is (a) x35, (b) x200, (c) x500, (d) x1000, (e) x5000 and (f) x7500 respectively. 77
Fig. 4.43: SEM topographies of alloy 2024-T351 after aging for 48 h at T=170°C and 2 hours exposure in the EXCO solution. Magnification is (a) x200, (b) and (c) x500 respectively. 77
Fig. 4.44: SEM topographies of alloy 2024-T351 after aging for 63 h at T=170°C and 2 hours exposure in the EXCO solution. Magnification is (a) x200, (b) x350, (c) x500, (d) x1000, (e) x1500 and (f) x2000 respectively. 78
Fig. 4.45: SEM topographies of alloy 2024-T351 after aging for 98 h at T=170°C and 2 hours exposure in the EXCO solution. Magnification is (a) x500 and (b) x1500 respectively. 79
Fig. 4.46: SEM topographies of alloy 2024-T351 after aging for 30 min at T=170°C and 24 hours exposure in the EXCO solution. Magnification is (a) x15, (b) x200, (c) x500, (d) x750, (e) x1500 and (f) x3500 respectively. 80

Fig. 4.47: SEM topographies of alloy 2024-T351 after aging for 1 h at T=170^{o}C and 24 hours exposure in the EXCO solution. Magnification is (a) x50, (b) x200, (c) x500, (d) x750, (e) x1000 and (f) x3500 respectively. 81
Fig. 4.48: SEM topographies of alloy 2024-T351 after aging for 2 h at T=170^{o}C and 24 hours exposure in the EXCO solution. Magnification is (a) x50, (b) x200, (c) x350, (d) x500, (e) x750 and (f) x1500 respectively. 82
Fig. 4.49: SEM topographies of alloy 2024-T351 after aging for 4 h at T=170^{o}C and 24 hours exposure in the EXCO solution. Magnification is (a) x150, (b) x200, (c) x350,(d) x500 and (e) 1500 respectively. 83
Fig. 4.50: Microhardness profile of 2024-T351 versus time of aging. The aging was performed at T=170^{o}C for duration of 30 min, 1 h, 2 h, 4 h,6 h, 9 h, 15 h , 24 h, 48 h, 63 h and 98 respectively. 84
Fig. 4.51: Microhardness profile of 2024-T351 versus time of aging. The aging was performed at T=170^{o}C for duration of 30 min, 1 h, 2 h, 4 h,6 h, 9 h, 15 h , 24 h, 48 h, 63 h and 98 respectively. 85
Fig. 52 : Spectrum of hydrogen evolved from the specimens in the T351 condition after (a) 12 h (b)24 h, (c) 48 h and (d) 72 h exposure to the EXCO solution. 86
Fig. 53: Spectrum of hydrogen evolved from the solution treated, quenched and aged (SQA) specimens after 24 h in the EXCO solution. The specimens were artificially aged for 30 min, 1 h, 2 h, 4 h, 6 h, 9 h, 15 h , 24 h, 48 h, 63 h and 98 respectively. 88
Fig. 54: Spectrum of hydrogen evolved from the solution treated, quenched and aged (SQA) specimens after 24 h in the EXCO solution. The specimens were artificially aged for 30 min, 1 h, 2 h, 4 h, 6 h, 9 h respectively. 88
Fig. 55: Spectrum of hydrogen evolved from the solution treated, quenched and aged (SQA) specimens after 24 h in the EXCO solution. The specimens were artificially aged for 15 h, 24 h, 48 h, 63 h and 98 respectively. 89
Fig. 56: Total hydrogen content of corroded specimens in the T1 trapping state as a function of aging time (24 hours in the exfoliation solution). 89
Fig. 57: Total hydrogen content of corroded specimens in the T2 trapping state as a function of aging time (24 hours in the exfoliation solution). 90
Fig. 58: Total hydrogen content of corroded specimens in the T3 trapping state as a function of aging time (24 hours in the exfoliation solution). 90
Fig. 59: Total hydrogen content of corroded specimens in the T4 trapping state as a function of aging time (24 hours in the exfoliation solution). 91

Acknowledgments

I feel the need to express my immense gratitude to my family, and separately to each member. My mother, my sister, my father, my grandmother and my grandfather for their support throughout the duration of my studies.

I would also like to thank my supervisor Hellen Kamoutsi and Professor Gregory N. Haidemenopoulos, giving me the opportunity to deal with such an interesting topic. I would also like to thank them for their assistance, guidance and helpful advice they gave me. I would also like to especially thank Mrs. Helen Kamoutsi for unlimited patience in conclusion; I would like to thank everyone who contributed to this difficult task each in his own way.

Chapter 1. Introduction

Description of the problem

Corrosion presents a major concern to the structural integrity of aging aircraft structures. As the time of an aircraft structure in service increases, there is a growing probability that corrosion will interact with other forms of damage, such as single fatigue cracks or multiple-site damage in the form of widespread cracking at regions of high-stress gradients; it can result in loss of structural integrity and may lead to fatal consequences. Thus, the effect of corrosion on the damage tolerance ability of advanced aluminium alloys calls for a very diligent consideration of the problems associated with the combined effect of corrosion and embrittling mechanisms. There has been, an increasing attention of basic research and development concerning structural integrity taking into account the related corrosion aspects (1-3). It has been realized that the establishment of damage functions for quantifying the simultaneous accumulation of corrosion and fatigue-induced damage is very complex and difficult. Therefore, despite the advancements in modelling fatigue crack growth (4-7) and multiple-site damage phenomena (1-3), the assessment of structural degradation in aging aircraft is still relying heavily on test data. To face the corrosion- induced structural degradation issue, available data usually refer to accelerated laboratory corrosion tests and, more rarely, to in-nature atmospheric or marine exposure corrosion tests.

With the exception of the atmospheric corrosion test where, according to the relevant specification the tensile properties of corroded specimens are measured as well, these tests are used for evaluating the corrosion susceptibility of the materials by measuring weight loss and characterizing depth and type of corrosion attack. The above methodology toward understanding corrosion susceptibility of a material does not relate corrosion to their effect on the materials mechanical behavior and residual properties. Yet, it is exactly these missing data that are needed to face structural integrity problems of corroded aircraft components. Corrosion- induced mechanical degradation studies have been based mainly on the results of stress corrosion cracking tests (8, 9) or, more rarely on the results of fatigue tests performed in the presence of a corrosive environment (1-3). Both types of tests provide useful results; they refer, however, to the case where a material is loaded in a corrosive environment but not to situations where a corroded material is subjected to mechanical loads. Present-day considerations of the corrosion-induced structural degradation relate the presence of corrosion with a decrease of the load-bearing capacity of the corroded structural member (2, 10).

This decrease is associated with the presence of corrosion notches that lead to local increase of stress promoting fatigue crack initiation as well; in addition, corrosion-induced reduction of the

members' load-bearing thickness which, in the case of the thin alloy skin sheets, may be essential, can lead to appreciable increase of stress gradients (10). Corrosion-induced material embrittlement is not accounted for. The above consideration of the corrosion-induced structural integrity issue is consistent with the classical understanding of the corrosion attack of aluminum alloys as the result of complex oxidation processes at the materials surface.

The above considerations gain particular importance if the so-called "aging aircraft" issue is considered. The aging aircraft has accumulated corrosion damage over the service life and its residual life depends on possible degradation stemming from corrosion-induced embrittling mechanisms.

There are three key questions regarding this issue:

1. Is there a corrosion-induced degradation of ductility, which in turn degrades damage tolerance and the residual life of aerostructures?
2. What is the underlying corrosion-induced embrittling mechanism?
3. What is the effect of the microstructural characteristics of the material on hydrogen trapping.

The answer to the first question has been given by the long series of experiments, conducted at the Univ. of Patras (11, 12), on mechanical testing of precorroded (in EXCO) alloy 2024. It was shown that (i) degradation of ductility increases with corrosion exposure time and (ii) removal of the corrosion layer restores strength but not ductility. These results indicated the operation of a bulk corrosion-induced embrittlement mechanism. The second question was answered by previous work performed in the Laboratory of Materials (13-15). Hydrogen is produced during the corrosion process and is being trapped in distinct energy states, which correspond to different microstructural traps. These traps are activated and liberate hydrogen at different temperatures. In alloy 2024, four traps T1 to T4 were identified. Trap T1 is considered to be a reversible trap, which liberates hydrogen continuously at low temperatures. Traps T2, T3 and T4 saturate with exposure time and are considered to be irreversible. The hydrogen front advances with the corrosion front, so hydrogen penetrates deep in the material through the intergranular paths generated by the corrosion process. Then hydrogen diffuses further in the material establishing a hydrogen-affected zone beneath the corrosion depth of attack.

As far as the last question is concerned it was partially answered in the previous work (13-15), where. Trapping state T1 was attributed to hydrogen at interstitial sites. Trapping state T4 as the strongest trap was attributed to the strengthening precipitate S in alloy 2024 and state T3 was connected with dislocations present in the material.

Thesis objectives

In view of the above considerations, the present thesis tries to further elucidate the third question posted above, i.e. what is the effect of the microstructural characteristics of the material on hydrogen trapping?

The thesis objectives are therefore the following:

1. To establish a link, if any, between corrosion and precipate population.
2. To establish a link, if any, between precipate population and hydrogen uptake and trapping.

Thesis methodology

Research was focused on aircraft aluminum alloy 2024 in the T351 temper. The experimental procedures involved the following actions:

(1) Heat treatments,

(2) Accelerated corrosion testing (using the EXCO procedure),

(3) Detailed microstructural investigation of the evolution of corrosion damage by employing stereo-microscopy, SEM and metallography,

(4) Hydrogen measurements by employing an in-house thermal desorption – gas chromatography system

Thesis outline

The thesis outline is as follows

Chapter2 - Literature review

Chapter3 - Experimental procedures

Chapter 4 - Results and Discussion

Chapter 5 - Conclusions

Chapter 6 - Proposed Future Work

Chapter 2 - Literature Review

The bibliographic review presented in the following pages, in addition to presenting the state of the art for the subject, aims at a short discussion of the key subjects of this thesis. The review starts with a brief introduction on Al-alloys (age hardening, damage tolerance). It continues with a discussion of corrosion of 2xxx alloys, emphasizing the forms of corrosion (pitting, intergranular corrosion, SCC and exfoliation). Finally there is a critical discussion of hydrogen damage in alloys and hydrogen embrittlement of Al-alloys.

2.1 The aircraft aluminium alloys of the 2xxx series

Metallurgical characteristics and hardening processes

The strength of aluminum alloys, rivals that of mild carbon steel, and can approach 700 MPa. Combination of high strength and light weight makes aluminum especially well suited to aircraft industry. Alloy 2024 T3, because of its high mild carbon steel strength-to-density ratio and corrosion resistance is used in the aircraft industry for numerous applications such as fuselage, door skin and trailing edge panels.

This alloy belongs in the 2xxx series, of wrought aluminum alloys; they are usually referred to as aircraft alloys. The primary alloying element for this group is copper, which produces high strength but reduced corrosion resistance (Table 1). These alloys were among the first aluminum alloys developed and were originally called duralumin. Alloy 2024 is perhaps the best known and most widely used alloy in the aircraft industry.

In some cases, alloys (such as 2024) are protected by a thin coating of pure aluminum or corrosion-resistant aluminum alloy, the resulting product is called al-clad. This cladding is metallurgically bonded to one or both sides of the sheet or plate and may be 1.5-10% of its overall thickness. The cladding alloy is chosen so that it is anodic to the core alloy and protects it from corrosion. Any corrosion that occurs proceeds only to the cladding-core interface and then spreads laterally, making cladding very effective in protecting thin materials.

Heat treatable aluminum alloy like 2024 own his remarkable mechanical properties to age hardening. Heat treatment normally involves the following stages:

(1) Solution treatment at a relatively high temperature within the single-phase region in order to dissolve the alloying elements.
(2) Rapid cooling or quenching, usually to room temperature, to obtain a supersaturated solid solution (SSSS) of these elements in aluminum.

(3) Controlled decomposition of the SSSS to form a finely dispersed precipitate, usually by ageing for specified times.

Table 1: Wrought Alloy Designation System and Characteristics.

Series Number	Primary Alloying Element	Relative Corrosion Resistance	Relative Strength	Heat Treatment
1xxx	None	Excellent	Fair	Non-heat-treatable
2xxx	Copper	Fair	Excellent	Heat treatable
3xxx	Manganese	Good	Fair	Non-heat-treatable
4xxx	Silicon	Fair	Fair	Non-heat-treatable
5xxx	Magnesium	Good	Good	Non-heat-treatable
6xxx	Magnesium and silicon	Good	Good	Heat-treatable
7xxx	Zinc	Fair	Excellent	Heat-treatable

The complete decomposition of an SSSS is a complex process which may involve several stages. Typically, Guinier-Preston (GP) zones and an intermediate precipitate may form prior to the equilibrium phase and may also coexist with the equilibrium phase. The GP zones are ordered, solute-rich clusters of atoms which may be only one or two atom planes in thickness. They retain the structure of the matrix and are coherent with it, although they produce appreciable elastic strains. Their formation requires movements of atoms over relatively short distances so that they are very finely dispersed in the matrix with densities which may be as high as 10^{17} to 10^{18} cm^{-3}. The intermediate precipitate is normally much larger in size than a GP zone and is only partly coherent with the lattice planes of the matrix. It has a definite composition and crystal structure which may differ only slightly from those of the equilibrium precipitate. In some alloys, the intermediate precipitate may be nucleated from, or at, the sites of stable GP zones. In others this phase nucleates heterogeneously at lattice defects such as dislocations. Formation of the final equilibrium precipitate involves complete loss of coherency with the parent lattice. It forms only at relatively high aging temperatures and, because it is coarsely dispersed, little hardening results. Maximum hardening in commercial alloys occurs with the formation of a critical dispersion of GP zones, or an intermediate precipitate, or both. In some cases the alloys are cold worked (e.g. by stretching 5%) after quenching and before aging, thus

increasing dislocation density and providing more sites at which heterogeneous nucleation of intermediate precipitates may occur. The precipitation sequence of Al-Cu, and Al-Cu-Mg (16-28) is illustrated in Table 2. If precipitate particles are large and widely spaced, they can be readily bypassed by moving dislocations which bow out between them by a mechanism first proposed by Orowan (29). Loops of dislocations are left around the particles. The yield strength of the alloy is low but the rate of work-hardening is high, and plastic deformation tends to be spread more uniformly throughout the grains. Accompanying the formation of the intermediate precipitate is the development of wider, precipitate-free zones adjacent to grain boundaries. These zones are relatively weak with respect to the age-hardened matrix and may deform preferentially leading to high stress concentrations at triple points which, in turn, may cause premature cracking.

Table 2: The precipitation sequence of 2xxx alloys (29).

Alloy	Precipitates	Remarks
Al-Cu	GP zones as thin plates on {100} θ" (formerly GP zones)	Probably single layers of copper atoms on $\{100\}_\alpha$ Coherent, probably two layers of copper atoms separated by three layers of aluminium atoms. May be nucleated at GP zones
	θ' tetragonal $A1_2Cu$ a = 0.404 nm c = 0.580 nm	Semi-coherent plates nucleated at dislocations Form on $\{100\}_\alpha$
	θ body-centred tetragonal $A1_2Cu$ a = 0.607 nm c = 0.487 nm	Incoherent equilibrium phase May nucleate at surface of θ'
Al-Cu-Mg	GP (Cu, Mg) zones as rods along <100>	GP zones form very rapidly in most compositions aged at elevated temperatures. Sometimes known as GPB zones
	S' orthorhombic $A1_2CuMg$ c = 0.718 run b = 0.925 nm a = 0.404 nm	Semi-coherent and nucleated at dislocations Forms as laths in {210}, along <001>,
	S orthorhombic $A1_2CuMg$ a = 0.400 nm b = 0.923 nm c = 0.714 nm	Incoherent equilibrium phase, probably transforms from S'. Note that precipitates from the Al-Cu system can also form in compositions with high Cu:Mg ratios

If precipitate particles are large and widely spaced, they can be readily bypassed by moving dislocations which bow out between them by a mechanism first proposed by Orowan (29). Loops of dislocations are left around the particles. The yield strength of the alloy is low but the rate of work-hardening is high, and plastic deformation tends to be spread more uniformly throughout the grains. Accompanying the formation of the intermediate precipitate is the development of wider, precipitate-free zones adjacent to grain boundaries. These zones are relatively weak with respect to the age-hardened matrix and may deform preferentially leading to high stress concentrations at triple points which, in turn, may cause premature cracking.

Corrosion and Residual life

The advantage of the damage tolerant design philosophy is obviously the ability to treat cracked objects in a direct and appropriate fashion. The previous methods only allow for the immediate removal of cracked structure. Use of the stress-intensity values and appropriate data (properties) allows the number of cycles of crack growth over a range of crack sizes to be estimated and fracture to be predicted. The clear tie of crack size, orientation, and geometry to non-destructive evaluation (NDE) is also a plus. Disadvantages are: possibly computationally intensive stress-intensity factor determinations, greater complexity in development and modelling of property data, and the necessity to perform numerical integration to determine crack growth. In addition, the predicted lives are considerably influenced by the initial crack size used in the calculation, requiring quantitative development of probability of detection for each type of NDE technique employed. Related to the initial crack size consideration is the inability of this approach to model effectively that the component was actually suitable for modelling as a continuum, which eliminates the so-called "initiation" portion of the part life. It becomes obvious that complete knowledge of prexisting cracks and their propagating paths must be available.

A major factor introducing cracks in materials is corrosion that produces cracking of metals as a result of exposure to the aggressive environment. This cracking may take the form of relatively slow, stable crack extension or, as is often the case, unpredictable catastrophic fracture. Investigations involving information on the residual mechanical properties of a structural material following exposure to corrosive environment were conducted by Pantelakis et al. (11, 12), and the effect of corrosion and hydrogen embrittlement on the mechanical behavior of aluminum aircraft alloys was investigated. The work was based on extended, experimental data of the aircraft aluminum alloy 2024. Evaluation of corrosion resistance was performed based on the metallography. As well, the obtained results were discussed under the viewpoint of hydrogen embrittlement.

2.2 The corrosion of high-strength aluminium alloys

It has become clear that a profound understanding and efficient control of corrosion phenomena is essential, for the reliable extension of aircraft service life.

Aluminum, as indicated by its position in the electromotive force series, is a thermodynamically reactive metal; among structural metals, only beryllium and magnesium are more reactive. Aluminum owes its excellent corrosion resistance to the protective oxide film that is bonded strongly to its surface and that, if damaged, reforms immediately in most environments. The conditions for thermodynamic stability of the oxide film are expressed by the Pourbaix (electrochemical potential versus pH) diagram. Aluminum is passive (protected by its oxide film) in the pH range of about 4 to 8.5. The limits of this range, however, vary somewhat with temperature, with the specific form of oxide film present, and with the presence of substances that can form soluble complexes or insoluble salts with aluminum. Beyond the limits of its passive range, aluminum corrodes in aqueous solutions because its oxides are soluble in many acids and bases, yielding Al^{3+} ions in the former and $A1O^{-}_{2}$ (aluminate) ions in the latter.

Corrosion of aluminum in the passive range is localized, usually manifested by random formation of pits. For aluminum, pitting corrosion is most commonly produced by halide ions, of which chloride (Cl^{-}) is the most frequently encountered in service. Pitting of aluminum in halide solutions open to the air occurs because, in the presence of oxygen, the metal is readily polarized to its pitting potential. Generally, aluminum does not develop pitting in aerated solutions of most nonhalide salts because its pitting potential in these solutions is considerably more noble (cathodic) than in halide solutions, and it is not polarized to these potentials in normal service.

Because of the electrochemical nature of corrosion processes, relationships among solution potentials of different aluminum alloys, as well as between potentials of aluminum alloys and those of other metals, are of considerable importance. Furthermore, the solution-potential relationships among the microstructural constituents of a particular alloy significantly affect its corrosion behavior. Compositions of solid solutions and additional phases, as well as amounts and spatial distributions of the additional phases, may affect both the type and extent of corrosion.

2xxx wrought alloys

2xxx wrought alloys, in which copper is the major alloying element, are less corrosion-resistant than alloys of other series that contain much lower amounts of copper. Electrochemical effects on corrosion can be stronger in these alloys than in alloys of many other types because of two factors: greater change in electrode potential with variations in the amount of copper in solid solution; and, under some conditions, the presence of non-uniformities in solid-solution concentration. However, the fact that general corrosion resistance decreases with increasing

copper content is not primarily attributable to these solid-solution or second-phase solution-potential relationships, but rather to galvanic cells created by formation of minute copper particles or films deposited on the alloy surface as a result of corrosion. As corrosion progresses, copper ions, which initially go into solution, replace onto the alloy to form metallic copper cathodes. The reduction of copper ions and the increased efficiency of O_2 and H^+ reduction reactions in the presence of copper increase the corrosion rate.

It is generally acceptable that pitting constitutes the precursor for every other type of corrosion; the creation of pits is virtually the first stage of corrosion. Pits first appear in regions where surface abnormalities with respect to the matrix are present. For example on grain boundaries, where during the precipitation of intermetallic second phase particles, a neighbouring area poor in compound elements is created. If the boundary precipitates are anodic with respect to the matrix and the precipitate free zone, then these particles are selectively dissolved. In the opposite case the neighbouring area poor in compound elements is attacked (30). On grain boundaries of an alloy belonging to the 2xxx series, for example, they selectively create anodic regions that make the material sensitive to corrosion.

Other researchers have shown that the anodic nature of grain boundaries can be attributed to the segregation in these regions, with regard to the grain interior. Guillaumin et al. observed on grain boundaries of 2024 acicular precipitates Al_2CuMg as well as particles of S phase (31). Generally galvanic cells are created between regions rich in Cu (S phase) and neighbouring regions poor in compound elements. From studies in different corrosive environments it was concluded that Cl^- ion is the most aggressive (32). As a result of the severe presence of Cl^- ions, the marine environment is highly corrosive (33).

Intergranular Corrosion

Another form of corrosion is intergranular (intercrystalline) corrosion, which is selective attack of grain boundaries or closely adjacent regions without appreciable attack of the grains themselves. Intergranular corrosion is a generic term that includes several variations associated with different metallic structures and thermomechanical treatments. Intergranular corrosion is caused by potential differences between the grain-boundary region and the adjacent grain bodies. The location of the anodic path varies with the different alloy systems: In 2xxx series alloys, it is a narrow band on either side of the boundary that is depleted in copper. Because intergranular corrosion is involved in SCC of aluminum alloys, it is often presumed to be more deleterious than pitting or general corrosion. However, in alloys that are not susceptible to SCC (e.g., the 6xxx series alloys) intergranular corrosion is usually no more severe than pitting corrosion and tends to decrease with time. For equal depth of corrosion, its effect on strength is also no greater than that of pitting corrosion, although fatigue cracks may be more likely to initiate at areas of intergranular corrosion than at random pits.

Stress corrosion cracking and Corrosion fatigue

Stress-corrosion cracking (SCC) is a term used to describe service failures in engineering materials that occur by slow environmentally induced crack propagation. The observed crack propagation is the result of the combined and synergistic interaction of mechanical stress and corrosion reactions. This is a simple definition of a complex subject, and like most simplifications, it fails to identify the boundaries of the subject. Environments that cause SCC are usually aqueous and can be condensed layers of moisture or bulk solutions. Typically, SCC of an alloy is the result of the presence of a specific chemical species in the environment. Thus, chloride ions cause cracking in stainless steels and aluminum alloys (34, 35).Only aluminum alloys that contain appreciable amounts of soluble alloying elements, primarily copper, magnesium, silicon, and zinc, are susceptible to SCC. For most commercial alloys, tempers have been developed that provide a high degree of immunity to SCC in most environments.

Stress-corrosion cracking in aluminum alloys is characteristically intergranular. According to the electrochemical theory, this requires a condition along grain boundaries that makes them anodic to the rest of the microstructure so that corrosion propagates selectively along them. Such a condition is produced by localized decomposition of solid solution, with a high degree of continuity of decomposition products along the grain boundaries. The most anodic regions may be either the boundaries themselves (most commonly, the precipitate formed in them) or regions adjoining the boundaries that have been depleted of solute.

In 2xxx alloys, the solute-depleted regions are the most anodic. The most anodic grain-boundary regions in other alloys have not been identified with certainty. Strong evidence for the presence of anodic regions and for the electrochemical nature of their corrosion in aqueous solutions is provided by the fact that SCC can be greatly retarded, if not eliminated, by cathodic protection. For alloys requiring microstructural control to avoid susceptibility, resistance is obtained by using treatments that produce precipitate throughout the microstructure, because precipitate always forms along boundaries, and its formation then usually cannot be prevented (36-40).

According to electrochemical theory, susceptibility to intergranular corrosion is a prerequisite for susceptibility to SCC, and treatment of aluminum alloys to improve resistance to SCC also improves their resistance to intergranular corrosion. For most alloys, however, optimum levels of resistance to these two types of failure require different treatments and resistance to intergranular corrosion is no a reliable indication of resistance to SCC.

Corrosion fatigue occurs in metals as a result of the combined action of a cyclic stress and a corrosive environment. Corrosion fatigue is dependent on the interactions among loading, environmental, and metallurgical factors. For a given material, the fatigue strength (or fatigue life at a given maximum stress value) generally decreases in the presence of an aggressive

environment. The effect varies widely, depending primarily on the particular metal-environment combination. The environment may affect the probability of fatigue crack initiation, the fatigue crack growth rate, or both.

Exfoliation corrosion

In certain tempers, wrought products of aluminum alloys are subject to corrosion by exfoliation, which is sometimes described as lamellar, layer, or stratified corrosion. In this type of corrosion, attack proceeds along selective subsurface paths parallel to the surface. Layers of uncorroded metal between the selective paths are split apart and pushed above the original surface by the voluminous corrosion product formed along the paths of attack. Because it can be detected readily at an early stage and is restricted in depth, exfoliation does not cause unexpected structural failure, as does SCC.

Exfoliation occurs predominantly in products with markedly directional structures, in which highly elongated grains form platelets that are thin relative to their length and width. Susceptibility to this type of corrosion may result from the presence of aligned intergranular or subgrain boundary precipitates or from aligned strata that differ slightly in composition. The intensity of exfoliation increases in slightly acidic environments or when the aluminum is coupled to a cathodic dissimilar metal. Exfoliation is not accelerated by stress and does not lead to SCC. Alloys most susceptible to exfoliation are the heat-treatable 2xxx and 7xxx alloys and certain cold-worked 5xxx alloys. Exfoliation is primarily caused by unfavorable distribution of precipitate. The processing to eliminate this form of attack promotes either more uniform precipitation within grains or a more advanced stage of precipitation. Thus, increases in precipitation heat-treating time or temperature are as effective in reducing susceptibility to exfoliation as they are in reducing susceptibility to SCC.

The occurrence of exfoliation in susceptible materials is remarkably influenced by environmental conditions. For example, forged truck wheels made of an aluminum-copper alloy (2024-T4) give corrosion-free service for many years in the warm climates of the southern and western United States, but exfoliate severely in only one or two years in the northern states, where de-icing salts are used on the highways during the winter months. Exfoliation corrosion initiates between bimetallic couples and progresses along grain boundaries as an intergranular crack. This intergranular crack widens into a crack plane and enlarges into multiple crack planes. Corrosive oxides press outward against the adjacent metal, thus producing a pattern of delamination (41, 42).

Accelerated corrosion tests

Accelerated laboratory tests do not precisely predict long-term corrosion behavior. However, they are frequently used when answers are needed quickly in the development of new materials. For this reason, accelerated tests are used to screen candidate alloys before

conducting atmospheric exposures or other field tests. They are also sometimes used for quality control tests. Several new laboratory tests for exfoliation corrosion have been standardized in recent years under the jurisdiction of American Society for Testing and Materials (ASTM) Committee G- 1 on the corrosion of metals.

ASTM standard G 34 provides an accelerated exfoliation corrosion test for 2xxx and 7xxx alloys through the continuous immersion of test materials in an aqueous solution containing 4 M NaCl, 0.5 M potassium nitrate (KNO_3), and 0. 1 M HNO_3 at 25 ºC. Susceptibility to exfoliation is determined by visual examination, using performance ratings established by reference standard photographs (43). This method, known as the EXCO test, is primarily used in research and development and quality control of such mill products as sheet and plate. However, it should not be considered the optimal method for quality acceptance. Rather, this method provides a useful prediction of the exfoliation behavior of these alloys in various types of outdoor service, especially in marine and industrial environments. The test solution is very corrosive and is meant to represent the more severe type of environmental exposure.

It remains to be determined whether correlations can be established between EXCO test ratings and practical service conditions for given alloy. For example, it has been reported that samples of 7xxx alloys rated EA (superficial exfoliation) or P (pitting) in 48 h EXCO test did not develop more than superficial exfoliation (EA rating) during six to nine-year exposures to seacoast atmospheres, while materials rated as EC or E (severe and very severe exfoliation, respectively) developed severe exfoliation within or one to seven years at the seacoast.

2. 3 Hydrogen Damage in Alloys

General classification of hydrogen damage

Hydrogen damage is a form of environmentally assisted failure that results most often from the combined action of hydrogen penetration and residual or applied tensile stress. Hydrogen damage to specific alloys or groups of alloys manifests itself in many ways, such as cracking, blistering, hydride formation and loss in tensile ductility. For many years, these failures have been collectively termed hydrogen embrittlement and have been confused with other forms of environmentally induced failure; this term persists even though it is improperly used to describe a multitude of failure modes involving hydrogen, several of which do not demonstrate the classical features of embrittlement (that is reduced load carrying capability or fracture below the yield strength).

The specific types of hydrogen damage have been categorized in order to enhance the understanding of the factors that affect this behavior in alloys and to provide a basis for development and analysis of theories regarding different hydrogen damage mechanisms.

Blistering occurs predominantly in low-strength alloys when atomic hydrogen diffuses to internal defects, such as laminations or nonmetallic inclusions, and then precipitates as molecular hydrogen (H_2). The pressure of molecular hydrogen can attain such high values that localized plastic deformation of the alloy occurs, forming a blister that often ruptures. Blisters are frequently found in low-strength steels that have been exposed to aggressive corrosive environments (such as H_2S) or cleaned by pickling (44). Shatter cracks, flakes, and fish eyes are features common to hydrogen damage in forgings, weldments, and castings. They are attributed to hydrogen pickup during melting operations when the melt has a higher solubility for hydrogen than the solid alloy. During cooling from the melt, hydrogen diffuses to and precipitates in voids and discontinuities, producing the features that result from the decreased solubility of hydrogen in the solid metal (45).

Hydrogen environment embrittlement occurs during the plastic deformation of alloys in contact with hydrogen bearing gases or a corrosion reaction and is therefore strain rate dependent. The degradation of the mechanical properties of ferritic steels, nickel-base alloys, titanium alloys, and metastable austenitic stainless steels is greatest when the strain rate is low and the hydrogen pressure and purity are high.

Hydrogen stress cracking often referred to as hydrogen-induced cracking or static fatigue is characterized by the brittle fracture of a normally ductile alloy under sustained load in the presence of hydrogen. Most often, fracture occurs at sustained loads below the yield strength of the material. Hydrogen stress cracking is associated with absorption of hydrogen and a delayed time to failure (incubation time) during which hydrogen diffuses into regions of high triaxial stress. The catastrophic cracking of steels in hydrogen sulfide (H_2S) environments referred to as sulfide stress cracking is a special case of hydrogen stress cracking (44).

Hydrogen attack is a high-temperature form of hydrogen damage that occurs in carbon and low-alloy steels exposed to high pressure hydrogen at high temperatures for extended time. Hydrogen enters the steel and reacts with carbon either in solution or as carbides to form methane gas, which may result in the formation of cracks and fissures or may simply decarburize the steel resulting in a loss in strength of the alloy. This form of damage is temperature dependent, with a threshold temperature of approximately 200 ^{o}C (46, 47).

Loss in tensile ductility was one of the earliest recognized forms of hydrogen damage. Significant decreases in elongation and reduction in area are observed for steels, stainless steels, nickel-base alloys, aluminum alloys, and titanium alloys exposed to hydrogen. This mode of failure is most often observed in lower-strength alloys, and the extent of loss in tensile ductility is a function of hydrogen content of the material. Loss in tensile ductility behavior is strain rate sensitive and becomes more pronounced as the strain rate decreases (48).

Degradation in flow properties in hydrogen environments has been found at ambient temperatures for iron and steel and at elevated temperature for several alloy systems. The steady-state creep rate under constant load has been observed to increase in the presence of hydrogen for some nickel-base alloys.

Hydride formation produces embrittlement in magnesium, tantalum, niobium, vanadium, uranium, thorium, zirconium, titanium, and their alloys, as well as many other less common metals and alloys. The degradation of mechanical properties and the cracking of these metals and their alloys are attributable to the precipitation of metal hydride phases. Hydrogen pickup often results from welding, heat treating, charging from a corrosion process, or during melting of the alloy. Hydride formation is enhanced for some metal-hydrogen systems by the application of stress-the so-called stress-induced hydride formation. Alloy systems that form hydrides are generally ductile at high (>300 K) and low (< 100 K) temperatures at which they fracture by ductile rupture. This temperature dependence is comparable to that observed for the hydrogen embrittlement of ferrous and nickel alloys. Some of these alloys are also susceptible to failure in hydrogen by mechanisms other than hydriding. Some evidence exists that nickel and aluminum alloys may also form a highly unstable hydride that could contribute to hydrogen damage of these alloys; however, this possibility has not been confirmed.

Mechanisms of Hydrogen Embrittlement

As may be appreciated from the numerous classes of hydrogen damage, there are many explanations or theories for these various forms of degradation. The preeminent theories for hydrogen damage are based on pressure, surface adsorption, de-cohesion, enhanced plastic flow, hydrogen attack, and hydride formation. Although many other theories have been presented, most are variations on these basic models.

The pressure theory of hydrogen damage, or more specifically, hydrogen embrittlement, is one of the oldest models for hydrogen damage. This theory attributes hydrogen embrittlement to the diffusion of atomic hydrogen into the metal and its eventual accumulation at voids or other internal surfaces in the alloy. As the concentration of hydrogen increases at these microstructural discontinuities, a high internal pressure is created that enhances void growth or initiates cracking. This model, although apparently reasonable for blistering and possibly appropriate for some aspects of loss in tensile ductility, does not explain many of the factors observed for classes of failure such as hydrogen stress cracking. However, it is a well-recognized phenomenon that charging hydrogen into steel or nickel alloys at high fugacity, either with high pressure hydrogen gas or under extreme electrochemical charging, can create a significant density of voids and irreversible damage to the alloy consistent with a pressure-dependent model (49).

The surface adsorption theory suggests that hydrogen adsorbs on the free surfaces created adjacent to the crack tip, decreasing the surface free energy and thus the work of fracture. Reduction in the work of fracture would thus enhance crack propagation at stress levels below those typically experienced for a particular alloy in a benign environment. There are many arguments against this model. The principal criticism is that it greatly underestimates the work of fracture and does not account for the discontinuous crack growth that has been observed for hydrogen cracking.

De-cohesion describes the effect of hydrogen on the cohesive force between atoms of the alloy matrix. Sufficiently high hydrogen concentrations that accumulate ahead of a crack tip are assumed to lower the maximum cohesive force between metal atoms such that the local maximum tensile stress perpendicular to the plane of the crack then becomes equivalent to or greater than the lattice cohesive force and fracture results.

Enhanced plastic flow is associated with hydrogen-dislocation interactions and is primarily based on fractographic observations. This approach proposes that atomic hydrogen enhances dislocation motion, generally screw dislocations, and the creation of dislocations at surfaces and/or crack tips leading to softening of the material on a localized scale (50, 51). Although this behavior has been observed in certain steels, hardening by hydrogen has also been found. Careful high-resolution electron microscopy of what appears to be brittle cleavage or intergranular fracture surfaces has revealed evidence of crack tip plasticity in support of this mechanism.

Hydride formation is the degradation of Group Vb metals (niobium vanadium. and tantalum) and zirconium, titanium (52) and magnesium in hydrogen environments by the formation of a brittle metal hydride at the crack tip. When sufficient hydrogen is available in the alloy, a metal hydride precipitates. Cracking of the hydride occurs, followed by crack arrest in the more ductile matrix or continued crack growth between hydrides by ductile rupture. Because hydride formation is enhanced by the application of stress, the stress field ahead of the crack tip may induce precipitation of additional hydrides that cleave. Thus, in some alloys, brittle crack propagation occurs by repeated precipitation of hydrides ahead of the crack tip, cleavage of these hydrides, and precipitation of new hydrides and so on until fracture is complete.

Hydrogen Trapping. Although numerous models exist, none adequately explains the behavior exhibited by alloys in different hydrogen bearing systems. Until a universal theory is developed, one must rely on the phenomenological behavior between the more prominent alloy systems to understand hydrogen damage. One of the principal factors that determines the hydrogen damage susceptibility of various alloys is a phenomenon referred to as trapping. Diffusion studies of iron and steels have shown an initial retardation in diffusion rate or lag time for hydrogen diffusion through these alloys before a steady-state diffusivity compatible with that

expected theoretically is achieved (53, 54). This lag time is generally considered to be related to the filling of traps by hydrogen. In fact, the apparent diffusivity of hydrogen in steels shows a precipitous decrease with increasing concentration of particles (traps). Hydrogen trapping may be considered the binding of hydrogen atoms to impurities, structural defects, or microstructural constituents in the alloy. Binding may be attributed to local electric fields and stress fields, temperature gradients, chemical potential gradients, or physical trapping. These hydrogen traps may be mobile (dislocations, stacking faults) or stationary (grain boundaries). carbide particles, individual solute atoms) (55, 56). They may also be reversible or irreversible traps. Short-duration trapping of hydrogen in which the occupancy time is limited is referred to as reversible. A long residency time for hydrogen characterized by a high binding energy is termed irreversible trapping (57, 58). (57)presents a classification of hydrogen traps in steels. The concept and investigation of trapping have been developed primarily for steels: however, it may not be restricted to this system (59). Face-centered cubic alloys show a similar trapping behaviour, although at a somewhat reduced efficiency for trapping compared to steels (60).

Many factors affect the behavior of ferrous alloys in hydrogen-bearing environments. Hydrogen concentration, temperature heat treatment/microstructure, stress level (applied and yield stress), solution composition, and environment are the primary factors involved in determining susceptibility to hydrogen embrittlement. The longer the baking time, the lower the residual hydrogen in the steel matrix. In general, increasing the concentration of hydrogen in an alloy will reduce time to failure and the stress level at which failure will occur (61-66).

Hydrogen concentration in the alloy is a function of the fugacity or the approximate concentration of hydrogen at the surface exposed to the environment. Therefore, hydrogen embrittlement will be controlled by the hydrogen gas pressure or pH of the environment as well as constituents within the environment that may accelerate or inhibit the entry of hydrogen into the alloy. Elements such as sulfur, phosphorus, antimony, tin, and arsenic and their compounds have been found to inhibit the hydrogen recombination reaction in aqueous solutions, thus increasing the charging of atomic hydrogen into the alloy. In contrast, small amounts of oxygen in gaseous hydrogen environments have demonstrated an inhibitive effect on crack growth of high-strength steels subject to hydrogen cracking.

Temperature also plays an important role in the hydrogen embrittlement of ferrous alloys. Embrittlement is most severe near room temperature and becomes less severe or nonexistent at higher or lower temperatures. At lower temperatures, the diffusivity of hydrogen is too sluggish to fill sufficient traps, but at high temperatures, hydrogen mobility is enhanced and trapping is diminished. Embrittlement is also strongly strain rate dependent. At high strain rates, fracture may proceed without the assistance of hydrogen because the mobility of hydrogen is not sufficient to maintain a hydrogen atmosphere around moving dislocations.

Fracture of low-strength steels in hydrogen environments may be characterized by ductile dimple-rupture, tearing, cleavage, quasi-cleavage, and, less frequently under certain conditions, intergranular cracking.

Nickel and its alloys are susceptible to hydrogen damage in both aqueous and gaseous hydrogen environments. The same factors that affect hydrogen embrittlement susceptibility in ferrous alloys are also prevalent in nickel alloys, although to a lesser degree. In general, fcc metals, because of their greater ease of slip and reduced solute diffusivities as compared to bcc materials, are less susceptible to hydrogen damage. As with ferrous alloys, hydrogen in nickel and its alloys may introduce intergranular, transgranular or quasi-cleavage cracking, and although the macroscopic features appear to be brittle, on a microscopic scale there is a high degree of local plasticity, suggesting that hydrogen enhances flow at the crack tip.

Hydrogen damage in Al alloys

It has been determined that hydrogen embrittles aluminum. For many years all environmental cracking of aluminum and its alloys was represented as SCC .However, testing in specific hydrogen environments has revealed the susceptibility of aluminum to hydrogen damage. Hydrogen damage in aluminum alloys may take the form of intergranular (67) or transgranular cracking or blistering. Blistering is most often associated with the melting or heat treatment of aluminum, where reaction with water vapor produces hydrogen. Blistering due to hydrogen is frequently associated with grain-boundary precipitates or the formation of small voids. Blister formation in aluminum is different from that in ferrous alloys in that it is more common to form a multitude of near-surface voids that coalesce to produce a large blister.

In a manner similar to the mechanism in iron-based alloys, hydrogen diffuses into the aluminum lattice and collects at internal defects. This occurs most frequently during annealing or solution treating in air furnaces prior to age hardening (68).

Dry hydrogen gas is not detrimental to aluminum alloys; however, with the addition of water vapor, subcritical crack growth increases dramatically. The threshold stress intensity for cracking of aluminum also decreases significantly in the presence of humid hydrogen gas at ambient temperature (69).

Crack growth in aluminum in hydrogen is also a function of hydrogen permeability, as in the iron- and nickel-base alloys. Hydrogen permeation and the crack growth rate are a function of potential, increasing with more negative potentials, as expected for hydrogen embrittlement behavior. Similarly, the ductility of aluminum alloys in hydrogen is temperature depended displaying minimum in reduction in area below 0^{o}C, this is similar to other fcc alloys. Most of the work on hydrogen embrittlement of aluminum has been on the 7xxx alloys; therefore, the full extent of hydrogen damage in aluminum alloys has not been determined and the

mechanisms have not been established. Some evidence for a metastable aluminum hydride has been found that would explain the brittle intergranular fracture of aluminum-zinc-magnesium alloys in water vapor. However, the instability of the hydride is such that it has been difficult to evaluate. Another explanation for the intergranular fracture of these alloys is that there is preferential decohesion of grain boundaries containing segregated magnesium. Overaging of these alloys increases their resistance to hydrogen embrittlement in much the same way as for highly tempered martensitic steels. Regarding corrosion-induced material embrittlement, Pantelakis et al. (11, 70) claimed that hydrogen embrittlement could be responsible for the dramatic degradation of toughness and ductility of 2091 and 8090 Al-Li alloys as well as conventional 2024 alloy in several types of accelerated corrosion tests (71). In other alloy systems there is mounting evidence connecting embrittlement and stress corrosion cracking to hydrogen penetration. Speidel (8) reviews recent results, mainly for Al-Mg-Zn alloys. Studies by Scamans et al. (72) of Al embrittlement in humid air, point to the major role of hydrogen. In particular, the intergranular crack path and the reversibility of the phenomenon (recovery of ductility after degassing) support a hydrogen, rather than an anodic dissolution, mechanism. Also, Scamans and Tuck (73) measured H_2 permeability and stress corrosion resistance of the Al-Mg-Zn alloy, as functions of quench- rate and aging treatment, and found similar trends. However, the stress-corrosion-resistant Al-Mg-Si alloy does not allow hydrogen permeation through its matrix, though the volume of hydrogen produced by surface reaction with the water in humid air is even higher than that of the Al-Nig-Zn alloy (73). It has been suggested (8) that hydrogen plays a major role in stress corrosion cracking of aluminum alloys exposed to aqueous solutions as well. An indication in favor of this argument is provided by measurement, in Al-Mg-Zn alloys, of hydrogen permeation and stress corrosion crack growth rates (74). These parameters are found to vary similarly as functions of the electrode potential. Despite the lack of a universally accepted hydrogen embrittlement mechanism, a generally recognized common feature is that some critical concentration of hydrogen must buildup at potential crack sites, for failure to initiate. Thus, the distribution of hydrogen inside the metal and its pattern of migration are of paramount importance in understanding the phenomena and designing alloys with improved behavior.

It has been shown (75, 76) that lattice defects (vacancies, dislocations, grain boundaries) and precipitates provide a variety of trapping sites for diffusing hydrogen. Hydrogen traps have mechanistically been classified by Pressouyre (57) as reversible and irreversible, depending on the steepness of the energy barrier needed to be overcome by hydrogen to escape from the trap. For example, during a degassing experiment reversible traps will release hydrogen continuously, while irreversible ones will do so only after a critical temperature has been reached. This is the temperature at which the probability of a single jump out of the steep trap becomes non-negligible. Reversible and irreversible traps may play different roles during an actual experiment (58). In particular, irreversible traps will always act as sinks for hydrogen,

whereas reversible traps may act as sinks or sources depending on initial hydrogen charging of the lattice. A uniform distribution of irreversible traps is believed to provide a beneficial effect in alloy behavior under embrittling conditions, by arresting diffusing hydrogen and thus delaying its buildup at the crack sites (55, 77). When crack nucleation and growth is along the grain boundaries, boundary chemistry may be playing an important role. Various studies on Al-Mg-Zn alloys have indicated that alloying elements (and in particular Mg) are segregated on the grain boundary. Tuck (78) proposed that Mg hydride forms at grain boundaries and is responsible for material embrittlement. In an effort to explain the connection between Mg-H interaction and material embrittlement, Song et al. (79) showed that stress corrosion and fatigue crack growth rates increase with the concentration of solid solution Mg on grain boundaries. The same authors theoretically calculated a decrease in the intergranular fracture work with both Mg and H segregation. Other aluminum alloys that have been studied for hydrogen induced failure are 8090 (80, 81) and 7050 (79).

Useful insight in the nature and intensity of hydrogen traps can be offered by studying the temperature needed to break these bonds. Thus, thermal analysis techniques have been used for a variety of alloys (59, 78). In particular, thermal desorption has been successfully used to study hydrogen partitioning in pure cast aluminum and in Al-Cu and Al-Mg_2Si alloys (76) and hydrogen diffusion in Al-Li alloys. Among other findings, these studies show that, for aluminum alloys, the energy of chemisorption is lower than the energy for lattice diffusion. Thus, the layer of passive oxide-formed on the surface of aluminum alloys-does not mask the bulk trapping states, and the results of thermal analysis are meaningful. Accelerated corrosion tests were used by Haidemenopoulos et al. (82) to characterize corrosion and hydrogen absorption in the less studied but widely used Al-Cu alloy 2024. In (83) hydrogen evolution from the corroded specimen of Al alloy 2024 was systematically measured as a function of temperature. The exfoliation test (43) was used as an accelerated corrosion method, and different exposure times were tested. The existence of multiple trapping states was verified and the quantity and evolution pattern of hydrogen is discussed.

Chapter 3 - Experimental procedures

3.1 Materials Studied

As discussed earlier, the main focus of this research was aluminum alloys belonging to the 2xxx alloy series, more accurately, alloy 2024. The material was obtained in plate form, that had not been anodised and its only surface protection emanated from the thin protective oxide, which is created when the material is exposed to atmospheric air. Material was obtained from several suppliers and with thickness 3.2mm.

The chemical composition of the material is displayed below in Table 3. 1 and below in Table 3. 2 the thermal treatments of the alloys are presented.

Table 3. 1: Chemical composition of alloys of aluminum (%wt.).

Sample	Al	Si	Fe	Cu	Mn	Mg	Cr	Zn	Ti	Other
2024	90,7-94,7%	0,50%	0,50%	4,35%	0,60%	1,5%	0,10%	0,25%	0,15%	0,15%

Table 3. 2: Thermal treatments of aluminum alloys.

Material	Temperature Dissolution	Quenching	Cold rolling	Thermal treatment
2024 Bare	495 °C	0°C	No	Aging 170°C

The labeling scheme used to identify the orientations and planes of the alloys is shown in Fig. 3. 1.

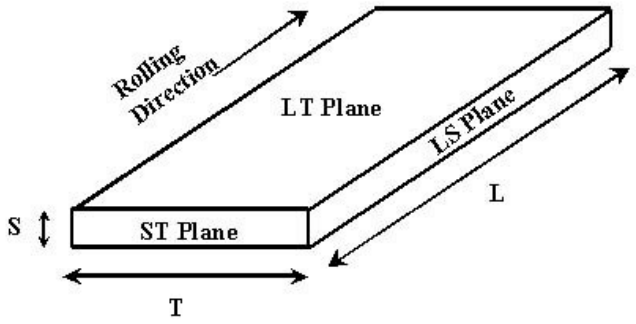

Fig. 3. 1: Labelling scheme used for directions and planes.

3.2 Microstructural characterization

All specimens were prepared using classical metallographic techniques. The non-corroded specimens were cut from the plate of the corresponding material with the use of a microtom (Struers Accutom). Their size was roughly 0,5 x 1cm².The specimens for metallographic observation were placed in simple epoxy resin (Acryfix) that stabilizes in atmospheric temperature (20-25^{0}C) in roughly 10 minutes.

The specimens were placed in epoxy resin for easy handling. The resin fills the pores, voids and surface abnormalities of the specimen. This process is essential for the maintenance of pits and microcracks during the next steps of preparation. The surface planes under observation were the rolling surface and the side surface (LT and LS plane in Fig. 3. **1**.Next the specimens were initially grinded on SiC abrasive wheels. The sizes of grains were 220, 500, 800, 1000, 2000 grid. Polishing of the specimens followed on special disks with diamond paste of 3μm and 1μm grain size respectively. The last stage of preparation was polishing with Al_2O_3 particles of 0,45μm diameter .Finally the surface was chemically etched with Keller's reagent. This reagent has a chemical composition of: *2,5 ml HNO_3, 1,5 ml HCl, 1,0 ml HF and 95,0 ml H_2O*. The time of exposure in Keller's was a few seconds. Finally the specimens were washed with distilled water and alcohol and dried in a purge of warm air (84).

3.3 Accelerated corrosion testing

Accelerated corrosion testing that provides a useful simulation of the exfoliation behavior of these alloys in various types of outdoor service, especially in marine and industrial environments, was employed. The accelerated corrosion test (EXCO) is described in ASTM specification G34-90 (43). It includes exposure at 22°C, for 12,24,48 and 72 hours respectively,

for the not-heat treated specimen, in a solution containing 234g NaCl, 50g KNO_3 and 6,3ml concentrated HNO_3 (70%wt) diluted to 1 L of distilled water. The quantity of solution used is proportional to the specimen external surface area, with the minimum amount required being 10 ml for every cm^2 of specimen surface and the maximum 30ml. Specimen cleaning, after removal from the corrosive solution involved soaking in concentrated HNO_3 (70%wt) for 5 minutes, rinsing in distilled water, then in acetone and thoroughly drying in a purge of warm air. The entire cleaning process did not exceed 10 minutes. Then, half of the specimens were placed in simple epoxy resin for metallographic observation and others were used for the determination of hydrogen quantity trapped in the material's microstructure.

3.4 Heat treatment

Some specimens were surface-cleaned with alcohol according to ASTM G1 and then were heat treated. The specimens all artificially aged, after solid solution at 490^{o}C for 30 min. Different artificial aging conditions were performed for the total 22 specimens at 170 ^{o}C, in an electric oven with ±5 ^{o}C temperature control and for different times.

The aging temperature were selected in order to affirm the results of the artificial aging of the commercial sheet AA2024-T3, according to a paper by Alexopoulos et al. (85). Aging times were selected to correspond to all aging conditions, including Under-Aging (UA), Peak-Aging (PA) and Over-Aging (OA). Some of the available specimens were exposed for 2h to the laboratory exfoliation corrosion (EXCO solution) according to specification ASTM G34 and others for 24 hours. Then, half of the specimens were placed in simple epoxy resin for metallographic observation and others were used for the determination of hydrogen quantity trapped in the material's microstructure.

3.5 Scanning Electron Microscopy (SEM)

Surface analysis was performed to the corroded specimens provided by the tests performed. Images were acquired with a Jeol Scanning Electron Microscope in the secondary electron mode with an accelerating voltage of 30 KV.

The scope of this work was to investigate the appearance of the corroded surface in order to determine pitting sites and other modes of corrosion. As corroded specimens with different

tempers were examined the difference was correlated with corrosion, microstructure and heat treatment.

The outcome of the metallographic analysis was also combined with the hydrogen content measurements and provided evidence of possible hydrogen embrittlement.

After the heat treatment tests, the specimen were placed in the SEM microscope mention above for examination. The study of the surface correlated with the corrosion results and the hydrogen measurements will lead to a spherical understanding of hydrogen embrittlement.

So, immediately after corrosion the specimens were immersed in concentrated nitric acid (70%) for 5 minutes, in order to remove the corrosion products deposited during electrochemical action. Finally they were dried in a purge of warm air. For the observation in SEM it is essential that the conductivity of specimens during observation is ensured, therefore the specimens were affixed on the special specimen holder with graphite paste. Then they are placed in the vacuum chamber of the microscope for the observation.

3.6 Hydrogen measurements

A main part of this thesis consists of the determination of hydrogen concentration and it's trapping states in the material after corrosion. The determination of these states was conducted by using a thermal desorption technique.

The scope of this process was to measure the amount of hydrogen eluting from specimens previously subjected to various periods of exfoliation corrosion exposure as a function of temperature. Strips of the materials, 3.2mm wide and 20 mm long, were be cut at right angles to the rolling direction and were exposed to exfoliation corrosion. The large surface to volume ratio of the specimen was chosen with a view to decreasing the hydrogen evolution time and increasing the sensitivity of the measurements. The exfoliation accelerated corrosion test is described in ASTM specification G34-90 as is mentioned above in 3.2. Hydrogen evolved from the corroded specimen with controlled heating in an inert atmosphere and was measured using a gas chromatograph.

For the determination of hydrogen quantity trapped in the material's microstructure an in-house experimental setup was used. This setup consists of a furnace with a system of automatic temperature control, a supply of inert gas (high-purity nitrogen) and a gas chromatograph equipped with a valve for sampling gases. The sample was placed in a 10 mm diameter quartz tube and held in place by an inert porous diaphragm, permeable to the gas (quartz wool). The tube was inserted in the furnace and subjected throughout the experiment to a flow of Q=20ml/min high purity nitrogen. This flow was then driven to a gas chromatograph equated

with a TCD detector. Calibration runs were performed using standard $H_2 - N_2$ mixtures, of volume concentration 1000 and 10000 ppm. Blind experiments were conducted with an empty tube heated up to 600^{o}C and no hydrogen was detected. The temperature of furnace was increased at a rate of approximately 5^o C/min and the nitrogen current swept along everything that was emitted by the sample and carried it in the gas chromatograph. The sampling was performed manually through the gas-sampling valve about every 2 minutes.

Primary data consist of curves of the intensity, I, of TCD detector signal (in μV) versus time, combined with the temperature history of the specimen. Detector intensity is converted to hydrogen mass flow rate, m, by the expression

$$m=\alpha IQ$$

where α has units of g of H_2/(ml μV). It is the calibration constant of the detector expressing the mass concentration of hydrogen per μV indication of the detector. During the present work, a small deterioration of the accuracy of the detector was witness, which was taken into account in the data.

The results reported in the next section are presented as hydrogen mass flow rate (in μg/min) versus specimen temperature. If the heating rate is sufficiently low, each trapping site produces an independent peak. The temperature of the onset of peak growth is characteristic of the energy needed to release hydrogen from the respective trapping site. Thus, low temperature peaks are related to weakly bonded hydrogen and high temperature peaks to strongly bonded hydrogen. Calculation of the total hydrogen quantity in each trapping site is performed by integrating the area under the respective peak.

Chapter 4 – Results and Discussion

4.1 Metallography –Microstructural Characterization

Objective

The objectives of the microstructural characterization are the following:

- To assess the corrosion damage in terms of pitting, intergranular corrosion, exfoliation and depth of attack
- To determine possible pathways of hydrogen entry in the material during corrosion.

As explained in the preceding chapter some optical and electro-optical characterization techniques were used in order to assess the corrosion damage at varying microstructural levels. Surface damage, at different stages of corrosion, examined by SEM investigations were employed. Intergranular corrosion, exfoliation attack and hydrogen pathways were assessed with metallographic sectioning.

The as received material was prepared for metallographic observations, as described in Chapter 3. The resulting microstructure is presented in Figures Fig.4.1- Fig.4.3. Figure Fig.4.1 depicts metallographic images in the LS direction for magnifications x100, x500 and x200 respectively. It is observed, that longwise this direction the grains are elongated and several second phase particles along the grain boundaries.

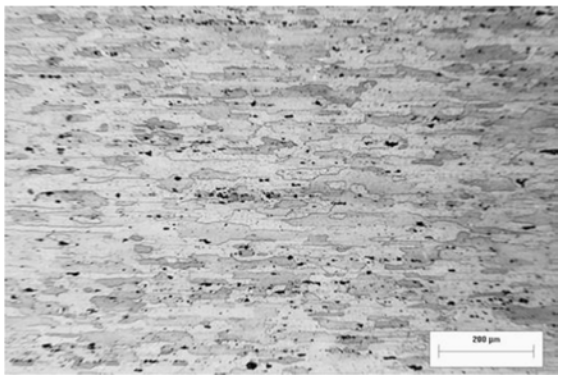

(a)

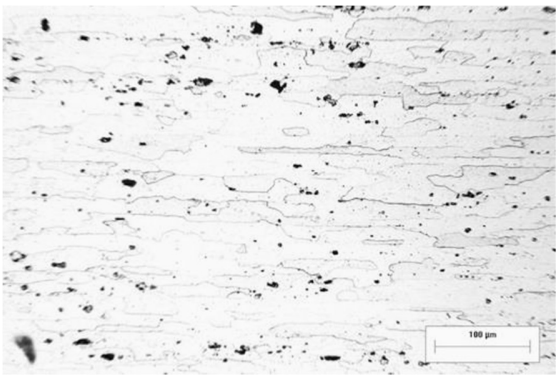

(c)

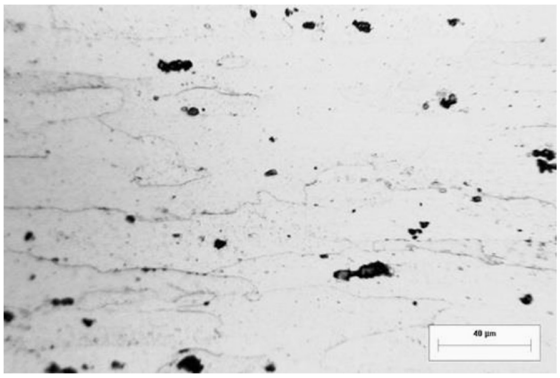

(b)

Fig.4.1: As received aluminum alloy 2024-T351. Metallographic images in the longitudinal direction (LS plane) for magnifications (a) x100, (b) x500 and (c) x200 respectively.

Fig.4.2depicts metallographic images on the LT (rolling) plane for magnifications x100, x500 and x200 respectively. As well, It is observed several second phase particles along the grain boundaries.

(a)

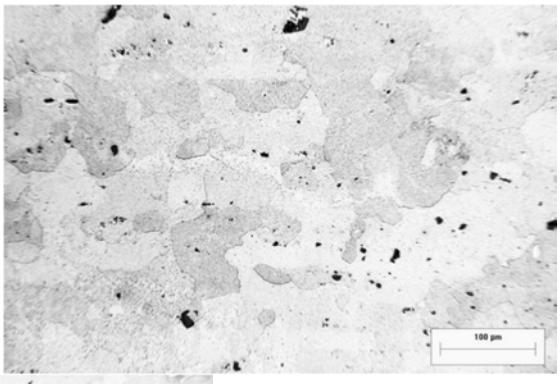

(c)

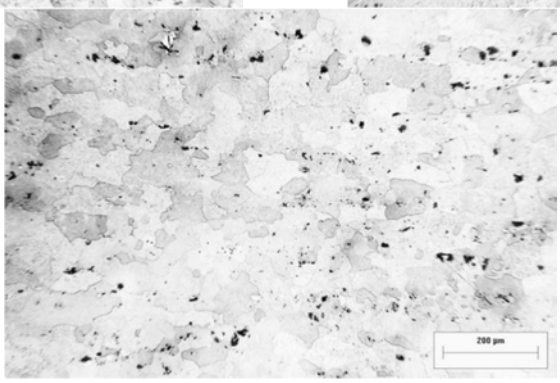

(b)

Fig.4.2. As received aluminum alloy 2024-T351. Metallographic images from the surface of the specimen (LT plane) for magnifications (a) x50,(b) x100,(c) x200 respectively.

Figure Fig.4.3 depicts metallographic images in the transverse direction for magnifications x100, and x200. It is observed, that along this direction the grains are elongated and several second phase particles along the grain boundaries.

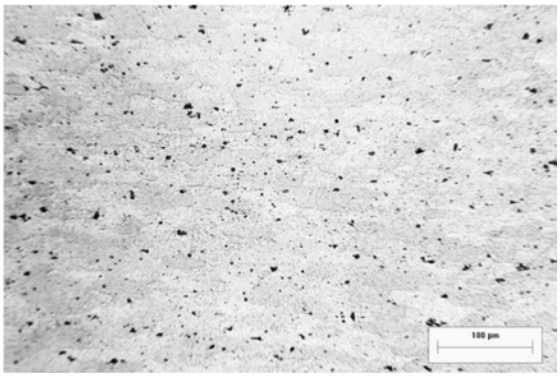
(a)
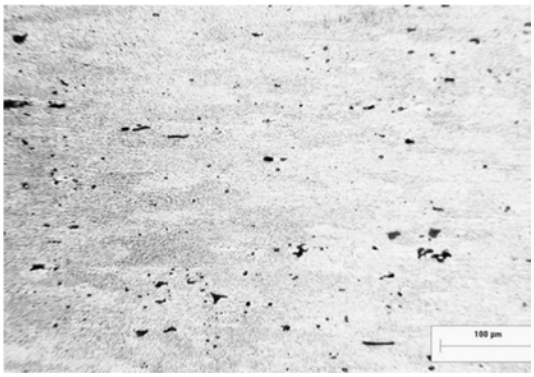
(c)
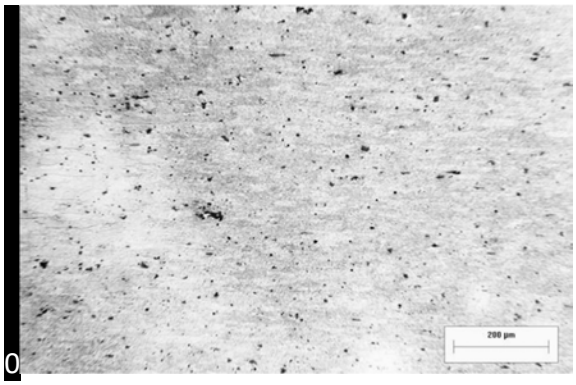
(b)

Fig.4.3: As received aluminum alloy 2024-T351. Metallographic images in the transverse direction (ST plane) for magnifications (a) x200,(b) x100 and(c) x200 respectively.

4.2 Accelerated corrosion testing of the as received material

The experimental procedure involves the following actions: (1) accelerated corrosion testing (using the EXCO procedure), (2) detailed microstructural investigation of the evolution of corrosion damage by employing, SEM and metallography. Figures Fig. 4.4 -Fig. 4.7correspond to specimens with varying exposure time to the exfoliation solution (from 12h up to 72h). All specimens were prepared using classical metallographic techniques

Corrosion Exposure 12 Hours

Initially, several of the aluminum alloy 2024-T351 specimens, were exposed to the EXCO solution for 12 h. Certain areas of the surfaces show the development of a network of pitting corrosion (Fig. 4.4). The pits have a depth of 411μm in the ST plane and 244μm in the LS plane. So it seems that the corrosion activity starts early, even after 12 h exposure time.

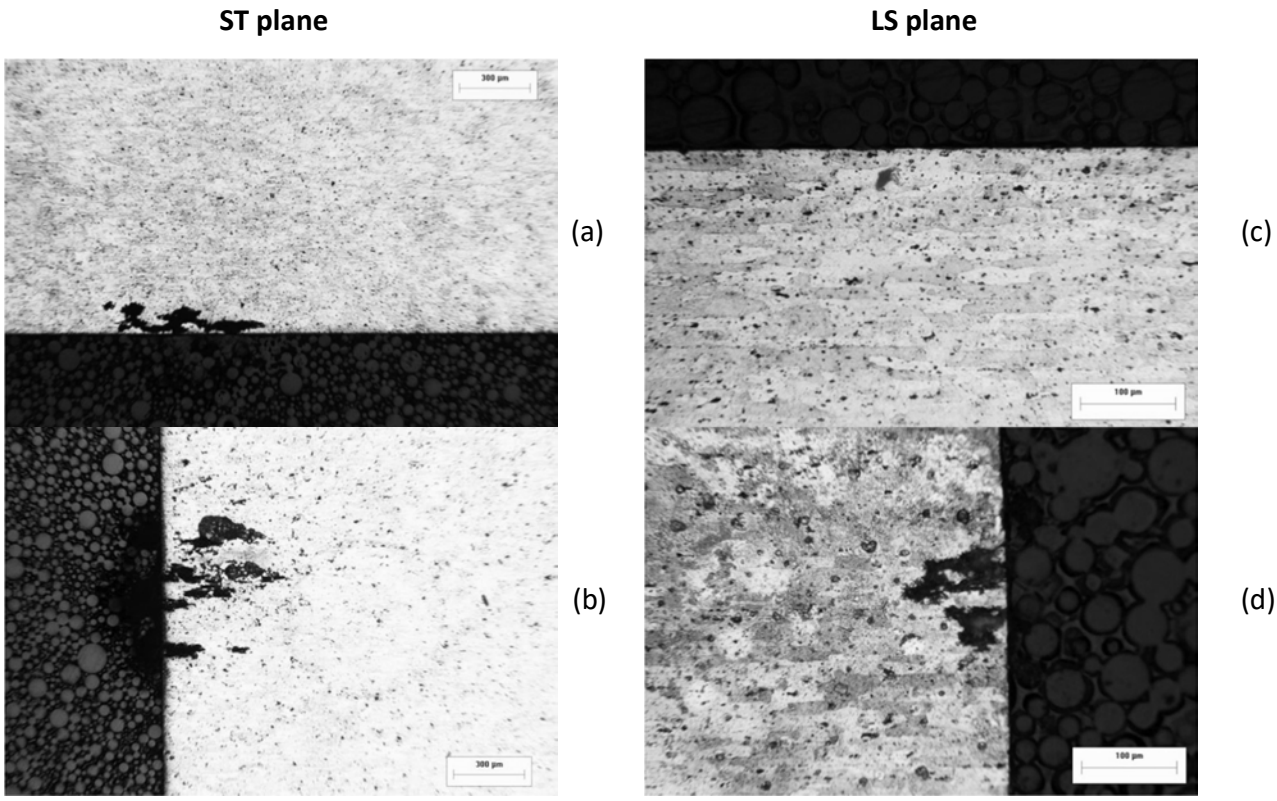

Fig. 4.4: Aluminum alloy 2024-T351 after exposure to EXCO solution for 12 h. Images (a) to (b) depict exfoliation in the ST plane. Magnification is x50 respectively. Maximum depth of attack was measured 411 μm as illustrated in Table 3.

Corrosion Exposure 24 Hours

After 24 hours exposure, pitting density has increased and the pits grow deeper. The maximum pit depth varies around 420 μm. A new feature is the appearance of exfoliation corrosion, intergranular cracks form under the surface. Specifically Images (a) to (c) depict exfoliation in the ST plane. Magnification is x50, and 100 and the pits have a maximum depth of 366 μm (Fig. 4.5.b) .Images (d) to (f) depict exfoliation in the LS plane .Magnification is x50, x100, and x200 and the maximum depth of attack was measured 229 μm.

ST plane **LS plane**

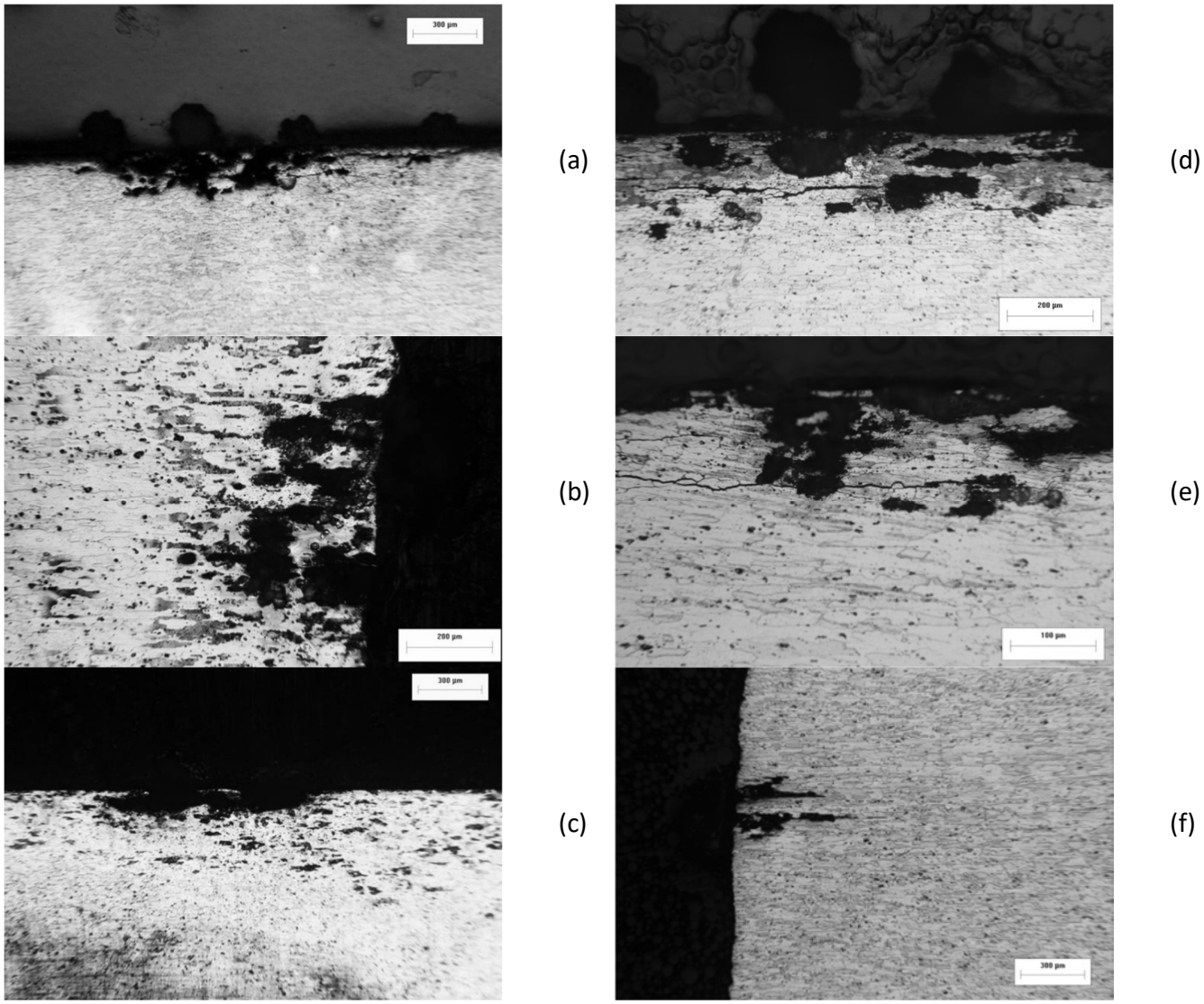

Fig. 4.5: Aluminium alloy 2024-T351 after exposure to EXCO solution for 24 h. Images (a) to (c) depict exfoliation in the ST plane. Magnification is x50, x100, and x50 respectively. Maximum depth of attack was measured 366 µm at fig (b) (as illustrated in table 1).Images (d) to (f) depict exfoliation in the LS plane, magnification is x50, x100, x200 and x50 respectively. Maximum depth of attack was measured 428 µm as illustrated in Table 3.

Corrosion Exposure 48 Hours

After 48 hours exposure, new corrosion pits initiate all over the surface. Pit depth has ceased to increase. However pits that formed at earlier times grow in diameter and lose their steepness, while the clustering of pits is enhanced (Fig. 4.6). Exfoliation corrosion is intensified. Specifically Images (a) to (c) depict exfoliation in the ST plane. Magnification is x50,x 100, x200 and the pits

have a maximum depth of 351 μm (Fig. 4.6.b). Images (d) to (f) depict exfoliation in the LS plane. Magnification is x100, and x200 and the maximum depth of attack was measured 217 μm at fig (f), as illustrated at Table 3.

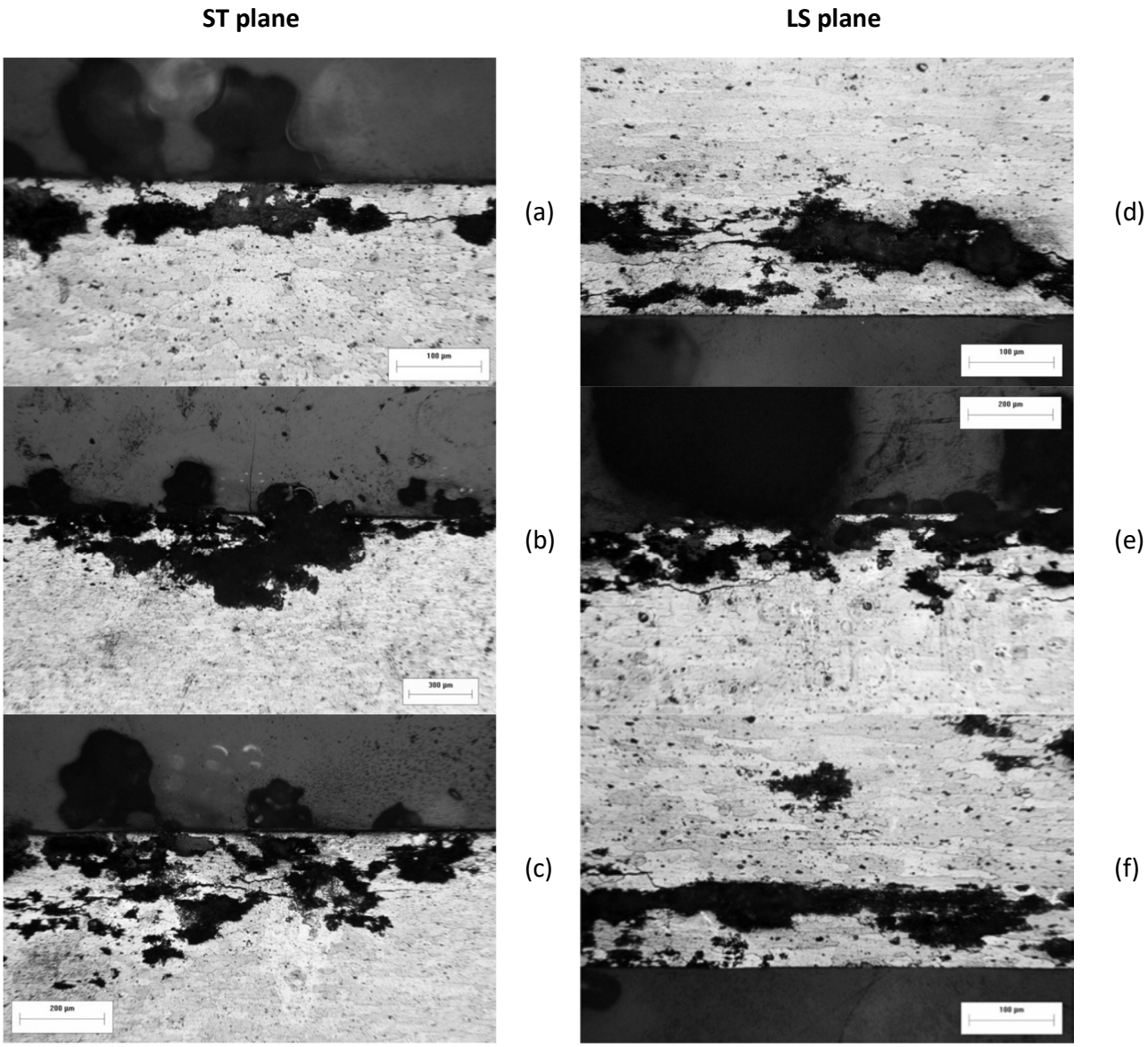

Fig. 4.6.: Aluminum alloy 2024-T351 after exposure to EXCO solution for 48 h. Images (a) to (c) depict exfoliation in the ST plane. Magnification is, x200 x50, x100 respectively. Maximum depth of attack was measured 451 μm at fig (b) (as illustrated in table 1).Images (d) to (g) depict exfoliation in the LS plane, magnification is x200, x100, and x200 respectively. Maximum depth of attack was measured 217 μm at fig (f) as illustrated in Table 3.

Corrosion Exposure 72 Hours

After 72 hours exposure, similarly to 48h of corrosion the pit depth has ceased to increase. Exfoliation corrosion at a rather aggressive stage with layers of material ready to be removed. Specifically Images (a) to (c) depict exfoliation in the ST plane. Magnification is x50 and the pits have a maximum depth of 428 μm (Fig. 4.7.c) .Images (d) to (f) depict exfoliation in the LS plane. Magnification is x50 and x100, and the maximum depth of attack was measured 224 μm at fig (e), as illustrated at Table 3.

ST plane **LS plane**

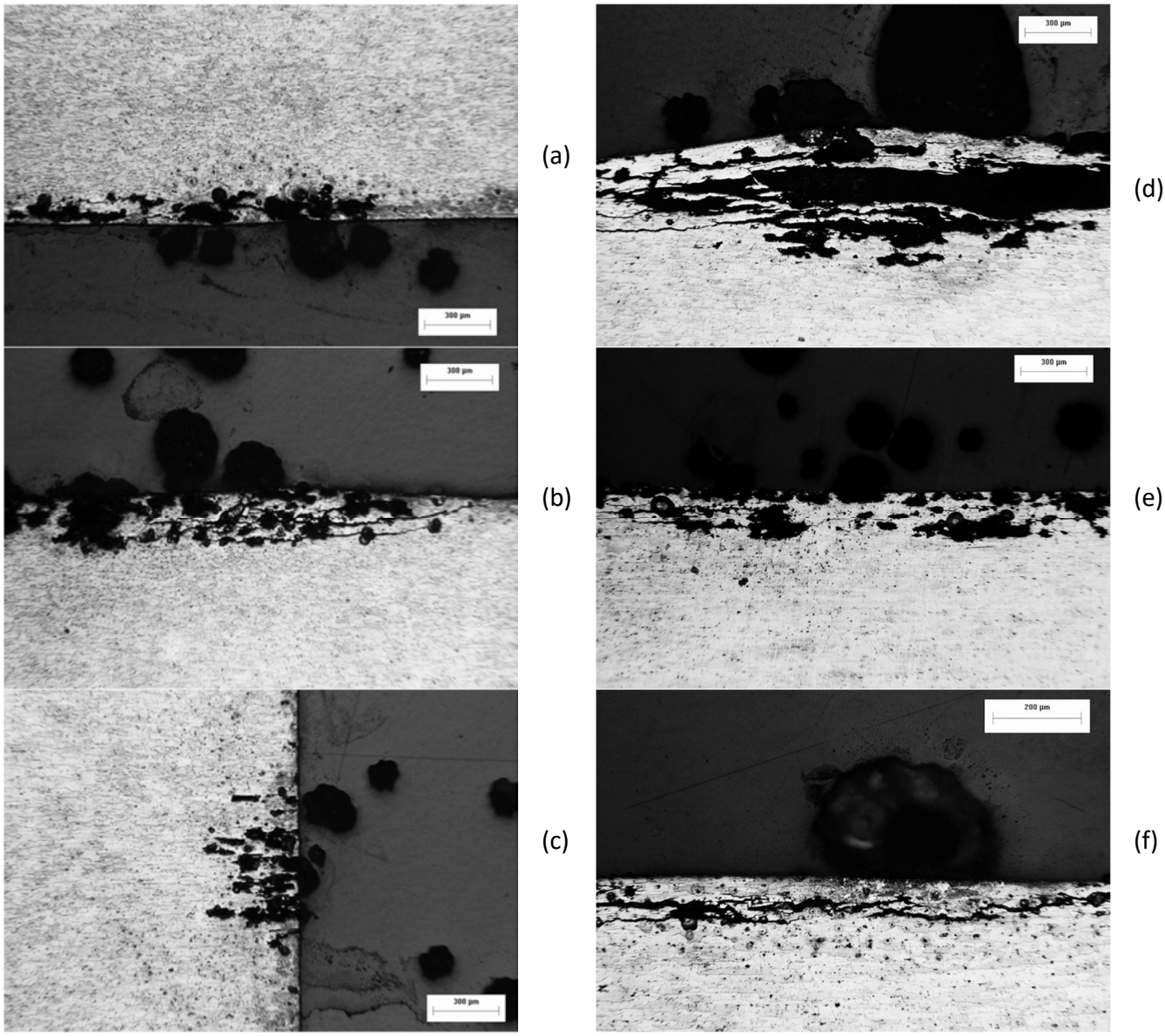

Fig. 4.7: Aluminium alloy 2024-T351 after exposure to EXCO solution for 72 h. Images (a) to (c) depict exfoliation in the ST plane. Magnification is x50. Maximum depth of attack was measured 428 μm at fig (c) as illustrated in table 1.Images (d) to (f) depict exfoliation in the LS

plane, magnification is x50, x50 and x100, respectively. Maximum depth of attack was measured 229 μm at fig (e) as illustrated in Table 3.

Table 3. Maximum depth of attack for the different times of exposure in the exfoliation corrosion.

TIME	ST plane	LS plane
12 h EXCO	411	244
24 h EXCO	428	229
48 h EXCO	451	217
72 h EXCO	600	224

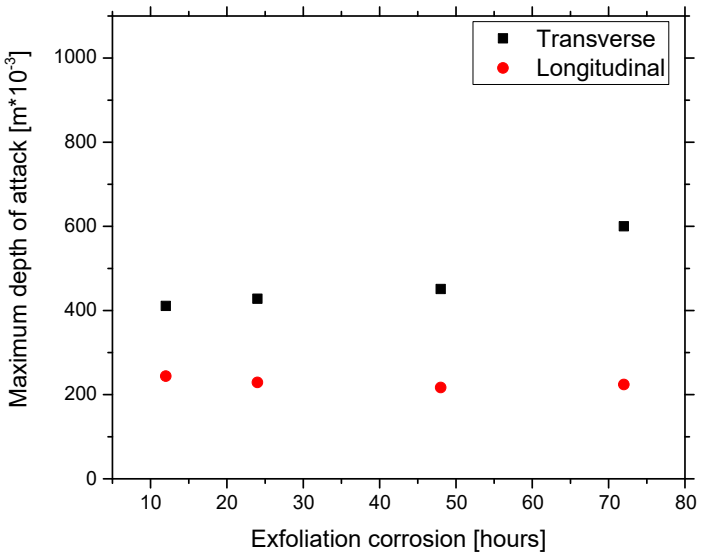

Fig. 4.8. Maximum depth of attack, of not heat treated aluminum alloy 2024-T351 specimens after exposure to EXCO solution.

4.3 Effect of aging on the exfoliation corrosion

22 specimens were surface-cleaned with alcohol according to ASTM G1 and then were heat treated. The specimens all artificially aged, after solid solution at 490°C for **30 min**. The specimens were artificially aged at 170 °C, in an electric oven with ±5 °C temperature control. The aging temperature was selected in order to affirm the results of the artificial aging of the commercial sheet AA2024-T3, according to (85). Aging times were selected to correspond to all

aging conditions, including Under-Aging (UA), Peak-Aging (PA) and Over-Aging (OA). Specifically, the different artificial aging conditions, where these specimens were performed, were respectively 30 min, 1 h , 2 h, 4 h, 6 h, 9 h, 15 h, 24 h, 48 h, 63 h, 98 h.

Half of the available specimens were exposed for 2h to the laboratory exfoliation corrosion (EXCO solution) according to specification ASTM G34 and the others, for 24 hours. Then, the specimens were placed in simple epoxy resin for metallographic observation. Metallographic sections were also prepared and examined in order to determine the depth of attack with exposure time after heat treatment at different conditions.

For the specimens exposed to the exfoliation solution for 2 h, Fig. 4.9 to Fig.4.19 depict the corrosion damage. Corrosion is more intense in the mid-plane of the LS plane (side surface-LS direction) and the maximum depth is 173,031 μm as shown in Fig. 4.13.

At 30 min of exposure time, corrosion spreads on the LT plane without further penetration in depth. However this spreading is moving beneath the surface of the material and causes exfoliation of surface layers. The exfoliation process becomes more intense with the increase in aging time. Fig. 4.12 shows the corrosion attack after 4 h of aging, where significant material removal has taken place. The subsurface spreading of corrosion damage proceeds with exfoliation corrosion as shown in Fig. 4.13. Similar corrosion damage development is observed at higher aging times as shown in Fig4.14, Fig. 4.15, Fig.4.16, Fig4.17, Fig.4.18 and Fig.4.19 for 9, 15, 24, 48, 63 and 98h aging respectively.

The above observations from the Metallographic sections lead to conclusions regarding the evolution of corrosion damage with exposure time. Corrosion starts in the form of isolated pits. In the first 30 min of exposure pits deepen and grow laterally. Pit density increases and pit-to-pit interaction starts. Pits interact via intergranular corrosion .This leads to pit coalescence and pit cluster formation. Pit clusters grow laterally beneath the material surface via intergranular corrosion, leading to exfoliation of surface layers of the material. This type of damage evolution, more specifically the intergranular network supporting pit growth is also responsible for the transport of corrosion solution deep in the material, so that the corrosion reaction takes place in a certain depth producing hydrogen. This is one of the main mechanisms of hydrogen transport in relatively high depths, which cannot otherwise be explained solely by diffusion from the material surface. However once hydrogen is produced, e.g. at the bottom of a corrosion pit, it diffuses to the adjacent unaffected material and establishes a hydrogen diffusion zone below the corrosion zone.

Corrosion Exposure 2 Hours

Aging time 30 min

Initially, several of the aluminum alloy 2024-T351 specimens, were artificially aged for 30 min at 170°C and subsequent exposed to the EXCO solution for 2 h. The ST and LS planes after 30 min of aging seem devoid of corrosion (Fig. 4.9). The pits have a depth of 70,6 μm (Fig. 4.9.c) in the ST plane and 49,6 μm (Fig. 4.4) in the LS plane. So it seems that there is some corrosion activity after 30 min aging and 2 h exposure time.

ST plane **LS plane**

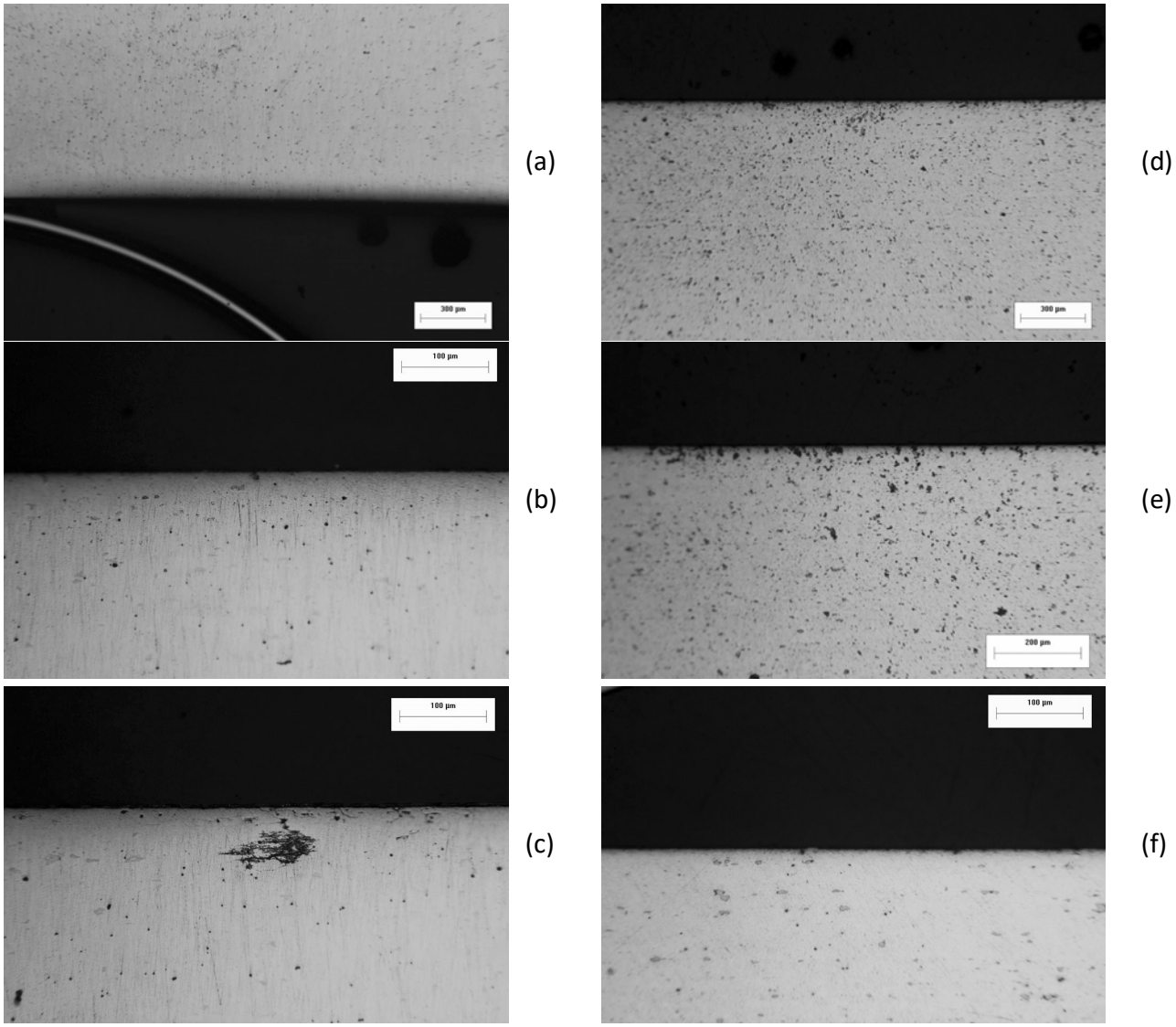

Fig. 4.9: Exfoliation corrosion for alloy 2024-T351 after aging for 30 min at T=170°C. Images (a) to (c) depict exfoliation in the ST plane. Magnification is x50, x100, x200 respectively. Maximum depth of attack was measured 70,6 μm at fig (c).

Aging time1 hour

After 1 hour aging, pitting density has increased and the pits grow deeper. The maximum pit depth varies from 73 to 82 μm. A new feature is the grouping of pits, i.e pits that grow close to each other coallesce and form a larger corrosion area. Specifically Images (a) to (c) depict exfoliation in the ST plane. Magnification is x50, x100 and x200 and the pits have a maximum depth of 82 μm (Fig.4.10.b). Images (d) to (f) depict exfoliation in the LS plane .Magnification is x50, x100, and x200 and the maximum depth of attack was measured 73 μm at (Fig.4.10 d).

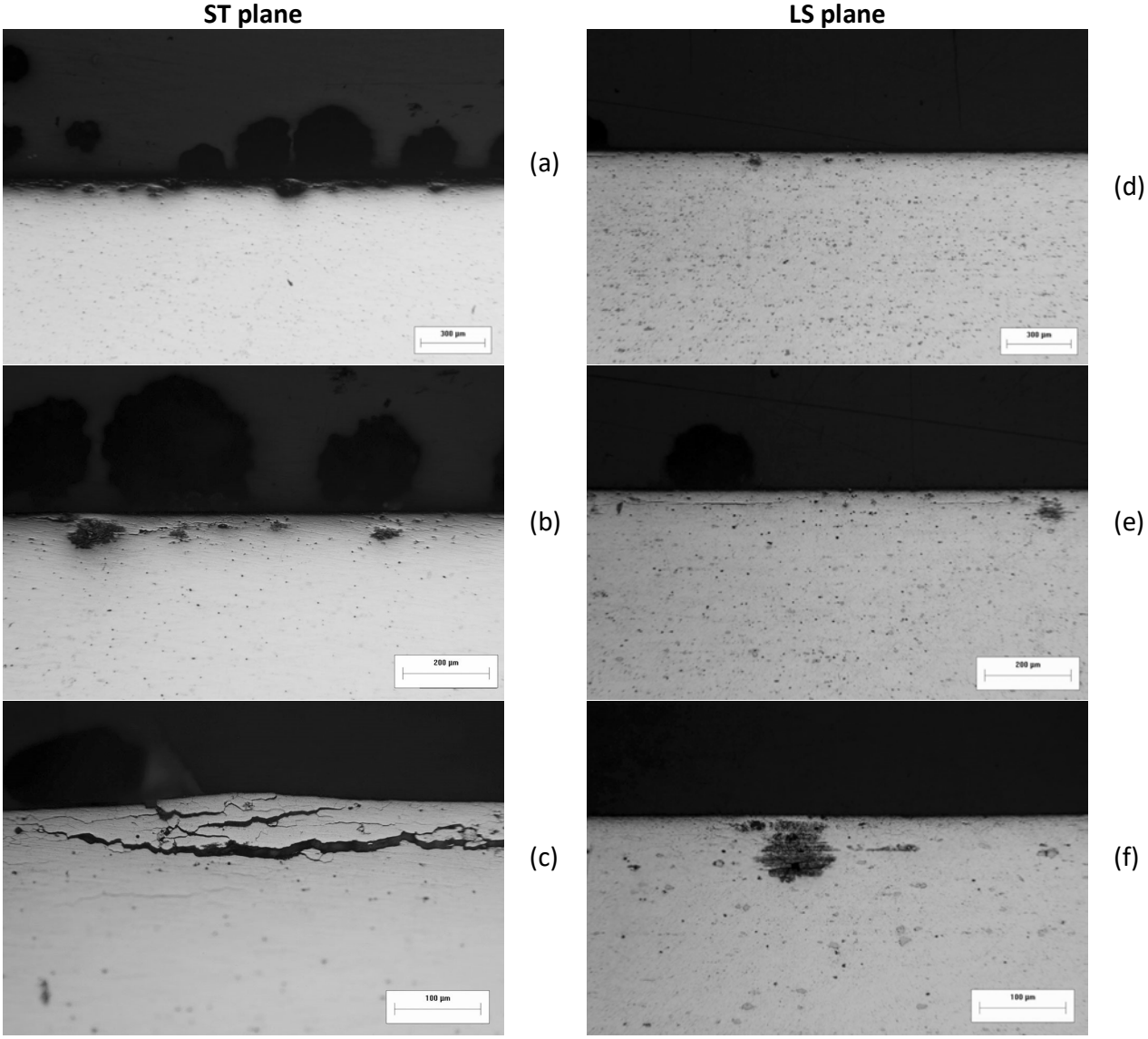

Fig.4.10 Exfoliation corrosion for alloy 2024-T351 after aging for 1 hour at T=170ºC. Images (a) to (c) depict exfoliation in the ST plane. Magnification is x50, x100, x200 respectively. Maximum depth of attack was measured 82,42 μm at fig (b) as illustrated in Table 4.

Aging time 2 hours

After 2 hours aging, pitting density has not increased significantly and the pits do not grow deeper. The maximum pit depth varies from 74 to 76 μm. Specifically Images (a) to (c) depict exfoliation in the ST plane. Magnification is x50, x100 and x200 and the pits have a maximum depth of 76 μm (Fig.4.11.c) .Images (d) to (f) depict exfoliation in the LS plane .Magnification is x50, x100, and x200 and the maximum depth of attack was measured 74 μm at(Fig.4.11.f).

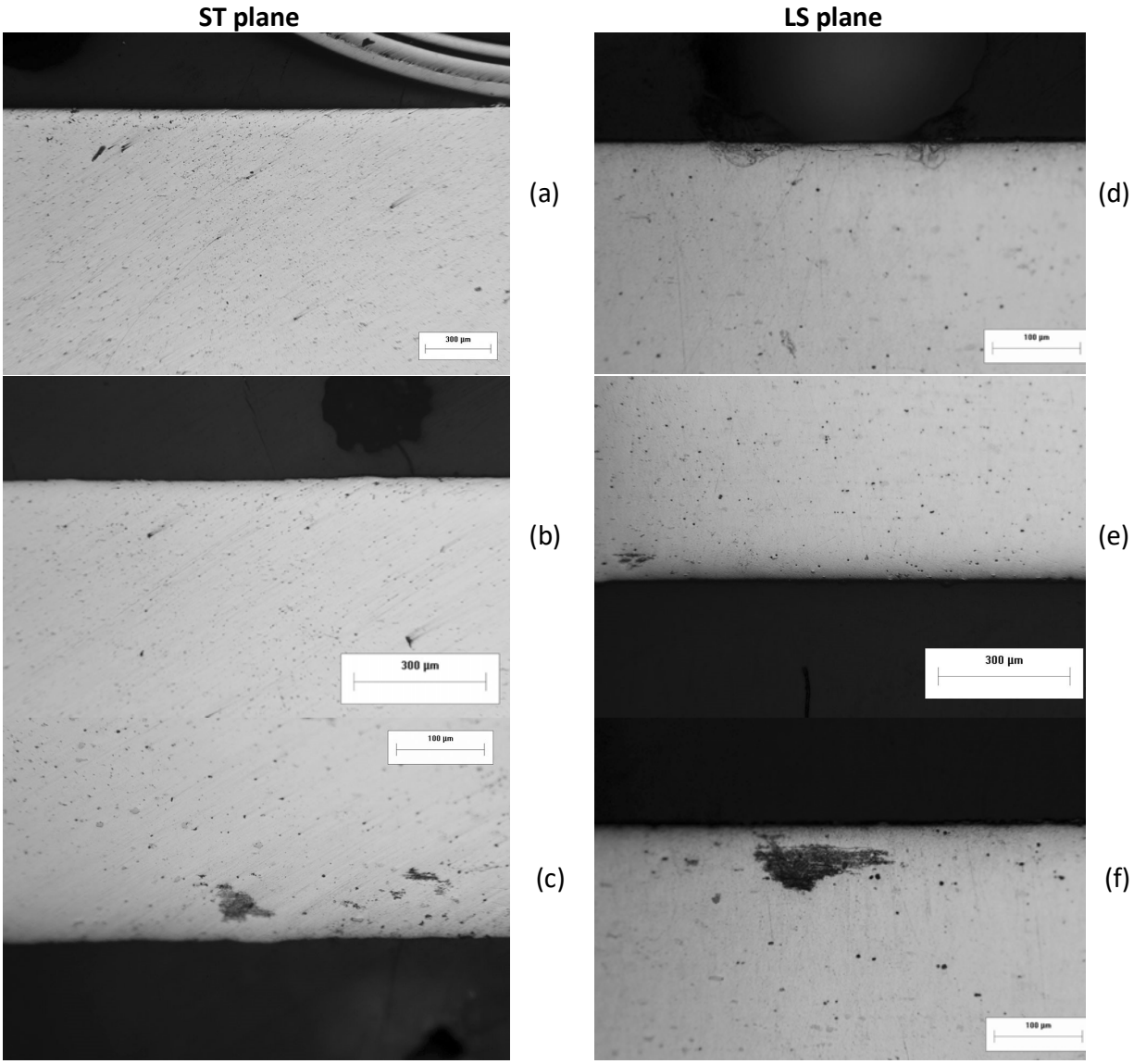

Fig.4.11: Exfoliation corrosion for alloy 2024-T351 after aging for 2 h at T=170^{o}C. Images (a) to (c) depict exfoliation in the ST plane. Magnification is x50, x100, x200 respectively . Maximum depth of attack was measured 76,97 μm at fig (c) as illustrated in Table 4.

Aging time 4 hours

After 4 hours aging, new corrosion pits initiate all over the surface. Pits are larger and the clustering of pits is enhanced (Fig. 4.12). A new feature is exfoliation corrosion which is quite severe (Fig. 4.12.b). Specifically Images (a) to (c) depict exfoliation in the ST plane. Magnification is x50,x 100, x200 and corrosion has a maximum depth of 141 μm (Fig. 4.12.b). Images (d) to (f) depict exfoliation in the LS plane. Magnification is x50, x 100, x200 and the maximum depth of attack was measured 167 μm at (Fig. 4.12.e).

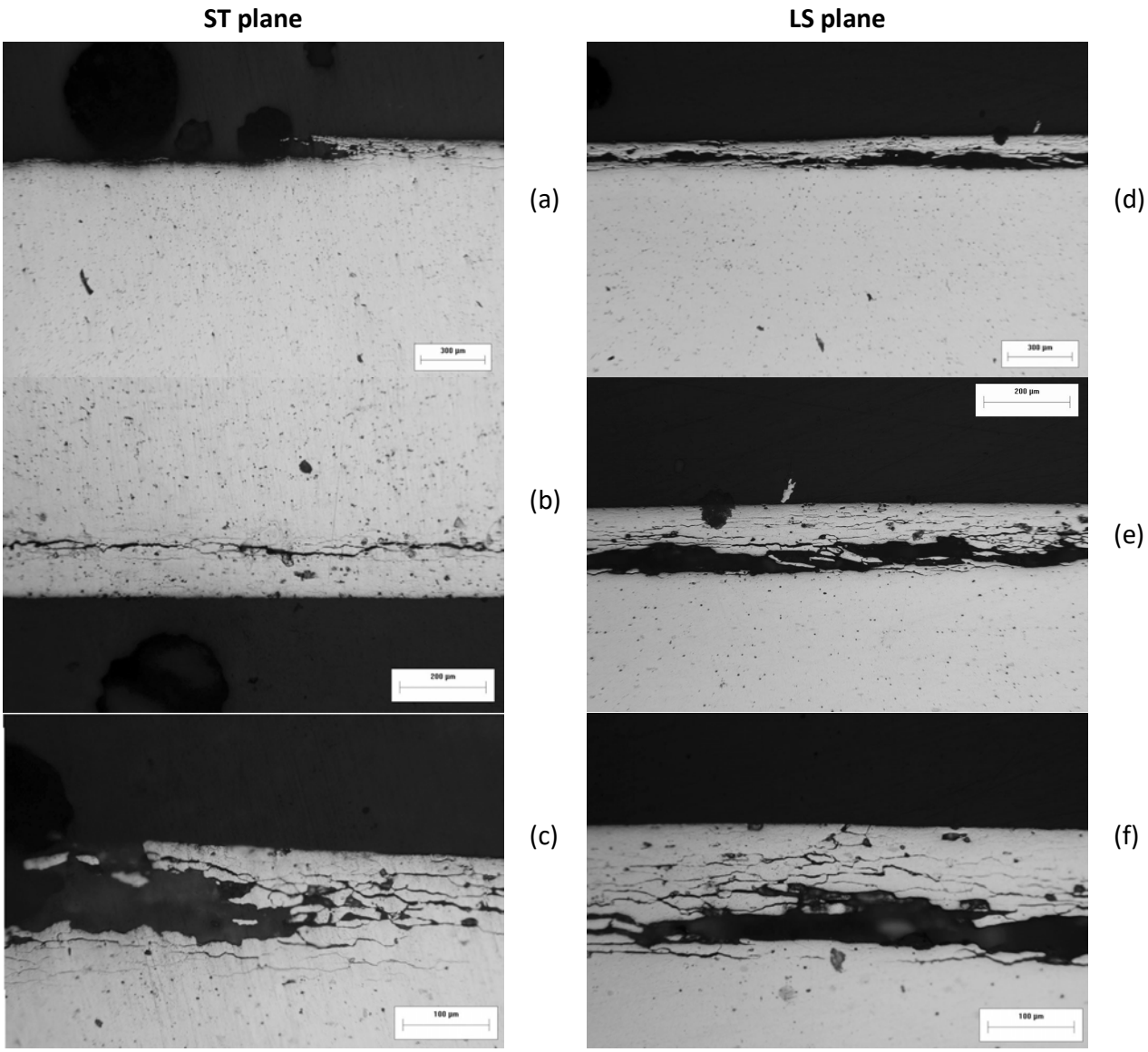

Fig. 4.12: Exfoliation corrosion for alloy 2024-T351 after aging for 4 h at T=170^{o}C. Images (a) to (c) depict exfoliation in the ST plane. Magnification is x50, x100, x200 respectively .Maximum depth of attack was measured 141,21 μm at fig (b) as illustrated in Table 4.

Aging time 6 hours

After 6 hours aging, the pit depth has ceased to increase, corrosion in the form of exfoliation is present but less severe than in the case of 4h of aging (Fig. 4.13). It is also observed the intergranular corrosion. Specifically Images (a) to (c) depict exfoliation in the ST plane. Magnification is x50,x100,x200 and the pits have a maximum depth of 126 μm (Fig. 4.13c).

Images (d) to (f) depict exfoliation in the LS plane. Magnification is x50, x100 and x200, and the maximum depth of attack was measured 173 μm at fig (d).

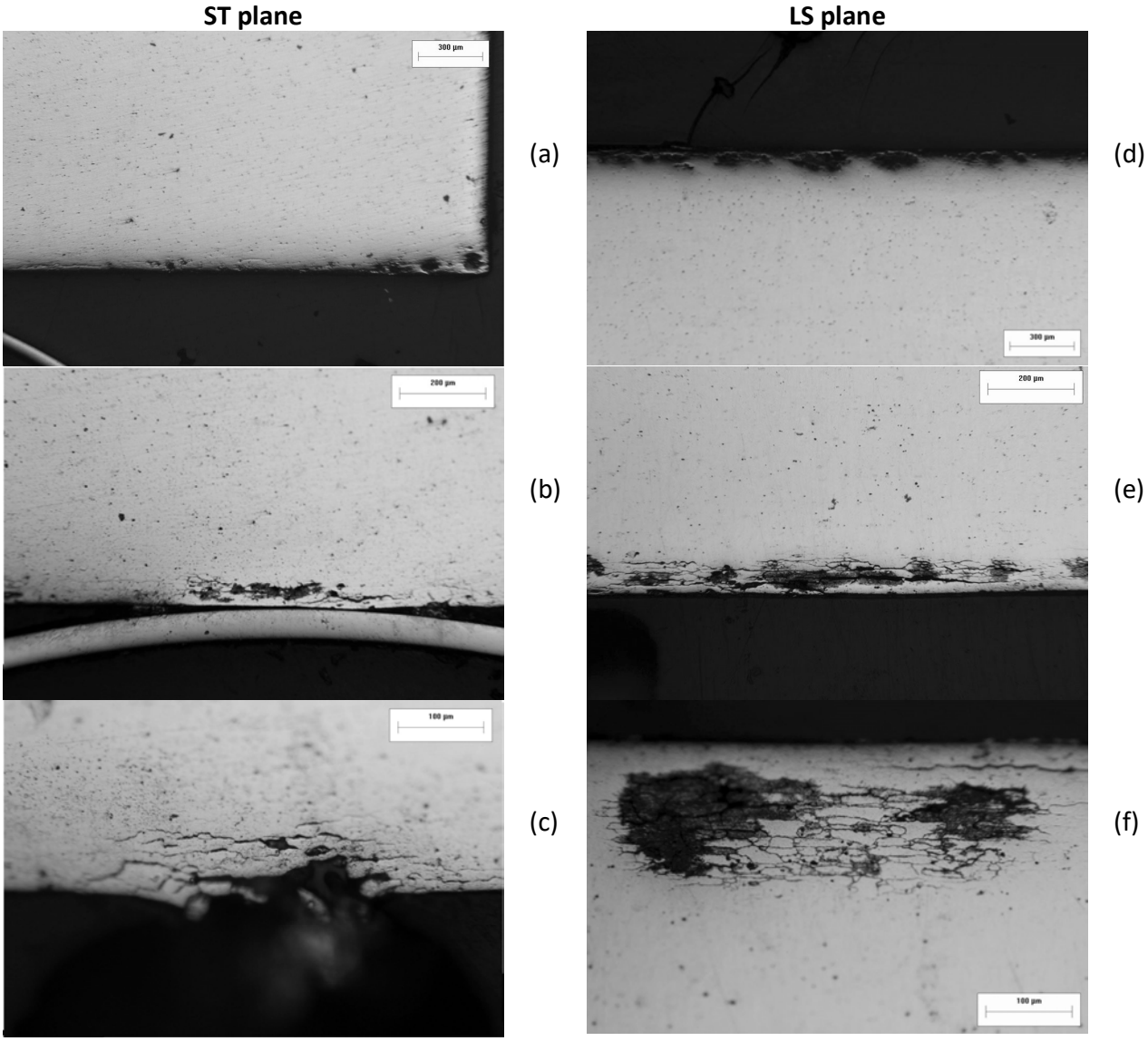

Fig. 4.13: Exfoliation corrosion for alloy 2024-T351 after aging for 6 h at T=170^{o}C. Images (a) to (c) depict exfoliation in the ST plane. Magnification is x50, x100, x200 respectively. Maximum depth of attack was measured 126,0610 μm, at fig(a) as illustrated in Table 4.

Aging time 9 hours

After 9 hours aging, the pit depth has totally ceased to increase. It is also observed that larger areas of the material have been removed due to exfoliation action. Specifically Images (a) to (c) depict exfoliation in the ST plane. Magnification is x50, x100, x200 and the pits have a maximum depth of 93 μm. Images (d) to (f) depict exfoliation in the LS plane. Magnification is x50, x100 and x200, and the maximum depth of attack was measured 105 μm at (Fig4.14.f).

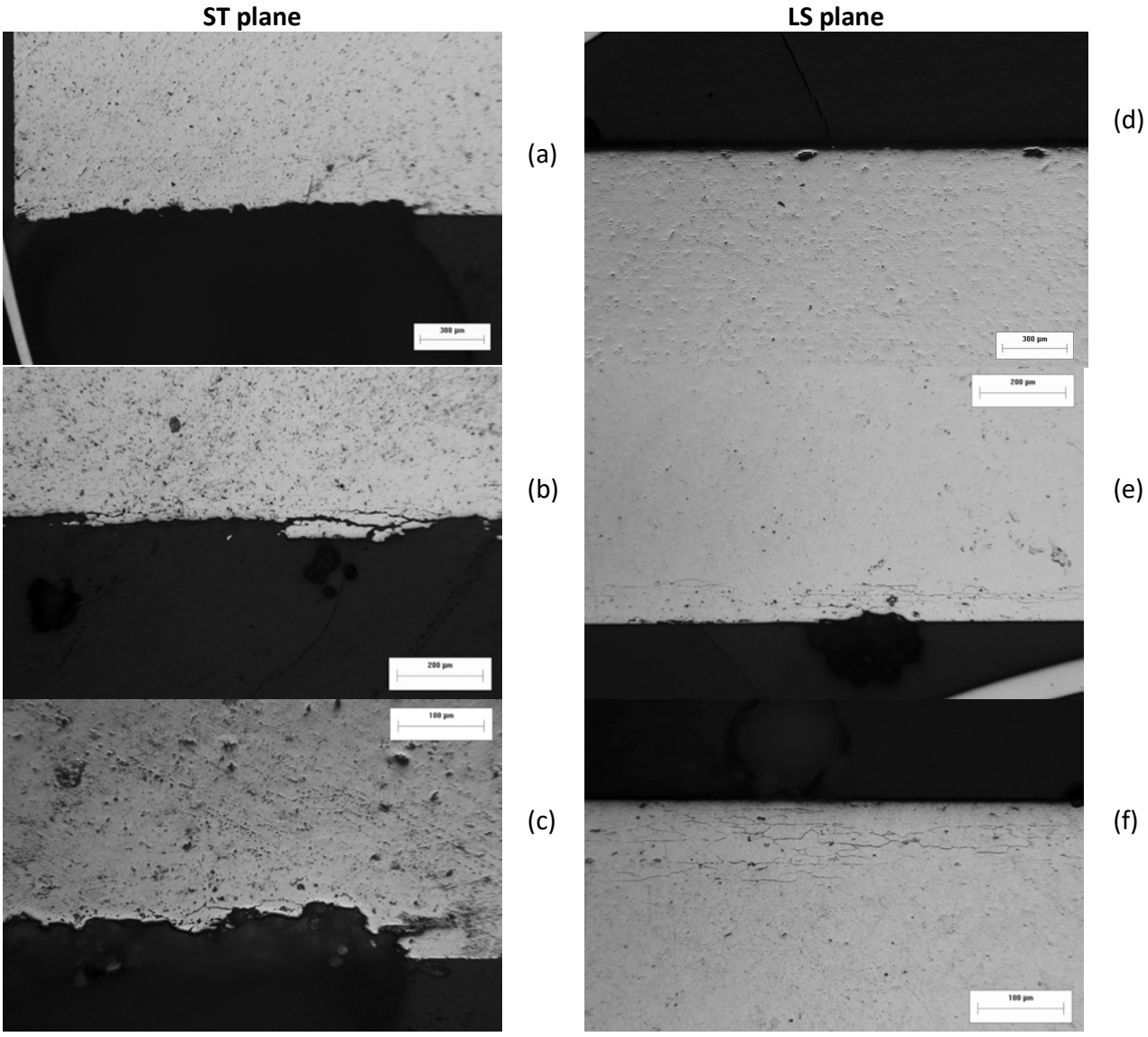

Fig4.14 Exfoliation corrosion for alloy 2024-T351 after aging for 9 h at T=170°C. Images (a) to (c) depict exfoliation in the ST plane. Magnification is x50, x100, x200 respectively. Maximum depth of attack was measured 93,94 μm, as illustrated in Table 4.

Aging time 15 hours

After 15 hours aging at T=170°C, the intergranular corrosion is observed clearly. Images (a) to (c) depict exfoliation in the ST plane. Magnification is x50, x100, x200 respectively. Maximum depth of attack was measured 114 μm at (Fig. 4.15.d). Images (d) to (f) depict exfoliation in the LS plane. Magnification is x50, x100, x200 respectively. Maximum depth of attack was measured 128 μm at (Fig. 4.15.f).

ST plane **LS plane**

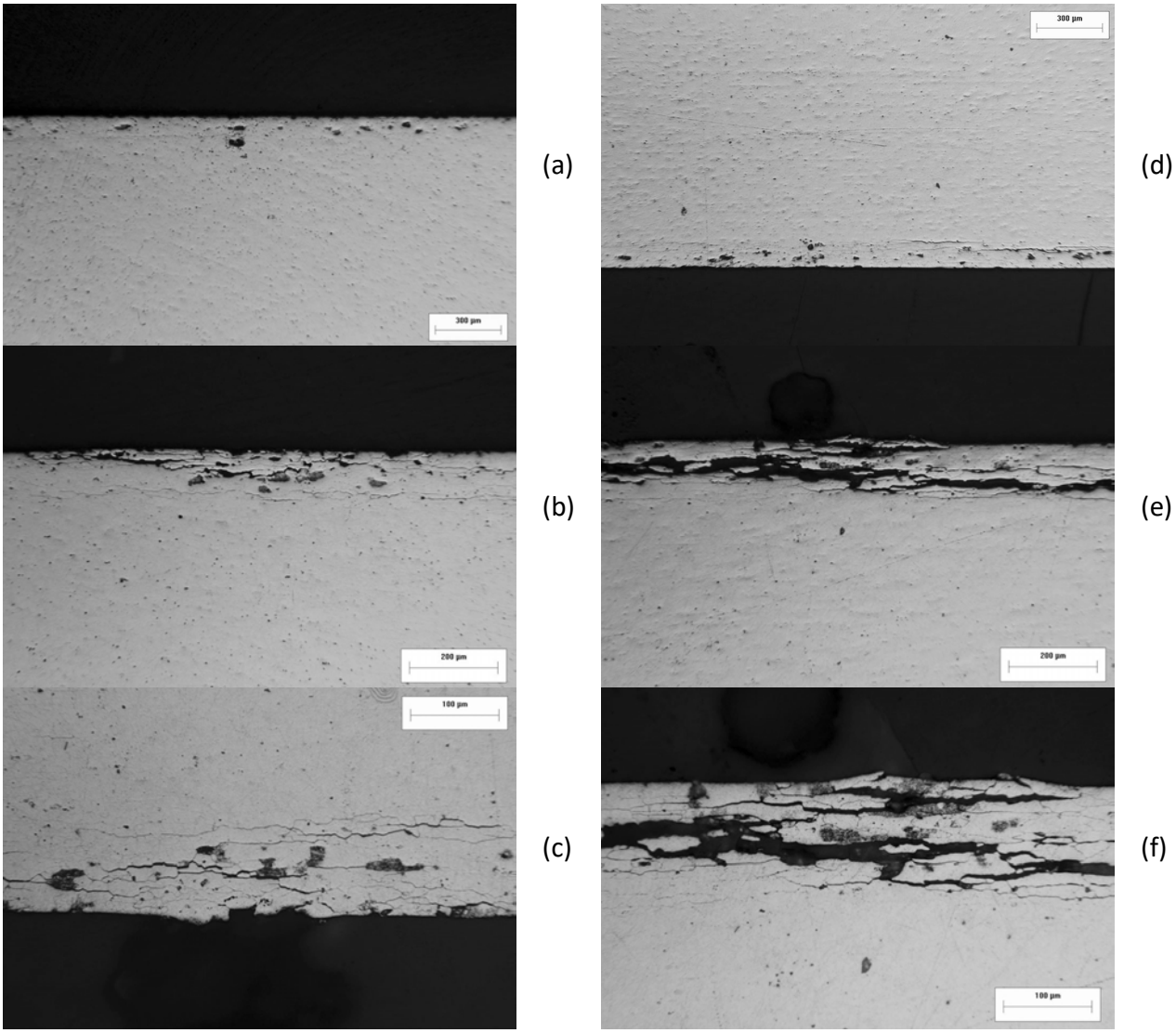

Fig. 4.15. Exfoliation corrosion for alloy 2024-T351 after aging for 15 h at T=170°C. Images (a) to (c) depict exfoliation in the ST plane. Magnification is x50, x100, x200 respectively. Maximum depth of attack was measured 114,25 μm at fig (d) as illustrated in Table 4.

Aging time 24 hours

After 24 hours aging at T=170°C, the maximum depth of attack was measured 113μm at fig (c) or 208,54 μm at fig.(a) in the ST plane and 110 μm, in the LS plane.

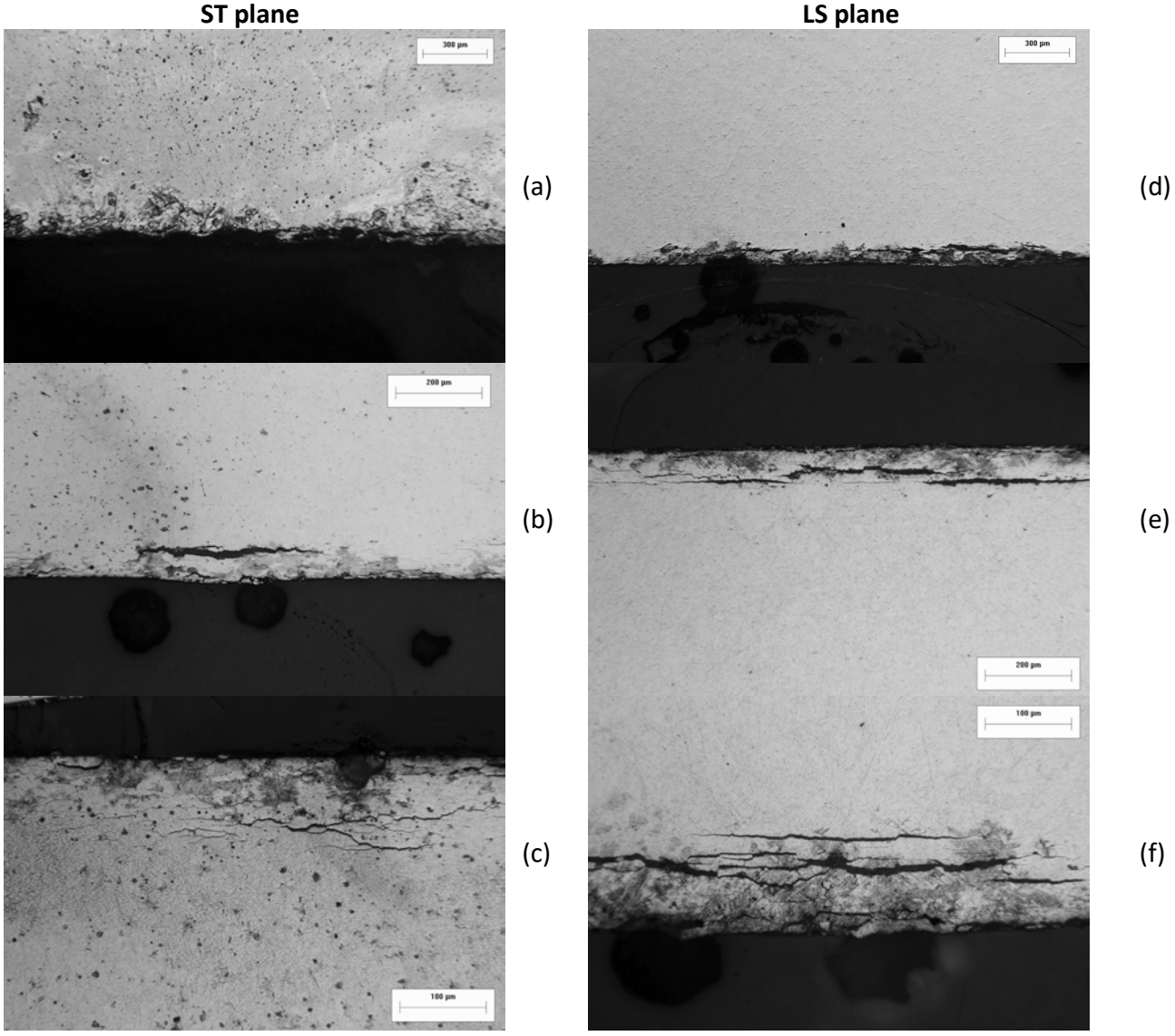

Fig.4.16 Exfoliation corrosion for alloy 2024-T351 after aging for 24 h at T=170°C. Images (a) to (c) depict exfoliation in the ST plane. Magnification is x50, x100, x200 respectively. Maximum depth of attack was measured 113,03 μm at fig.(c) or 208,54 μm at fig.(a) as illustrated in Table 4.

Aging time 48 hours

After 48 hours aging at T=170°C, the maximum depth of attack was measured 102 μm in the ST plane and 83 μm, in the LS plane.

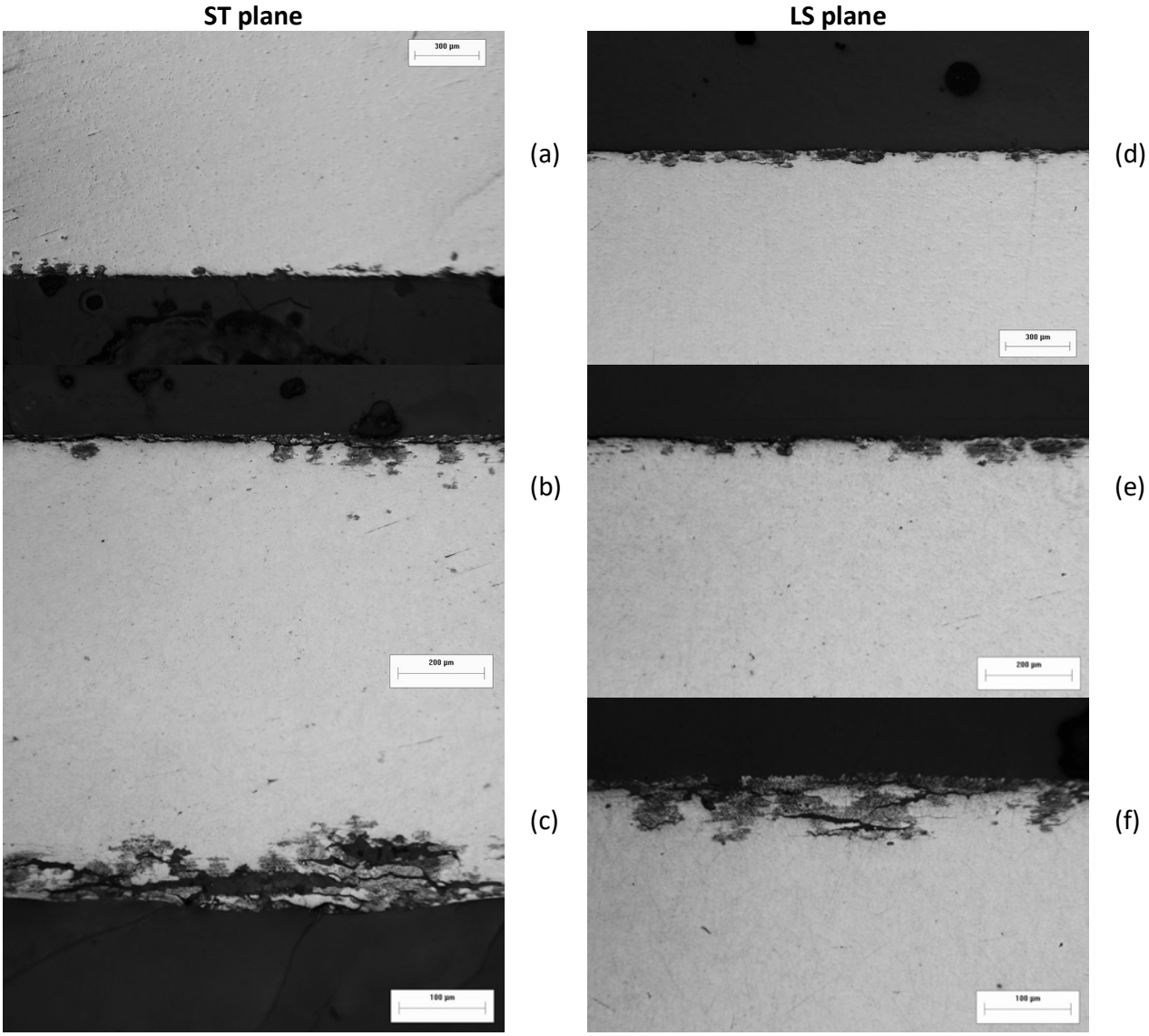

Fig4.17 Exfoliation corrosion for alloy 2024-T351 after aging for 48 h at T=170°C. Images (a) to (c) depict exfoliation in the ST plane. Magnification is x50, x100, x200 respectively. Maximum depth of attack was measured 102, 46 μm at fig (b) as illustrated in Table 4.

Aging time 63 hours

After 63 hours aging at T=170ºC, the maximum depth of attack was measured 186 μm in the ST plane and 90 μm, in the LS plane.

ST plane **LS plane**

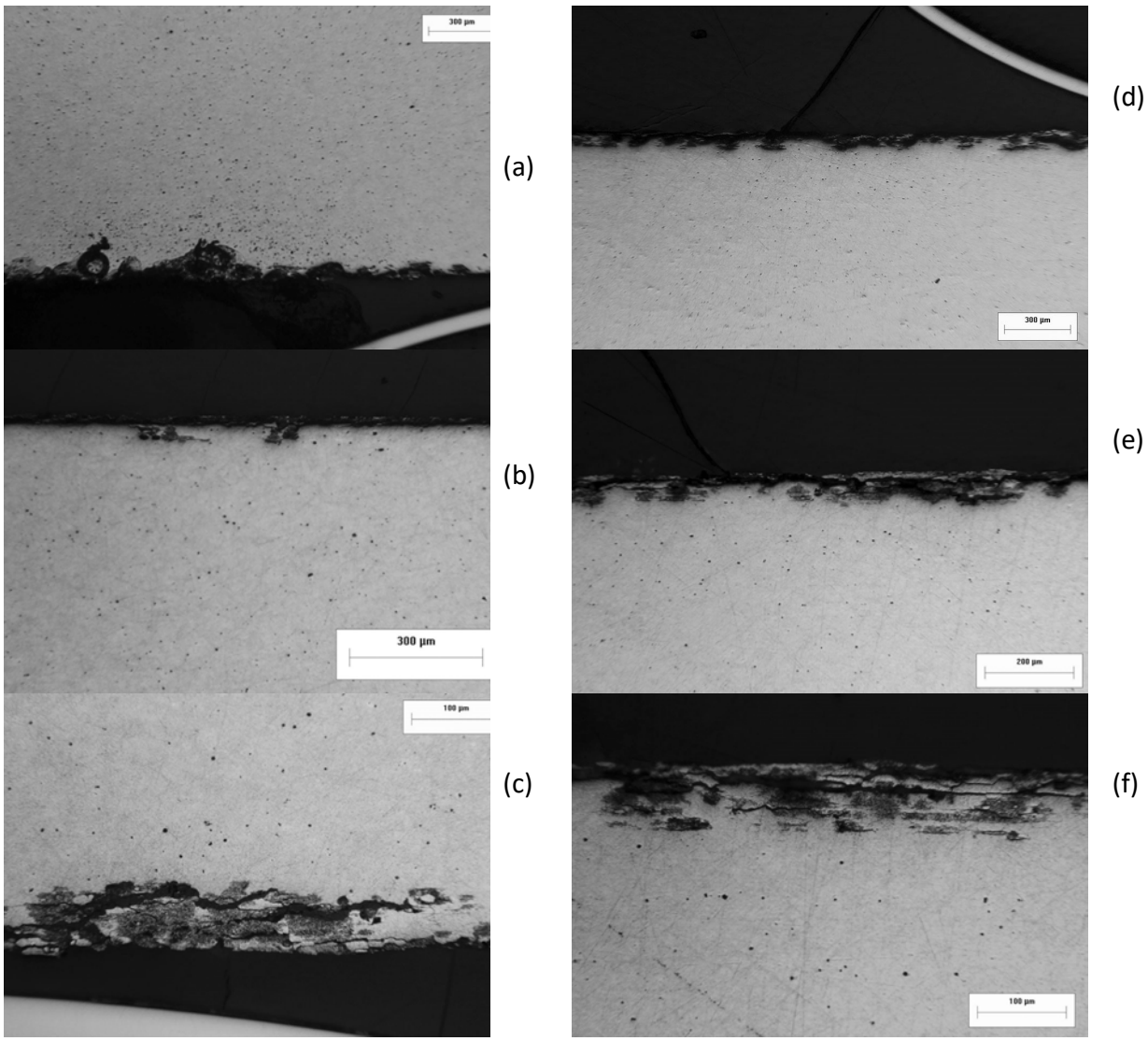

Fig.4.18 . Exfoliation corrosion for alloy 2024-T351 after aging for 63 h at T=170ºC. Images (a) to (c) depict exfoliation in the ST plane. Magnification is x50, x100, x200 respectively .Maximum depth of attack was measured 186.69 μm at fig (a) as illustrated in Table 4.

Aging time 98 hours

After 98 hours aging at T=170°C, the maximum depth of attack was measured 167 μm in the ST plane and 82 μm, in the LS plane.

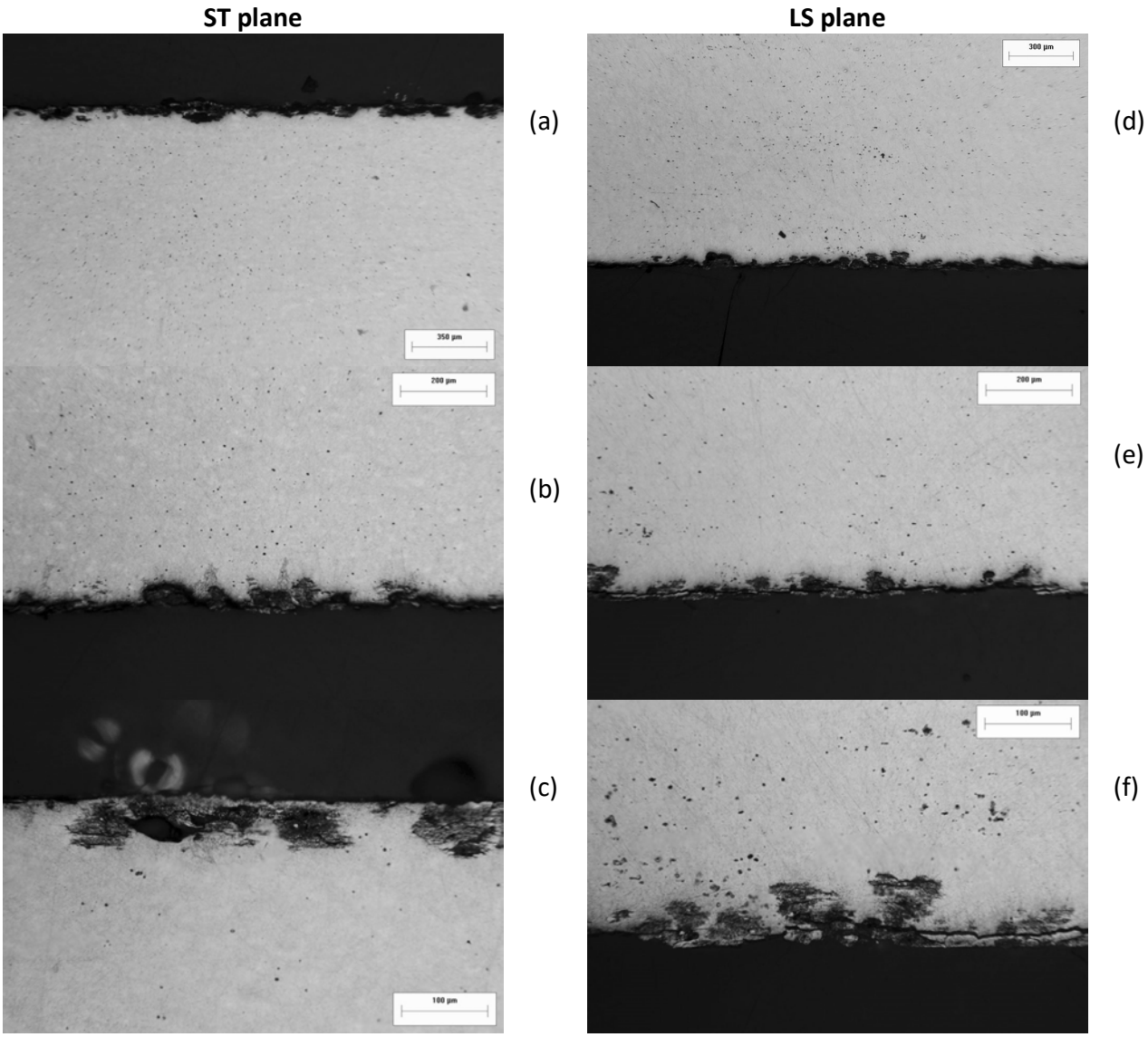

Fig.4.19 Exfoliation corrosion for alloy 2024-T351 after aging for 98 h at T=170°C. Images (a) to (c) depict exfoliation in the ST plane. Magnification is x50, x100, x200 respectively. Maximum depth of attack was measured 167,27 μm. Images (d) to (f) depict exfoliation in the LS plane. Magnification is x50, x100, x200 respectively. Maximum depth of attack was measured 82,92 μm.

In table 4 the maximum depth of attack versus aging time for the ST and LS planes is presented.

Table 4.Maximum depth of attack for the different times of aging and for the ST and LS side respectively, after 2 hours of EXCO exposure

Time	ST plane	LS plane
0.5 h	70,6	49,6
1 h	82,4	73,1
2 h	76,9	74,5
4 h	141,2	167,2
6h	126,0	173,0
9 h	93,9	105,4
15 h	114,2	128,4
24 h	113,0	110,3
48 h	102,4	83,3
63 h	186.6	90,2
98 h	167,2	83,9

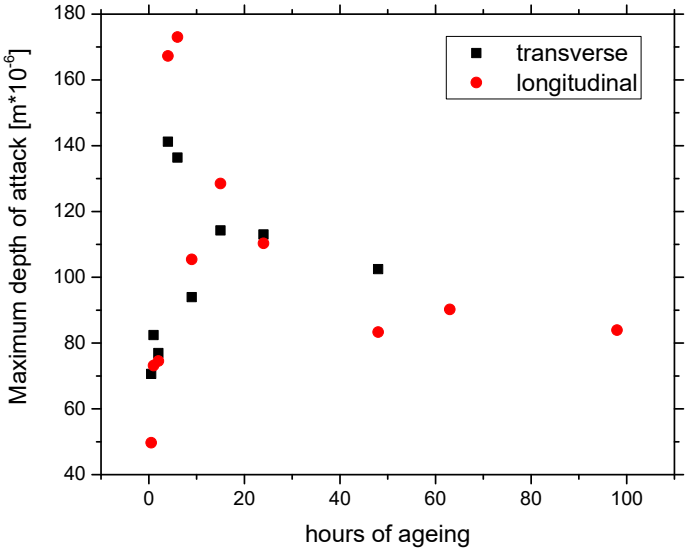

Fig. 4.20. Maximun depth of attack for the different times of aging for the ST and LS plane after 2 hours of EXCO exposure.

As is evident from figure 4.20 the depth of attack remains almost constant at 100μm, with a maximum between 4 and 6 hours of aging.

Fig. 4.21 and Fig 4.22 present the material weight loss versus aging time. The presentence of weight loss increases with increasing aging time.

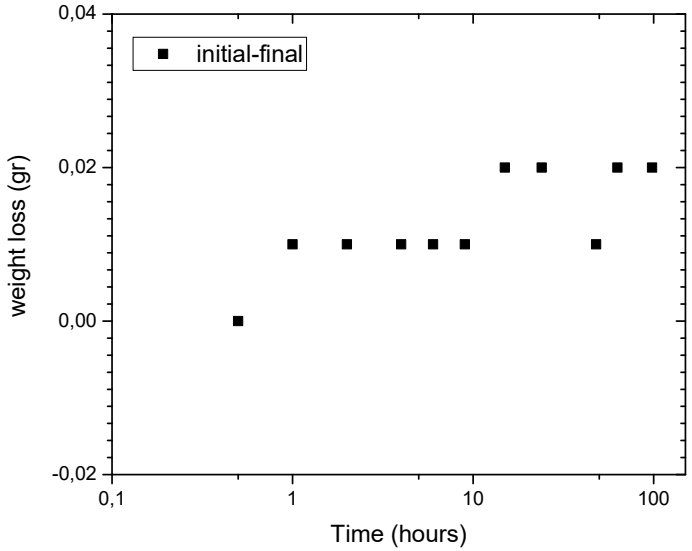

Fig. 4.21. Weight loss of the specimens, were introduced in the EXCO solution for 2 hours after aging in different conditions.

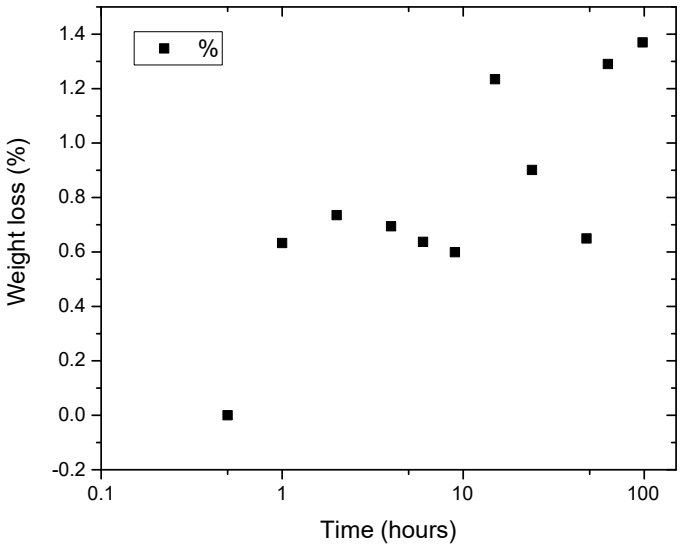

Fig. 4.22.Weight loss percentage of the specimens, were introduced in the EXCO solution for 2 hours after aging in different conditions.

Corrosion Exposure 24 Hours

As mentioned before, the depth-of-attack is defined as the maximum depth of the corrosion front, that has reached by a combination of aging and a certain exposure time in the EXCO solution. For 24h exposure the depth-of-attack could not be completely determined due to the effect of the corrosion. However it is observed the rapid growth of pits, as the aging time increases.

Aging time 30 min

After 30 min aging at T=170^{o}C and 24 h exposure in the exfoliation corrosion solution, the maximum depth of attack was measured 118μm in the ST plane and 54 μm, in the LS plane.

ST LS

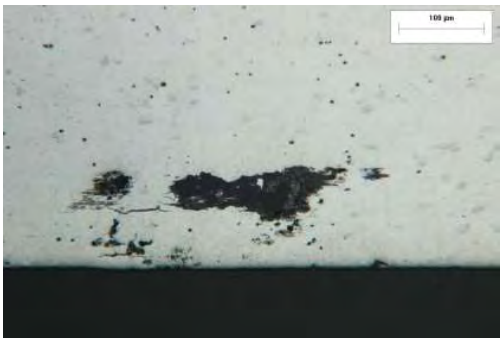

(a)

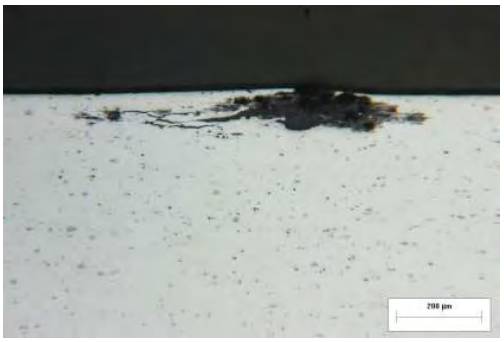

(b)

Fig.4.23: Exfoliation corrosion of 24h, for aluminum alloy 2024-T351, after aging for 30 min at T=170oC. Image (a) depicts exfoliation in the ST plane. Magnification is x200. Maximum depth of attack was measured 118,78 μm at fig (a) .Images (d) to (f) depict exfoliation in the LS plane. Magnification is x50, x100, x200 respectively. Maximum depth of attack was measured 54,54 μm at fig (b) .

Aging time 1 h

After 1 h aging at T=170^{o}C and 24 h exposure in the exfoliation corrosion solution, the maximum depth of attack was measured 165μm in the ST plane and 220 μm, in the LS plane. It is obvious, that the depth of attack is much bigger than the one exposed 2 h in the EXCO solution.

ST plane **LS plane**

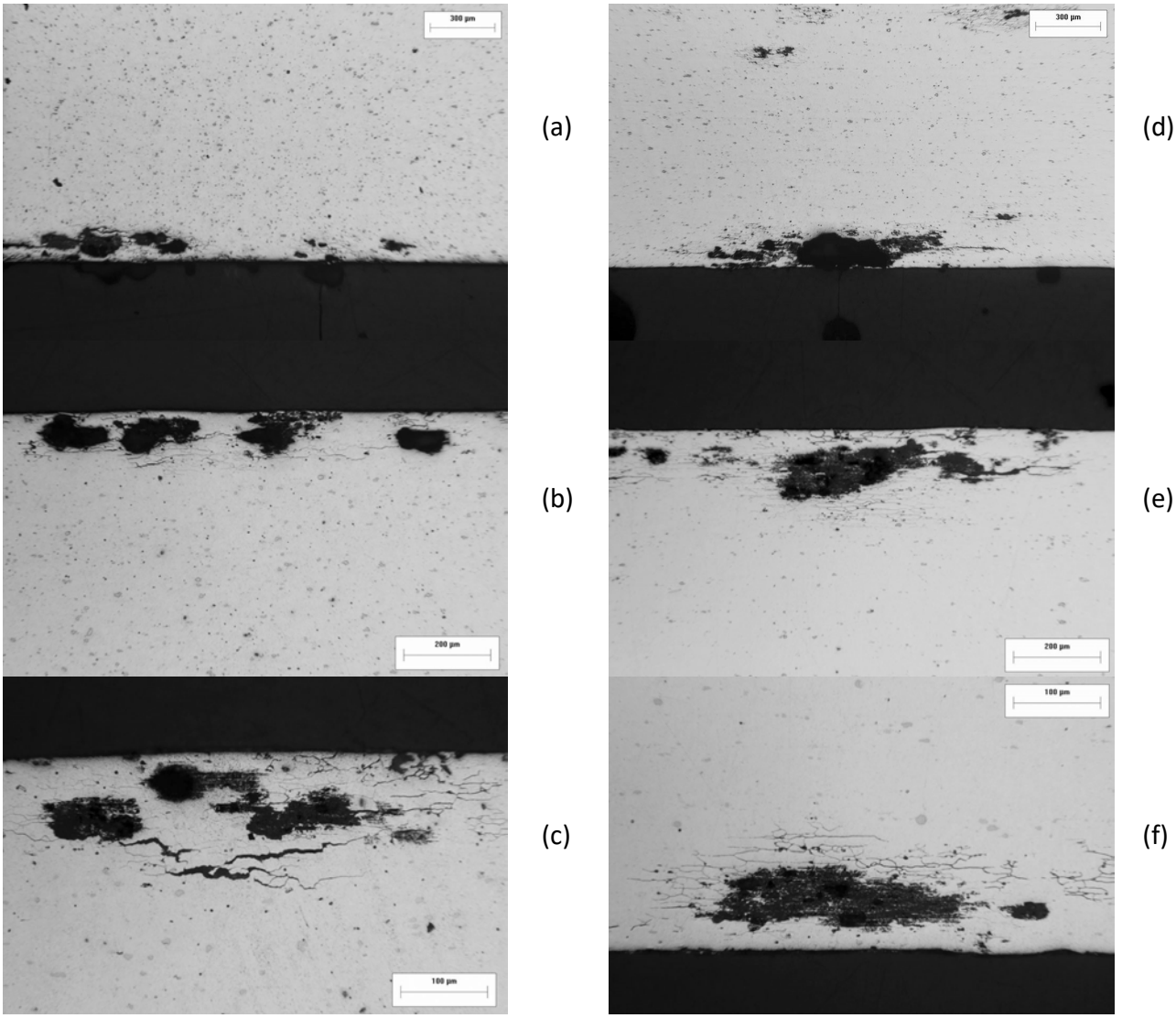

Fig.4.24: Exfoliation corrosion of 24h, for aluminum alloy 2024-T351, after aging for 1 hour at T=170^{o}C. Images (a) to (c) depict exfoliation in the ST plane. Magnification is x50, x100, x200 respectively. Maximum depth of attack was measured 165,85 μm at fig(a).Images (d) to (f) depict exfoliation in the LS plane. Magnification is x50, x100, x200 respectively. Maximum depth of attack was measured 220 μm at fig (e).

Aging time 2 h

After 2 h aging at T=170^{o}C and 24 h exposure in the exfoliation corrosion solution, the maximum depth of attack was measured 158 μm in the ST plane. The maximum depth of attack was not possible to be measured in the LS plane. The main reason was the substantial corrosion which affected the specimens.

ST LS

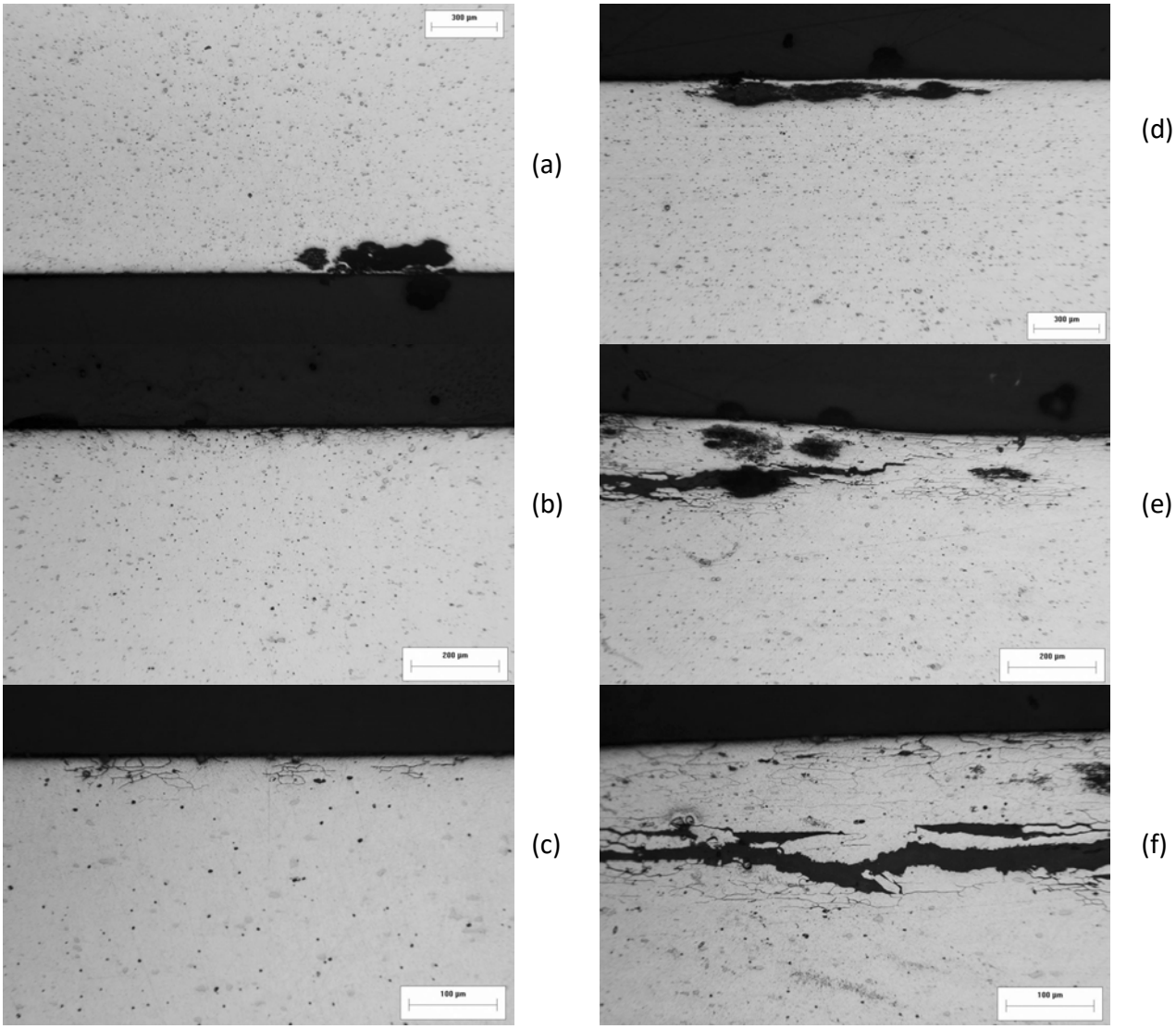

Fig.4.25: Exfoliation corrosion of 24h, for aluminum alloy 2024-T351, after aging for 2 hours at T=170^{o}C. Images (a) to (c) depict exfoliation in the ST plane. Magnification is x50, x100, x200 respectively. Maximum depth of attack was measured 158,53 μm at fig (a).Images (d) to (f) depict exfoliation in the LS plane. Magnification is x50, x100, x200 respectively.

Aging time 4 h

After 4 h aging at T=170^{o}C and 24 h exposure in the exfoliation corrosion solution, the maximum depth of attack was not possible to be measured neither in the LS nor in the ST plane. The main reason, was the substantial corrosion which affected the specimens

ST plane **LS plane**

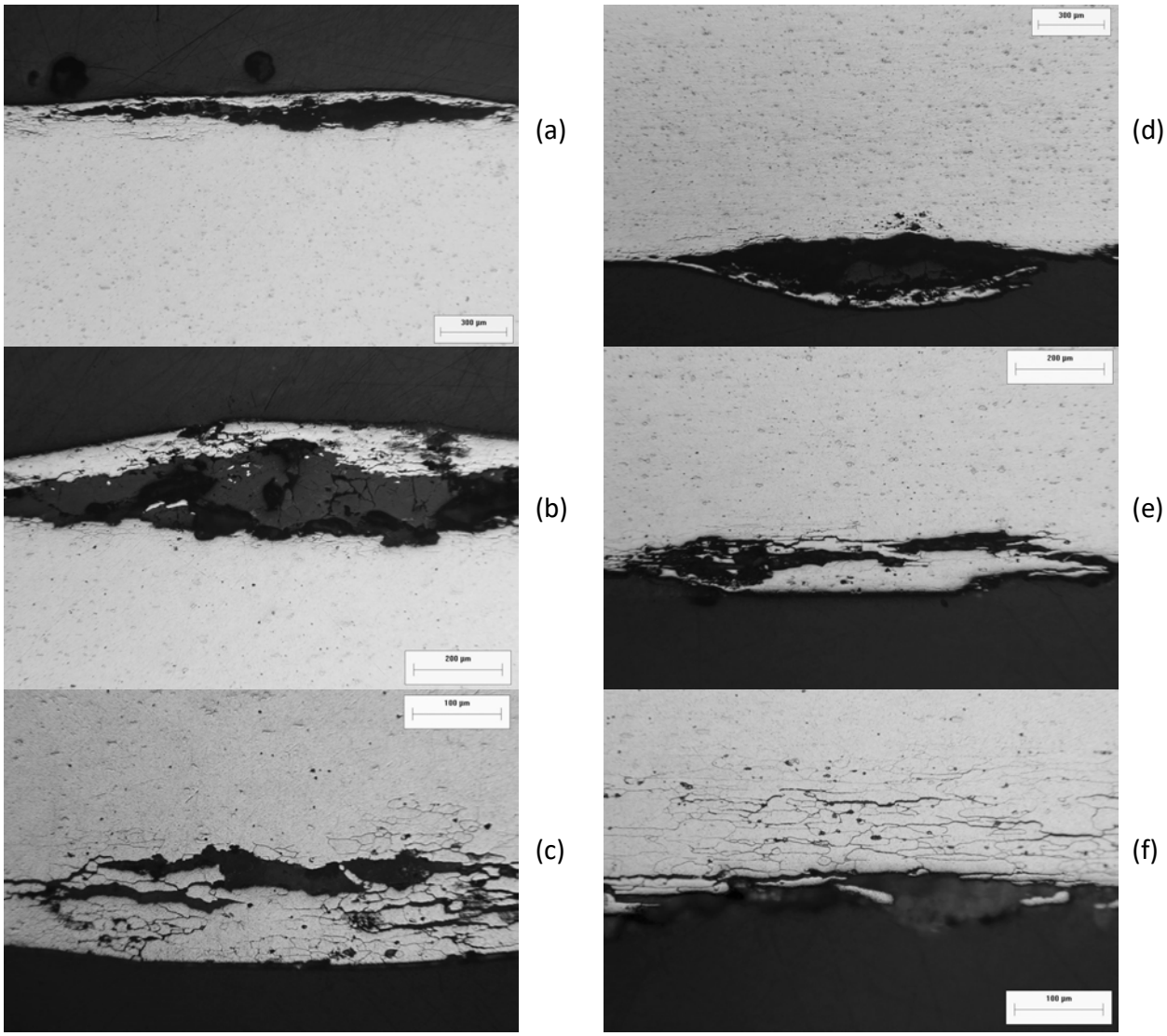

Fig.4.26: Exfoliation corrosion of 24h, for aluminum alloy 2024-T351, after aging for 4 hours at T=170^{o}C. Images (a) to (c) depict exfoliation in the ST plane. Magnification is x50, x100, x200 respectively. Images (d) to (f) depict exfoliation in the LS plane. Magnification is x50, x100, x200 respectively.

Aging time 6 h

After 6 h aging at T=170^{o}C and 24 h exposure in the exfoliation corrosion solution, the maximum depth of attack was not possible to be measured neither in the LS nor in the ST plane. The main reason, was the substantial corrosion which affected the specimens

ST plane **LS plane**

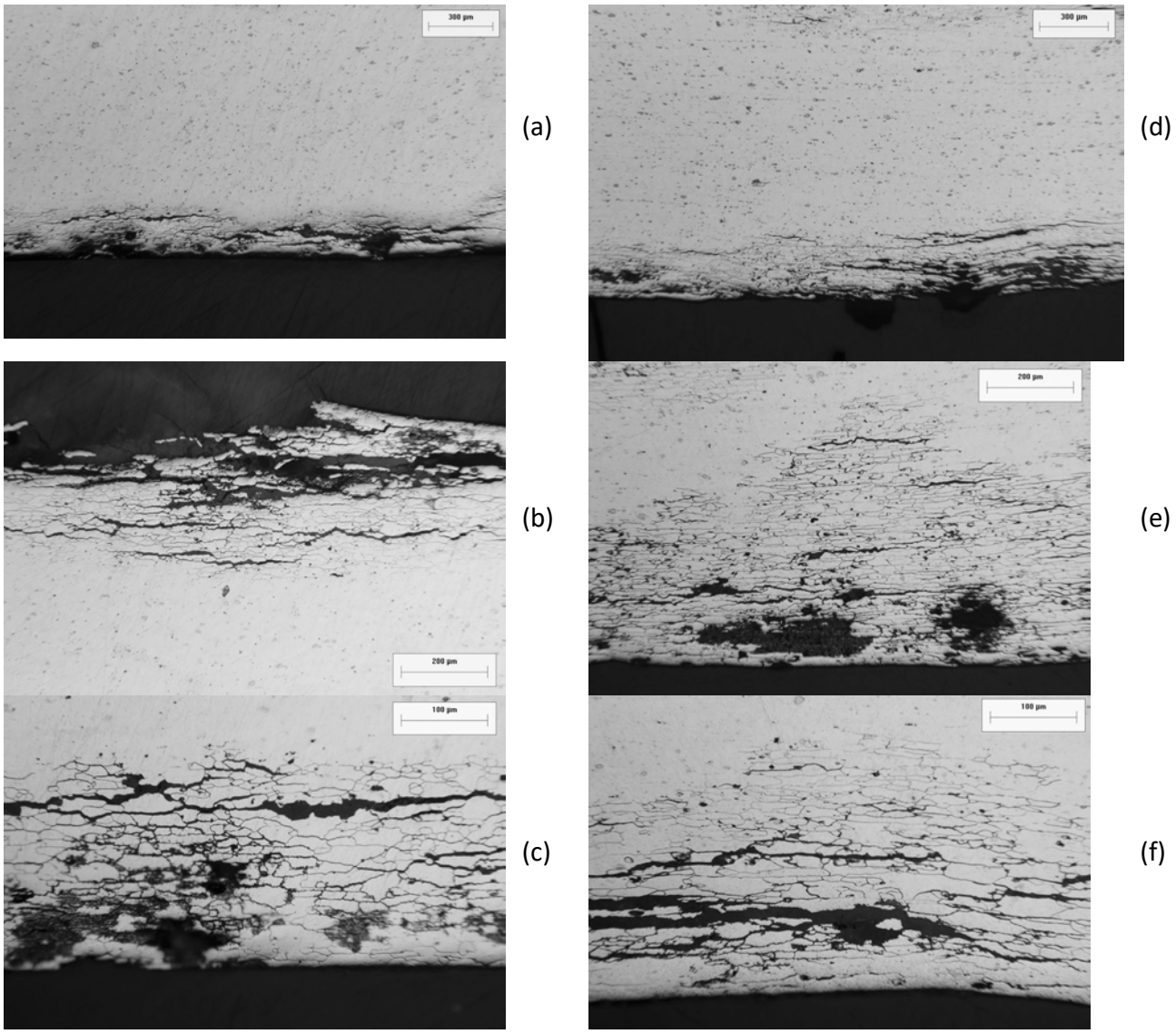

Fig.4.27: Exfoliation corrosion of 24h, for aluminum alloy 2024-T351, after aging for 6 hours at T=170^{o}C. Images (a) to (c) depict exfoliation in the ST plane. Magnification is x50, x100, x200 respectively. Images (d) to (f) depict exfoliation in the LS plane. Magnification is x50, x100, x200 respectively.

Aging time 9 h

After 9 h aging at T=170^{o}C and 24 h exposure in the exfoliation corrosion solution, the maximum depth of attack was not possible to be measured neither in the LS nor in the ST plane. The main reason, was the substantial corrosion which affected the specimens

ST plane **LS plane**

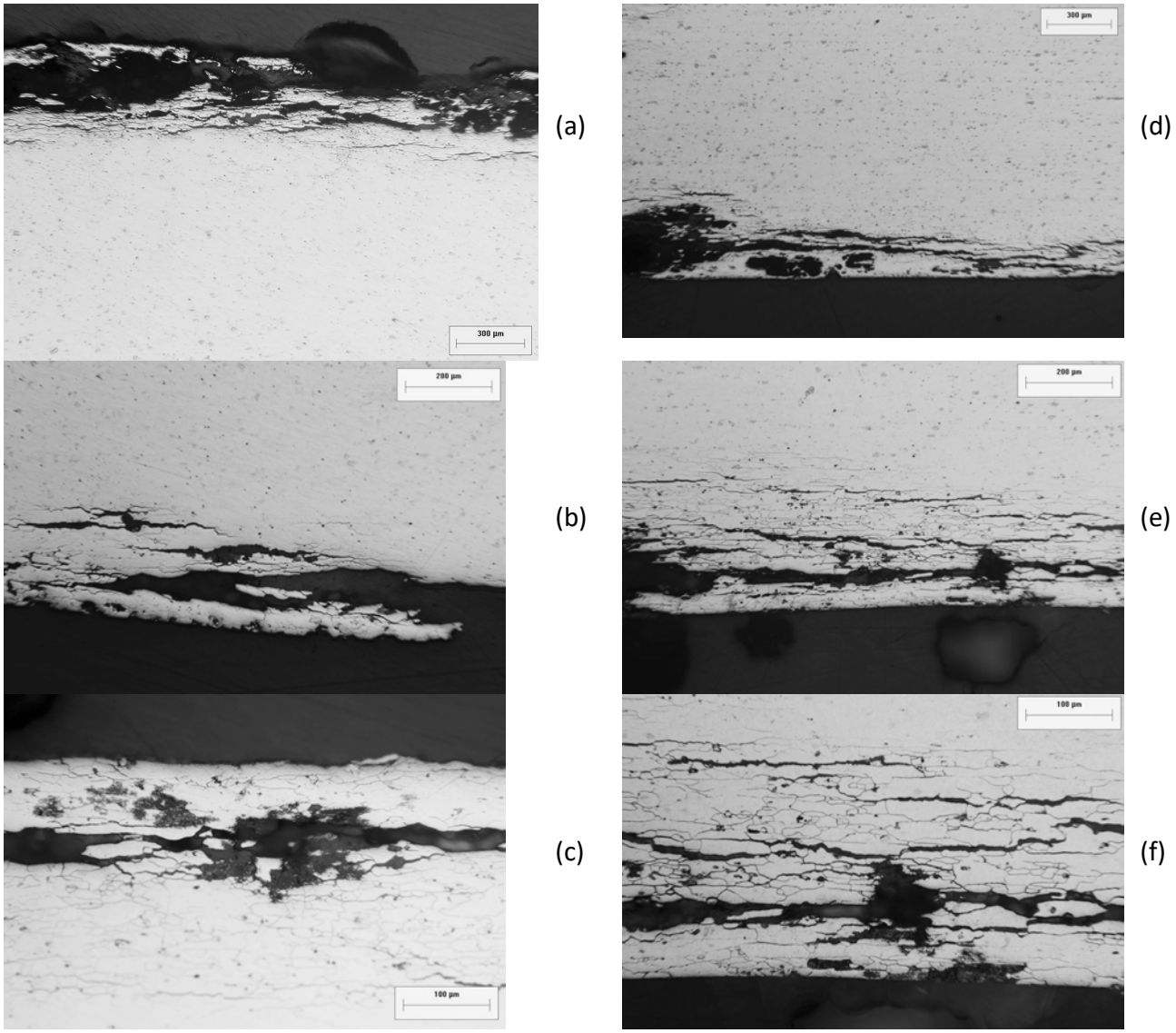

Fig.4.28: Exfoliation corrosion of 24h, for aluminum alloy 2024-T351, after aging for 9 hours at T=170^{o}C. Images (a) to (c) depict exfoliation in the ST plane. Magnification is x50, x100, x200 respectively. Images (d) to (f) depict exfoliation in the LS plane. Magnification is x50, x100, x200 respectively.

Aging time 15 h

After 15 h aging at T=170^{o}C and 24 h exposure in the exfoliation corrosion solution, the maximum depth of attack was not possible to be measured neither in the LS nor in the ST plane. The main reason, was the substantial corrosion which affected the specimens

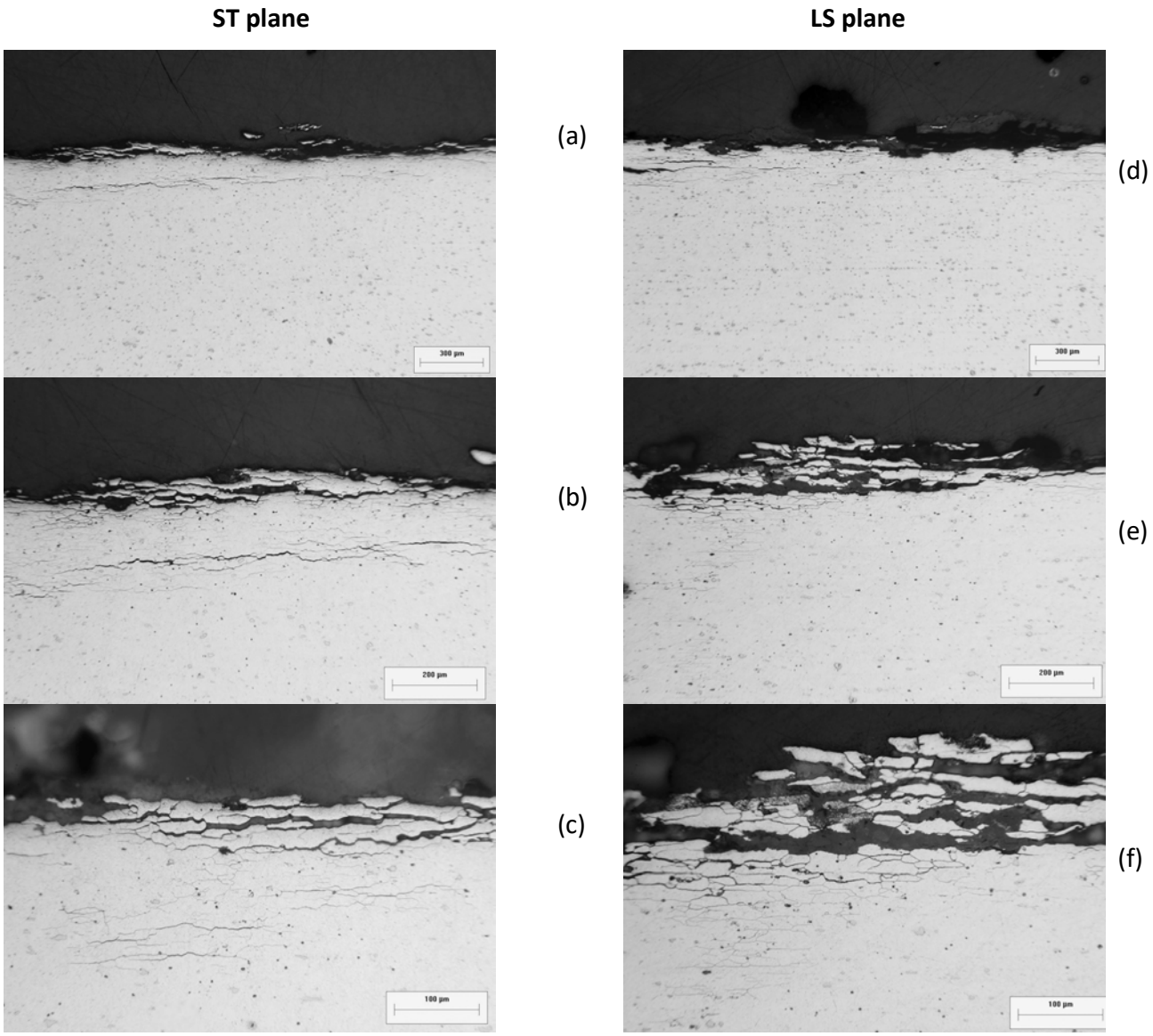

Fig.4.29: Exfoliation corrosion of 24h, for aluminum alloy 2024-T351, after aging for 15 hours at T=170^{o}C. Images (a) to (c) depict exfoliation in the ST plane. Magnification is x50, x100, x200 respectively. Images (d) to (f) depict exfoliation in the LS plane. Magnification is x50, x100, x200 respectively.

Aging time 24 h

After 24 h aging at T=170^{o}C and 24 h exposure in the exfoliation corrosion solution, the maximum depth of attack was not possible to be measured neither in the LS nor in the ST plane. The main reason, was the substantial corrosion which affected the specimens

ST plane **LS plane**

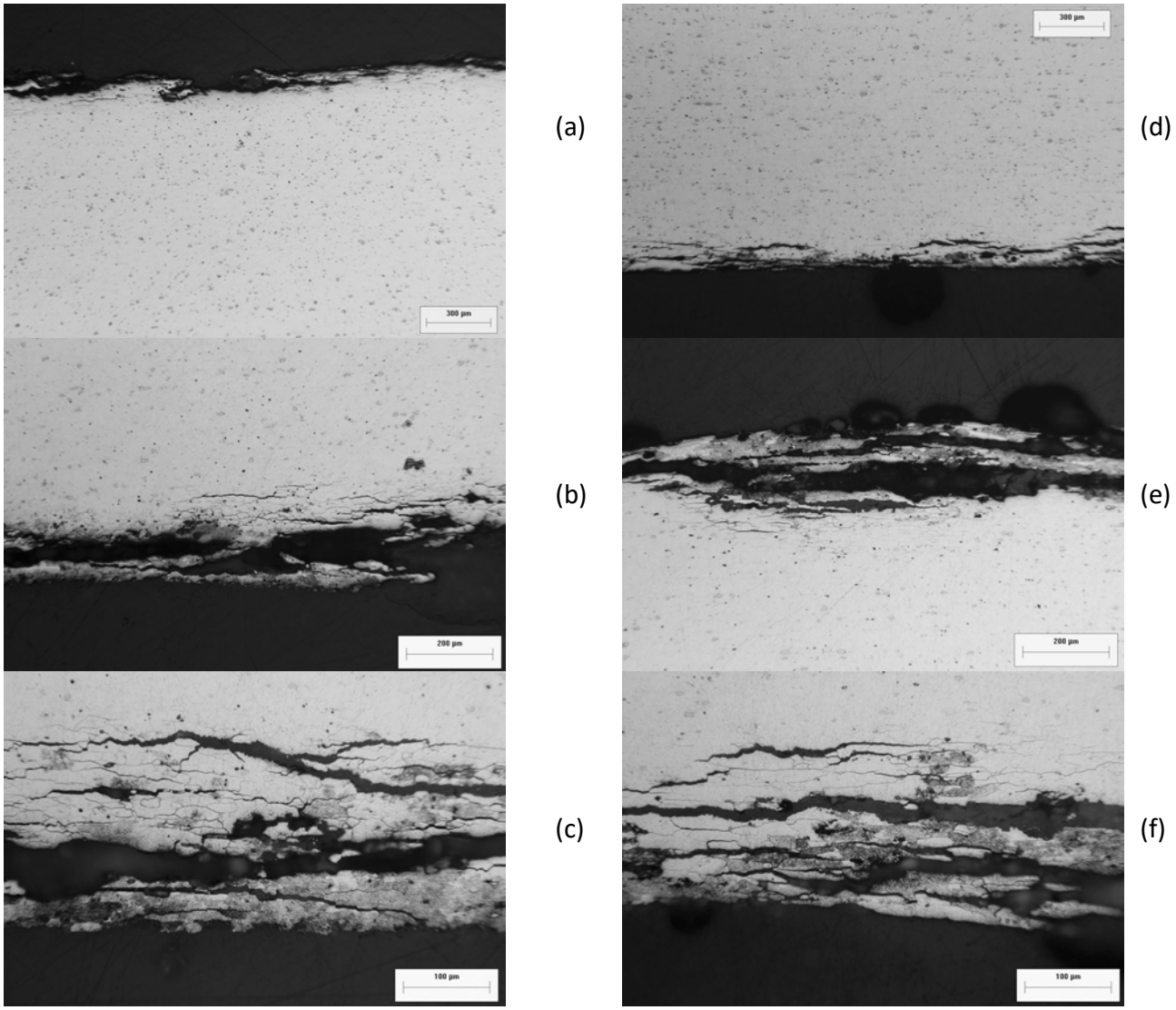

Fig.4.30: Exfoliation corrosion of 24h, for aluminum alloy 2024-T351, after aging for 24 hours at T=170^{o}C. Images (a) to (c) depict exfoliation in the ST plane. Magnification is x50, x100, x200 respectively. Images (d) to (f) depict exfoliation in the LS plane. Magnification is x50, x100, x200 respectively.

Aging time 48 h

After 48 h aging at T=170^{o}C and 24 h exposure in the exfoliation corrosion solution, the maximum depth of attack was not possible to be measured neither in the LS nor in the ST plane. The main reason, was the substantial corrosion which affected the specimens

ST plane **LS plane**

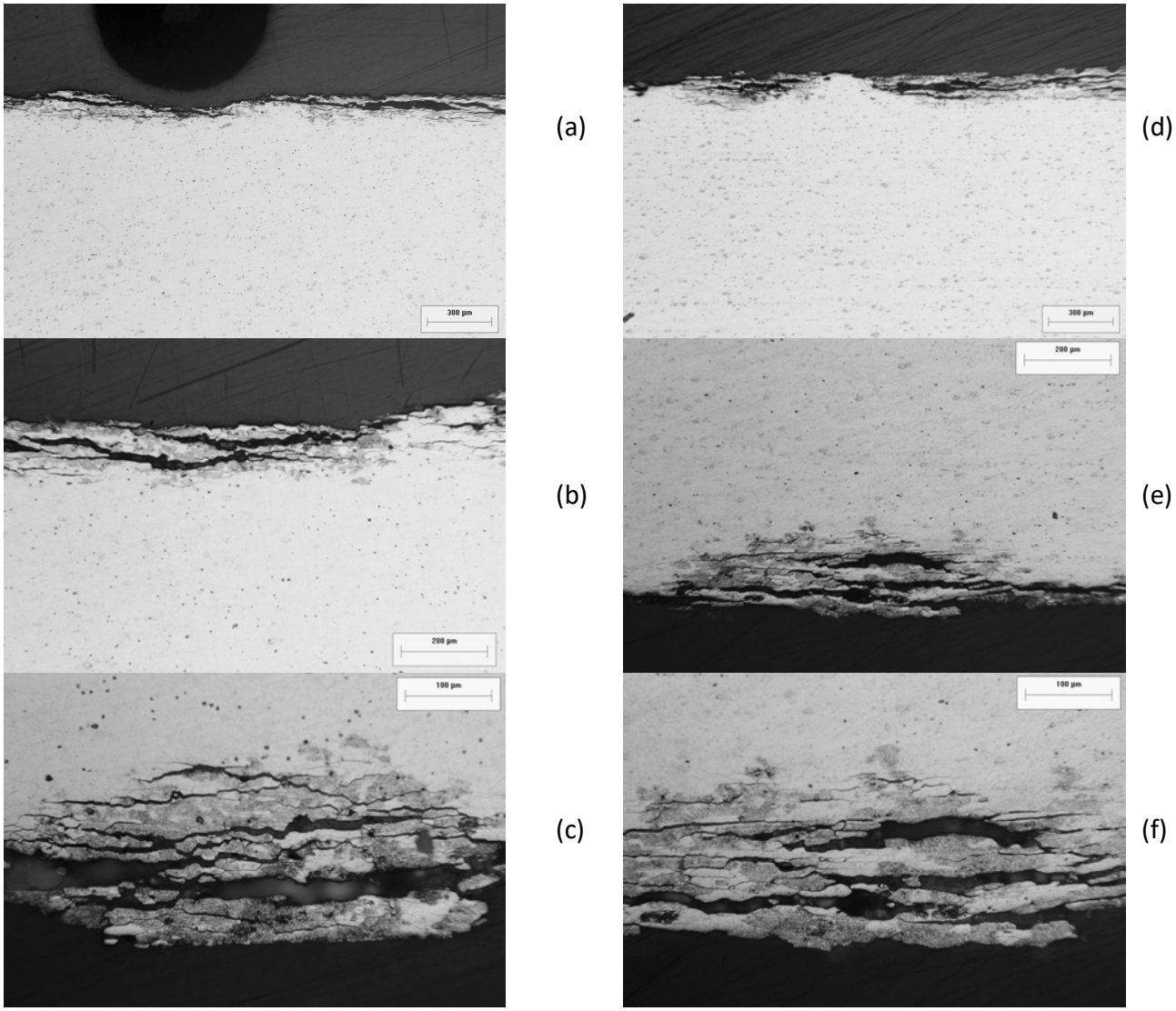

Fig.4.31: Exfoliation corrosion of 24h, for aluminum alloy 2024-T351, after aging for 48 hours at T=170^{o}C. Images (a) to (c) depict exfoliation in the ST plane. Magnification is x50, x100, x200 respectively. Images (d) to (f) depict exfoliation in the LS plane. Magnification is x50, x100, x200 respectively.

Aging time 63 h

After 63 h aging at T=170^{o}C and 24 h exposure in the exfoliation corrosion solution, the maximum depth of attack was not possible to be measured neither in the LS nor in the ST plane. The main reason, was the substantial corrosion which affected the specimens

ST plane **LS plane**

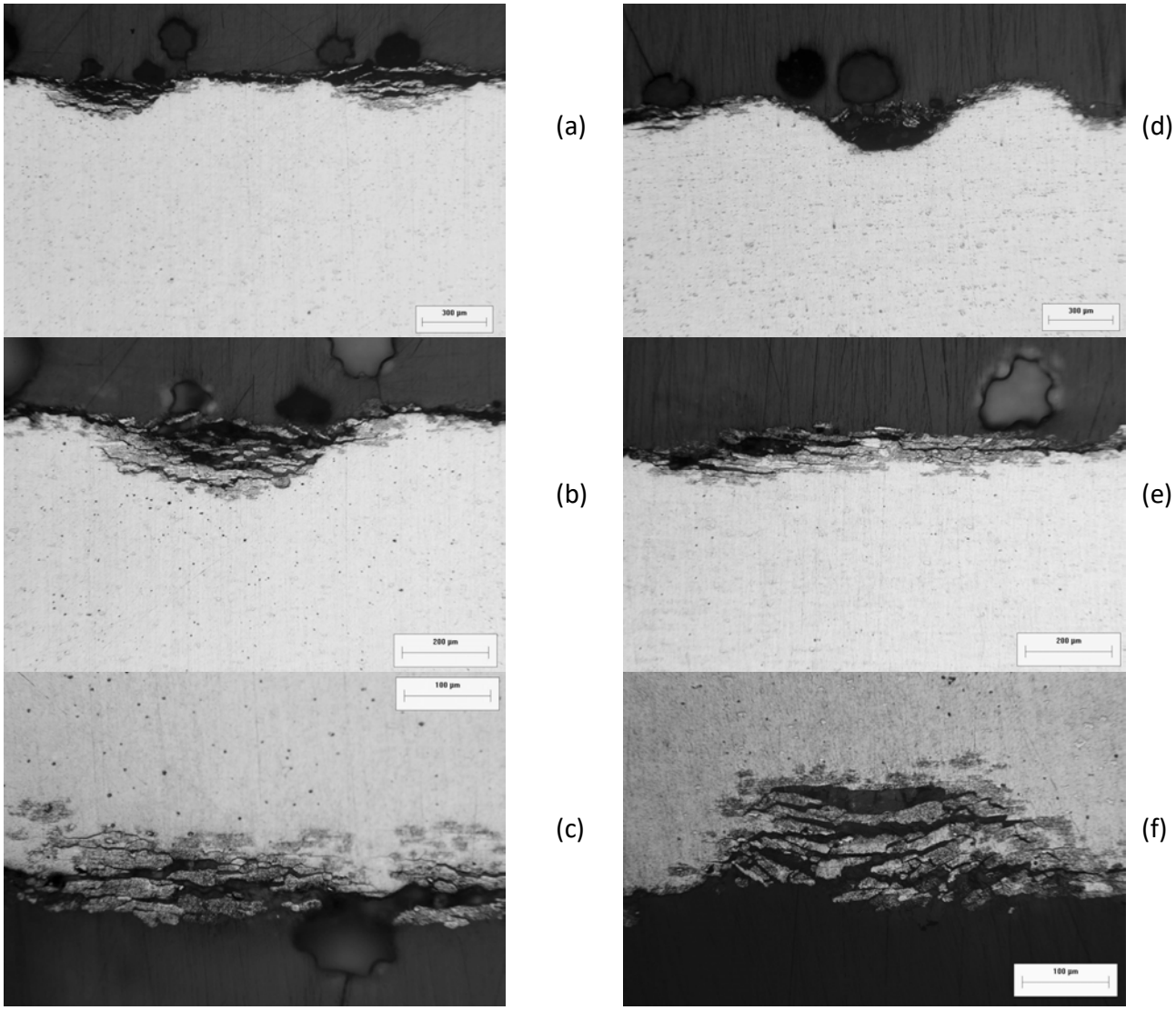

Fig.4.32: Exfoliation corrosion of 24h, for aluminum alloy 2024-T351, after aging for 63 hours at T=170^{o}C. Images (a) to (c) depict exfoliation in the ST plane. Magnification is x50, x100, x200 respectively. Images (d) to (f) depict exfoliation in the LS plane. Magnification is x50, x100, x200 respectively.

Aging time 98 h

After 98 h aging at T=170^{o}C and 24 h exposure in the exfoliation corrosion solution, the maximum depth of attack was not possible to be measured neither in the LS nor in the ST plane. The main reason, was the substantial corrosion which affected the specimens

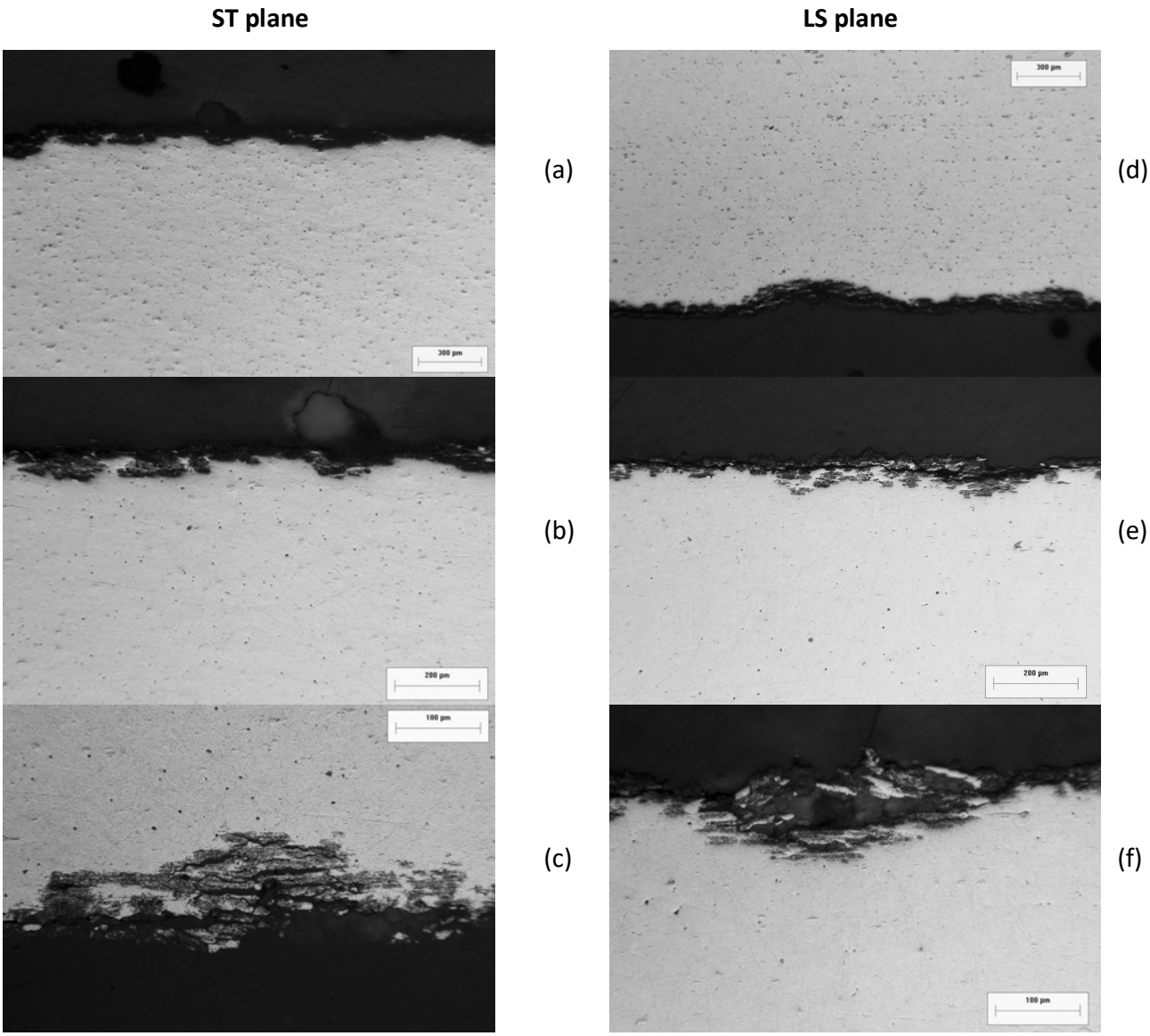

Fig.4.33: Exfoliation corrosion of 24h, for aluminum alloy 2024-T351, after aging for 98 hours at T=170ºC. Images (a) to (c) depict exfoliation in the ST plane. Magnification is x50, x100, x200 respectively. Images (d) to (f) depict exfoliation in the LS plane. Magnification is x50, x100, x200 respectively.

As stated earlier, it was not possible to measure the depth of attack for artificial aging and 24h exposure to EXCO. Fig. 4.34 and Fig 4.35 present the material weight loss versus aging time. The presentence of weight loss increases with increasing aging time.

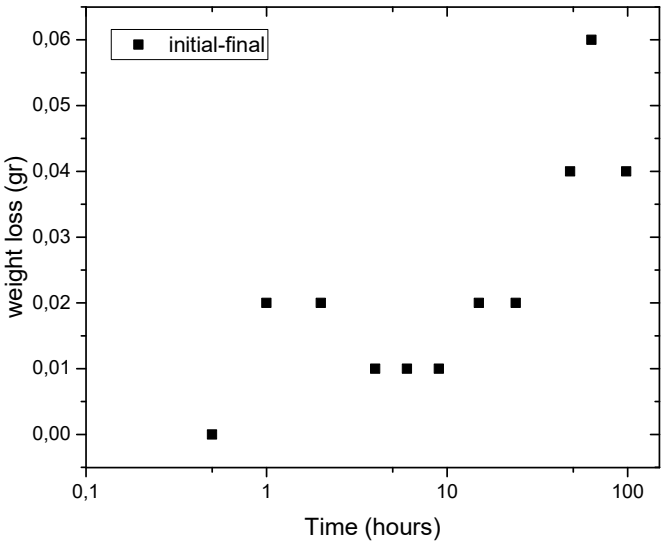

Fig. 4.34. Weight loss of the specimens, were introduced in the EXCO solution for 24 hours after aging in different conditions.

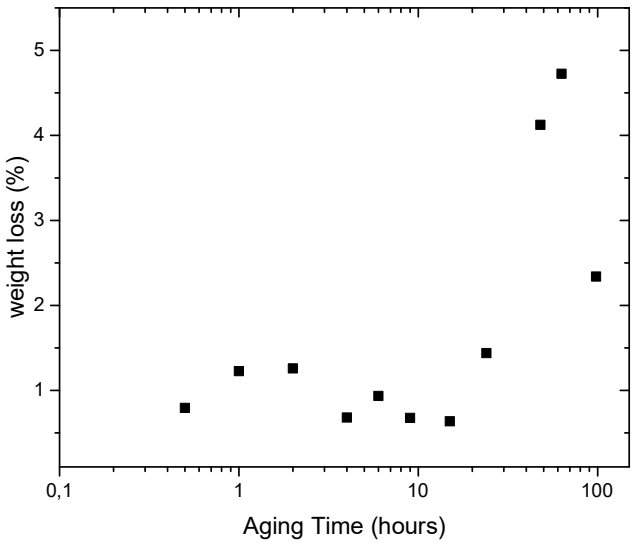

Fig. 4.35. Weight loss percentage of specimens, were introduced in the EXCO solution for 24 hours after aging in different conditions.

4.5 Scanning Electron Microscopy (SEM)

Surface analysis was performed to corroded specimens provided by the tests performed.

Corrosion Exposure 2 Hours

30 min aging

In Fig 4.36 the on start of pitting corrosion is apparent as well as the morphologies of several pits. Pits appear isolated.

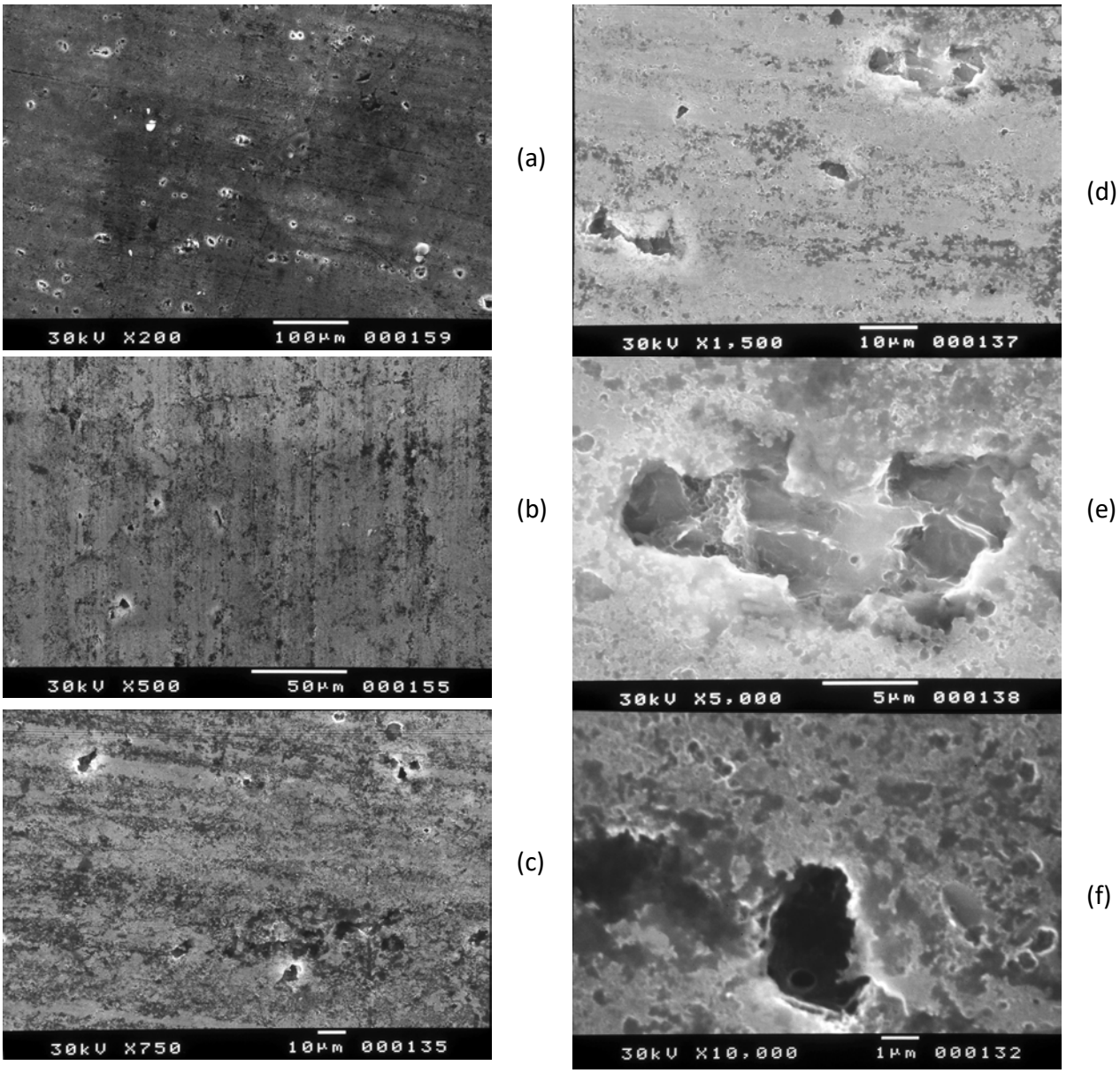

Fig. 4.36 : SEM topographies of alloy 2024-T351 after aging for 30 min at T=170°C and 2 hours exposure in the EXCO solution. Magnification is (a) x200, (b) x500, (c) x750, (d)x1500, (e)x5000 and (f) x10000 respectively .

1 hour aging

In Fig 4.37 pitting is the main corrosion mechanism with several pits forming groups.

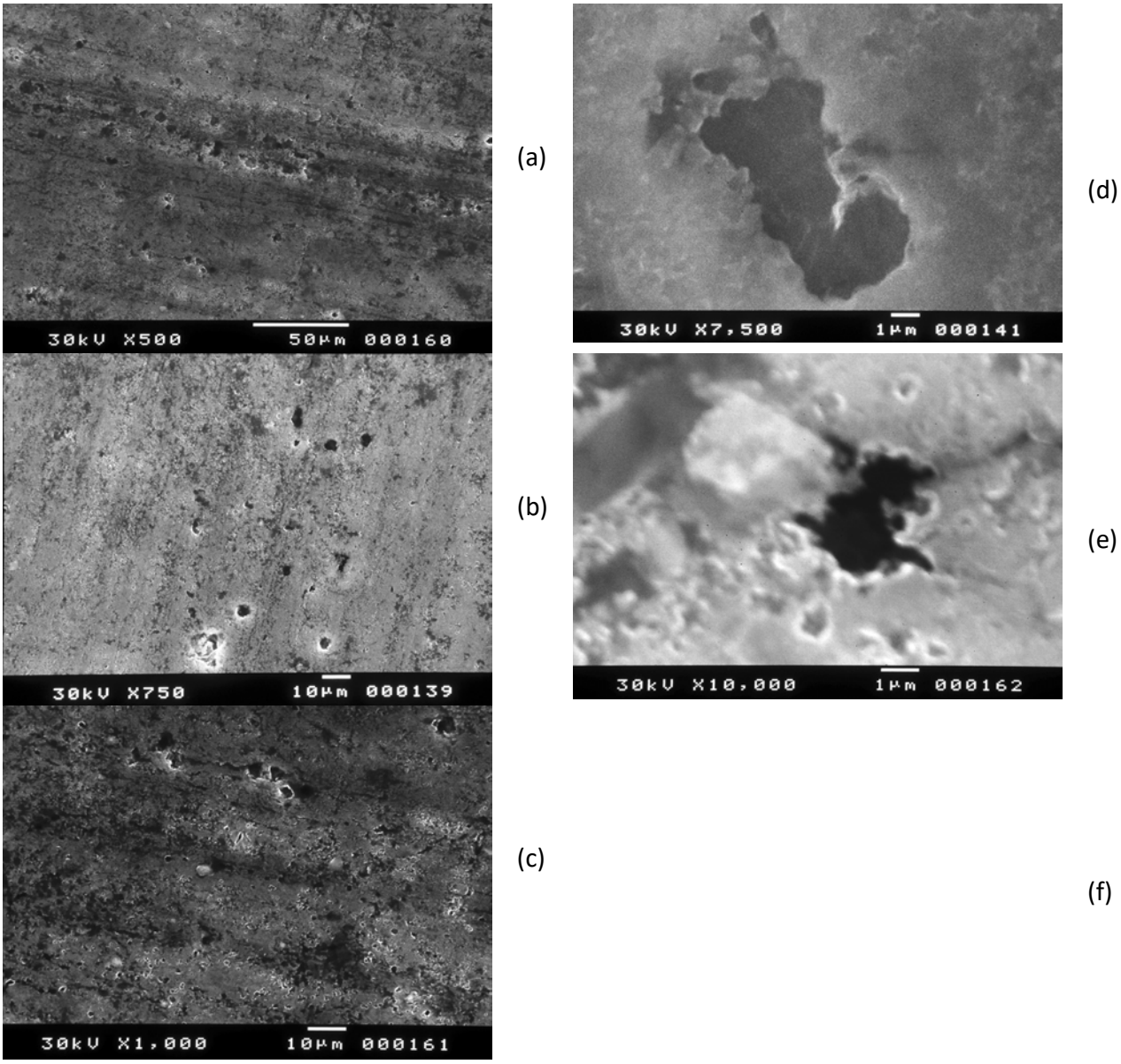

Fig. 4.37: SEM topographies of alloy 2024-T351 after aging for 1 h at T=170^{o}C and 2 hours exposure in the EXCO solution. Magnification is (a) x500, (b) x750, (c) x1000, (d) x7500 and (e) 10000 respectively.

2 hours aging

In Fig 4.38 pitting is the main corrosion mechanism with several pits forming groups. The corrosion mechanism is similar with 1h of aging.

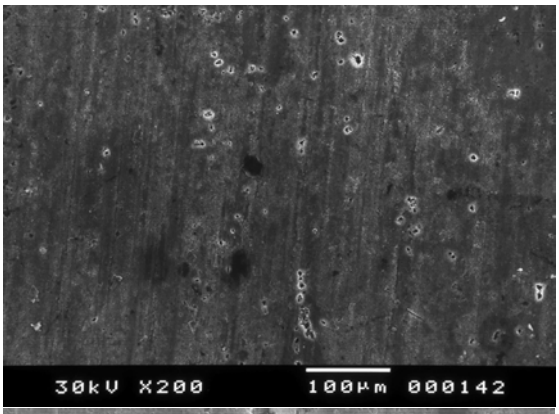

(a)

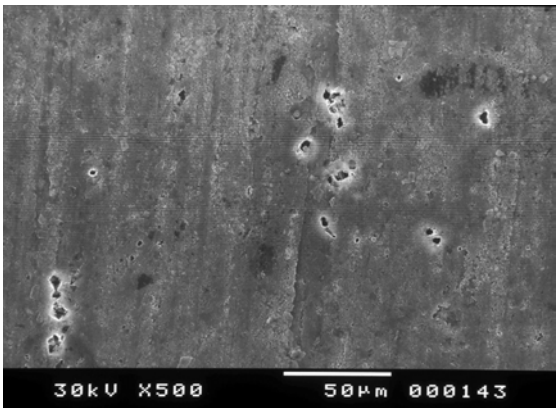

(d)

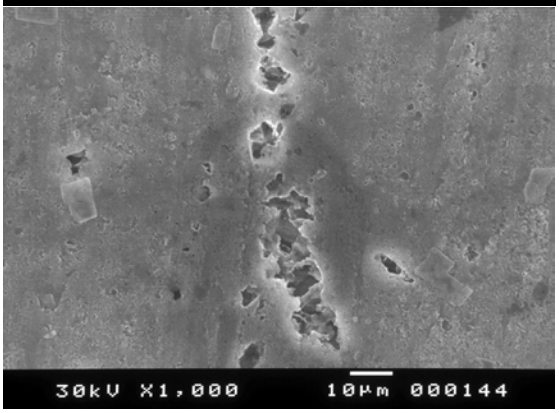

(b)

(e)

Fig. 4.38 :SEM topographies of alloy 2024-T351 after aging for 2 h at T=170^{o}C and 2 h exposure in the EXCO solution. Magnification is (a) x200, (b) x500 and (c) x1000 respectively .

6 hours aging

In Fig 4.39 pitting is the main corrosion mechanism with several pits forming larger groups. The corrosion mechanism is similar with 1h of aging.

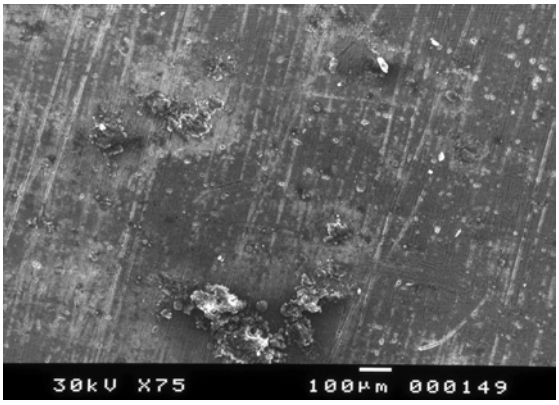

(a)

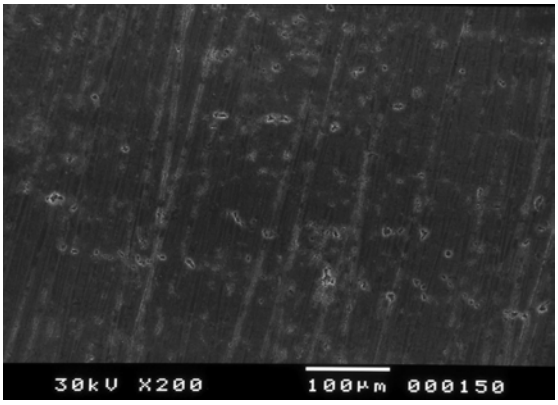

(d)

Fig. 4.39 : SEM topographies of alloy 2024-T351 after aging for 6 h at T=170°C and 2 hours exposure in the EXCO solution. Magnification is (a)x100 and (b) x200respectively.

9 hours aging

In Fig 4.40 there are some areas were pitting is the main corrosion mechanism but mainly a more severe attack is present. Pits have connected along intergranular paths.

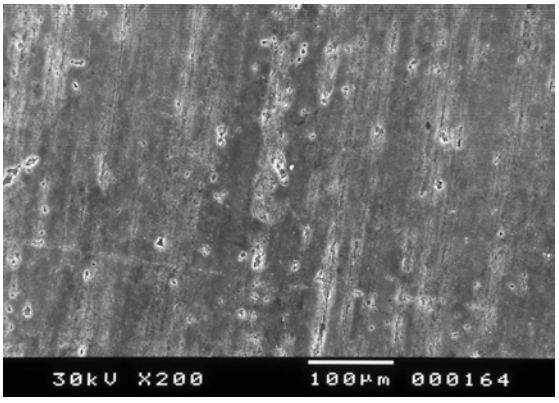

(a)

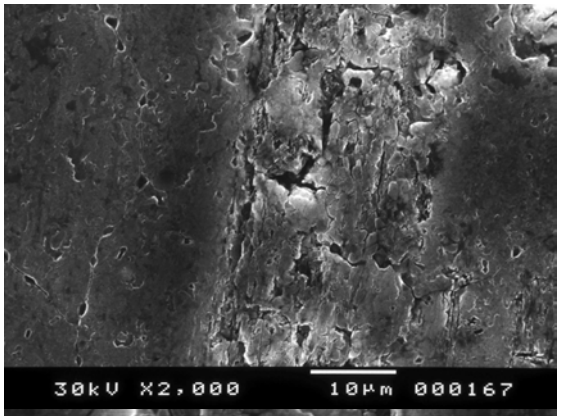

(d)

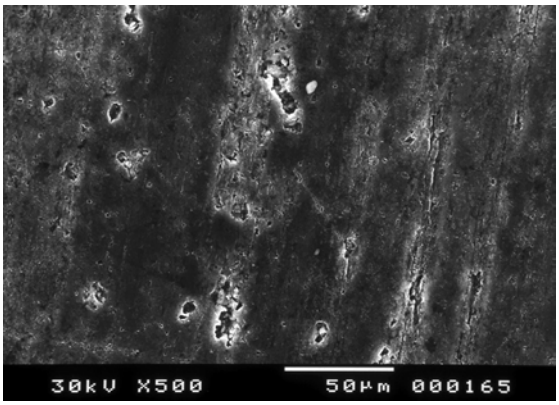

(b)

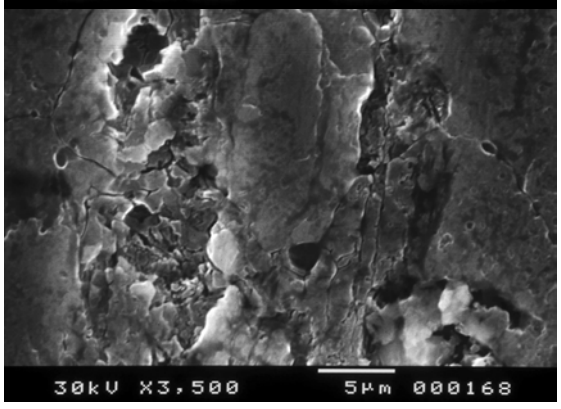

(e)

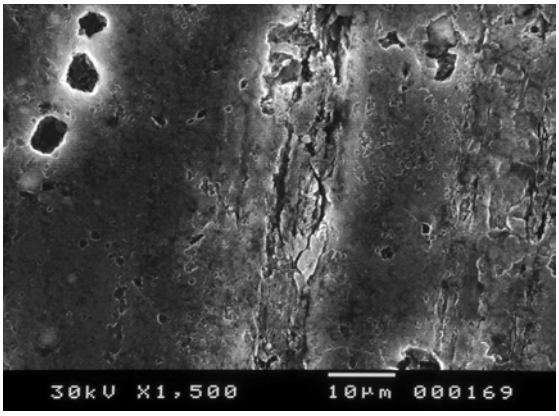

(c)

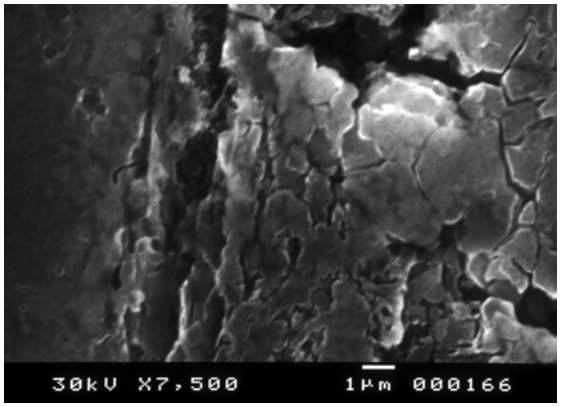

(f)

Fig. 4.40: SEM topographies of alloy 2024-T351 after aging for 9 h at T=170°C and 2 hours exposure in the EXCO solution. Magnification is x200, x500, x1500, x2000, x3500 and x7500 respectively.

15 hours aging

In Fig 4.41 a more severe attack is present. Pits have connected along intergranular paths.

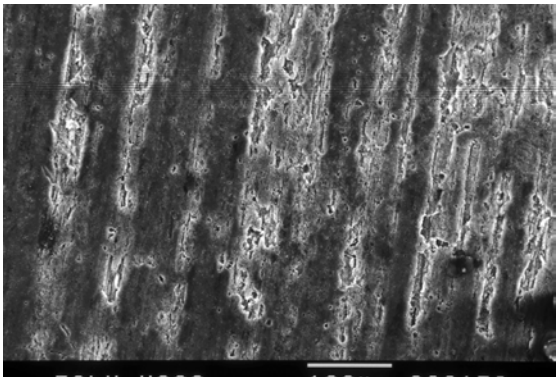

(a)

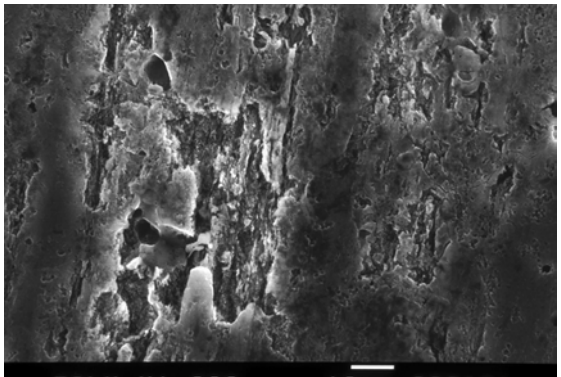

(d)

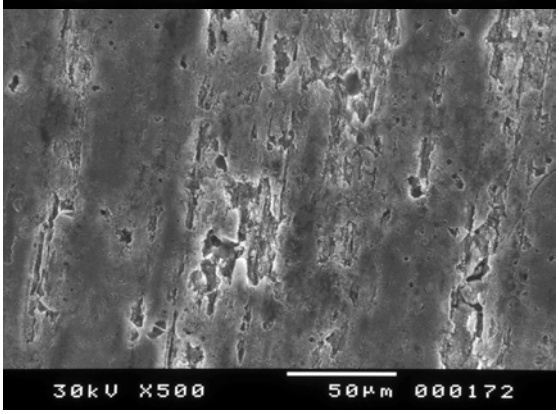

(b)

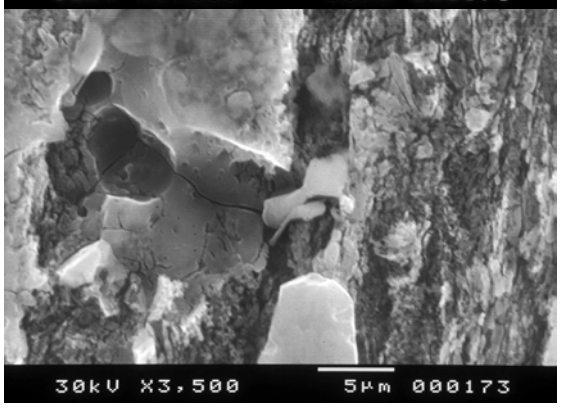

(e)

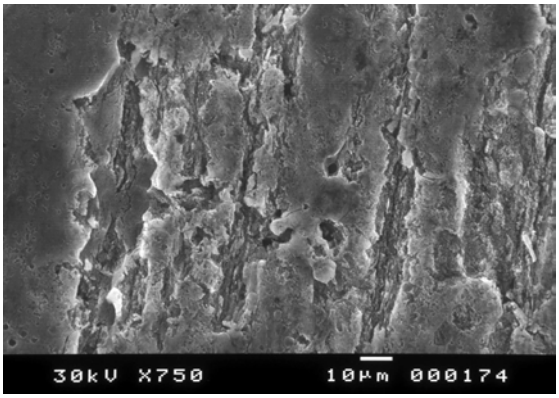

(c) (f)

Fig. 4.41: SEM topographies of alloy 2024-T351 after aging for 15 h at T=170°C and 2 hours exposure in the EXCO solution. Magnification is x200, x500, x750, x1000 and x3500 respectively.

24 hours aging

In Fig 4.42 severe overall attack is present.

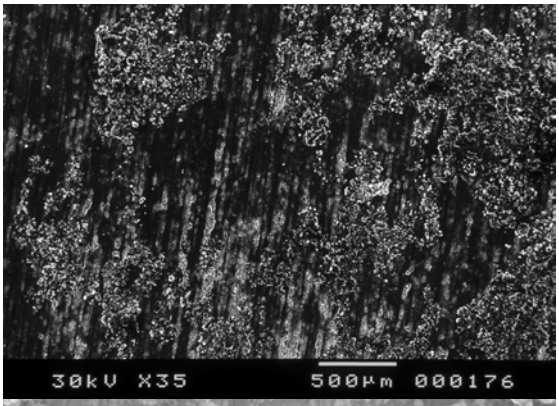

(a)

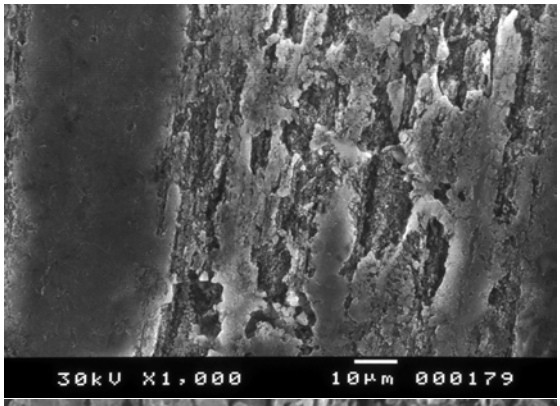

(d)

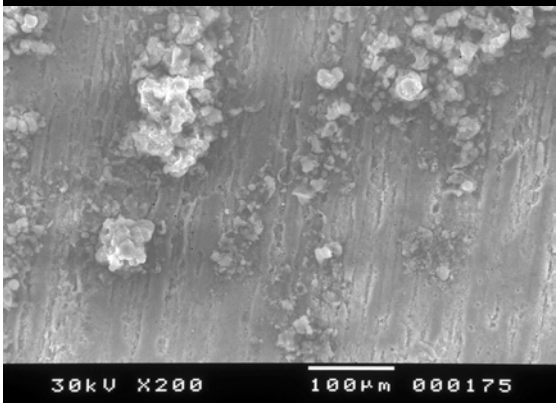

(b)

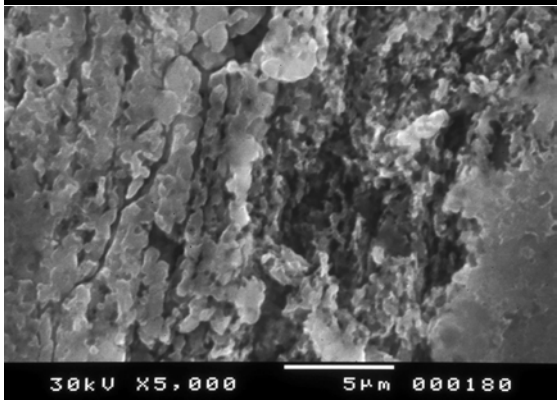

(e)

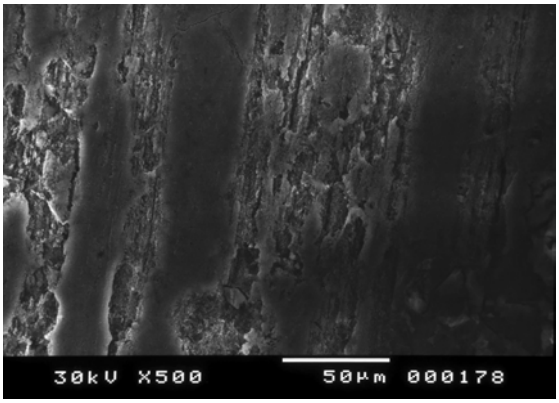

(c)

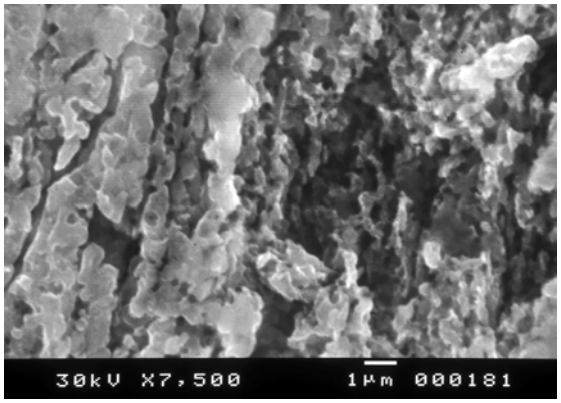

(f)

Fig. 4.42 : SEM topographies of alloy 2024-T351 after aging for 15 h at T=170°C and 2 hours exposure in the EXCO solution. Magnification is (a) x35, (b) x200, (c) x500, (d) x1000, (e) x5000 and (f) x7500 respectively.

48 hours aging

In Fig 4.43 severe overall attack is present.

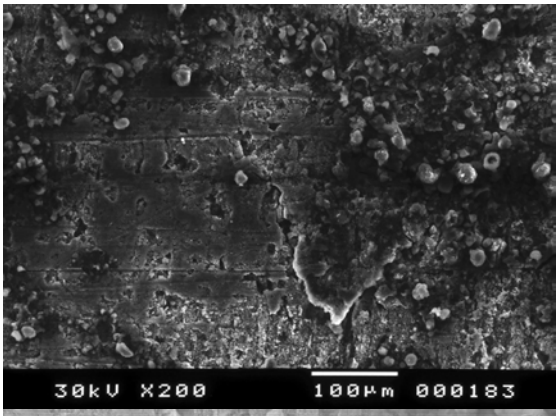

(a)

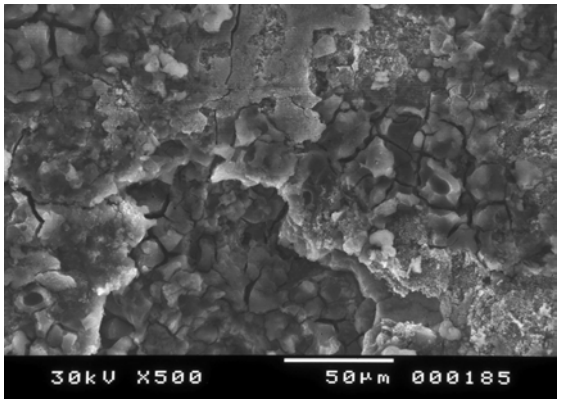

(c)

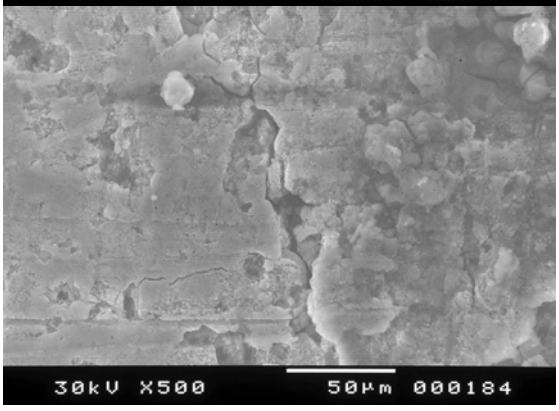

(b)

Fig. 4.43: SEM topographies of alloy 2024-T351 after aging for 48 h at T=170°C and 2 hours exposure in the EXCO solution. Magnification is (a) x200, (b) and (c) x500 respectively.

63 hours aging

In Fig 4.44 severe overall attack is present.

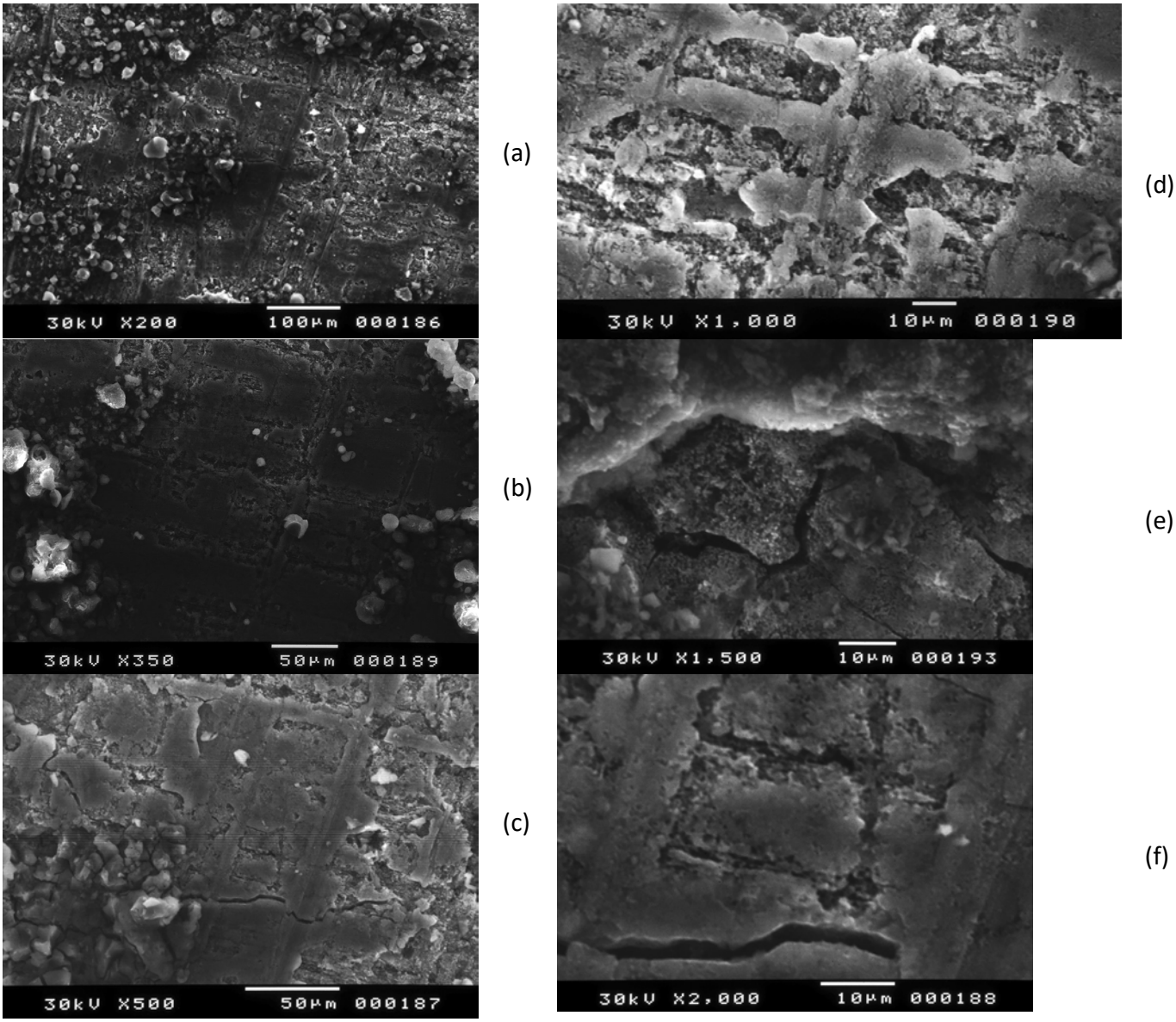

Fig. 4.44: SEM topographies of alloy 2024-T351 after aging for 63 h at T=170^{o}C and 2 hours exposure in the EXCO solution. Magnification is (a) x200, (b) x350, (c) x500, (d) x1000, (e) x1500 and (f) x2000 respectively.

98 hours aging

In Fig 4.45 severe overall attack is present.

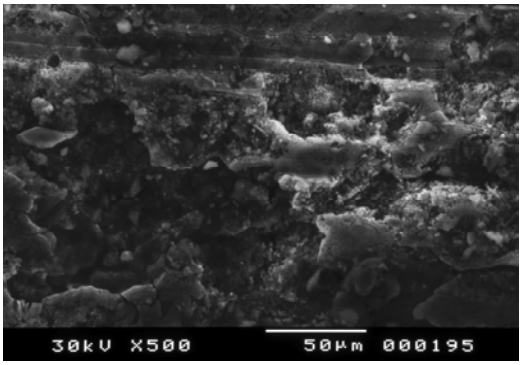

(a)

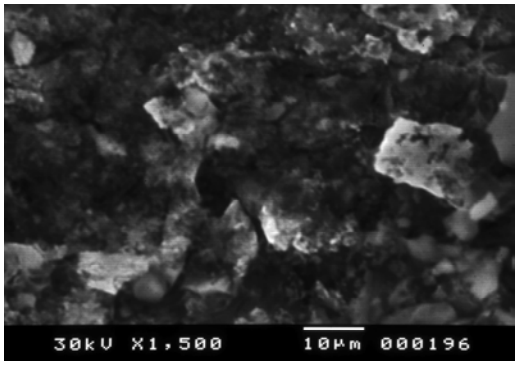

(d)

Fig. 4.45: SEM topographies of alloy 2024-T351 after aging for 98 h at T=170^{o}C and 2 hours exposure in the EXCO solution. Magnification is (a) x500 and (b) x1500 respectively.

Corrosion Exposure 24 Hours

30 min aging

In Fig 4.46 pitting is the main corrosion mechanism with several pits forming groups.

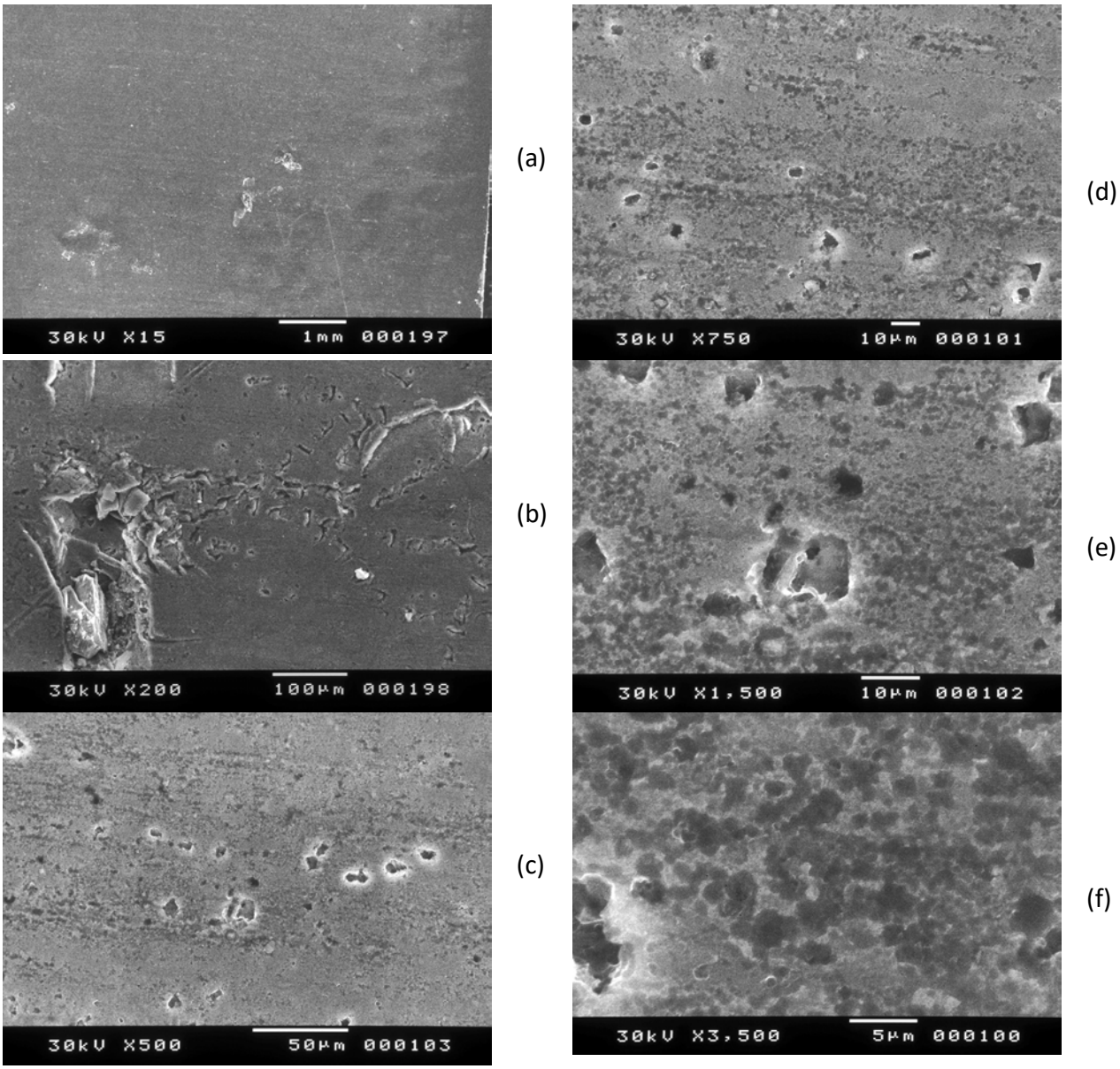

Fig. 4.46: SEM topographies of alloy 2024-T351 after aging for 30 min at T=170°C and 24 hours exposure in the EXCO solution. Magnification is (a) x15, (b) x200, (c) x500, (d) x750, (e) x1500 and (f) x3500 respectively.

1 hour aging

In Fig 4.47 there are some areas were pitting is the main corrosion mechanism but mainly a more severe attack is present. Pits have connected along intergranular paths.

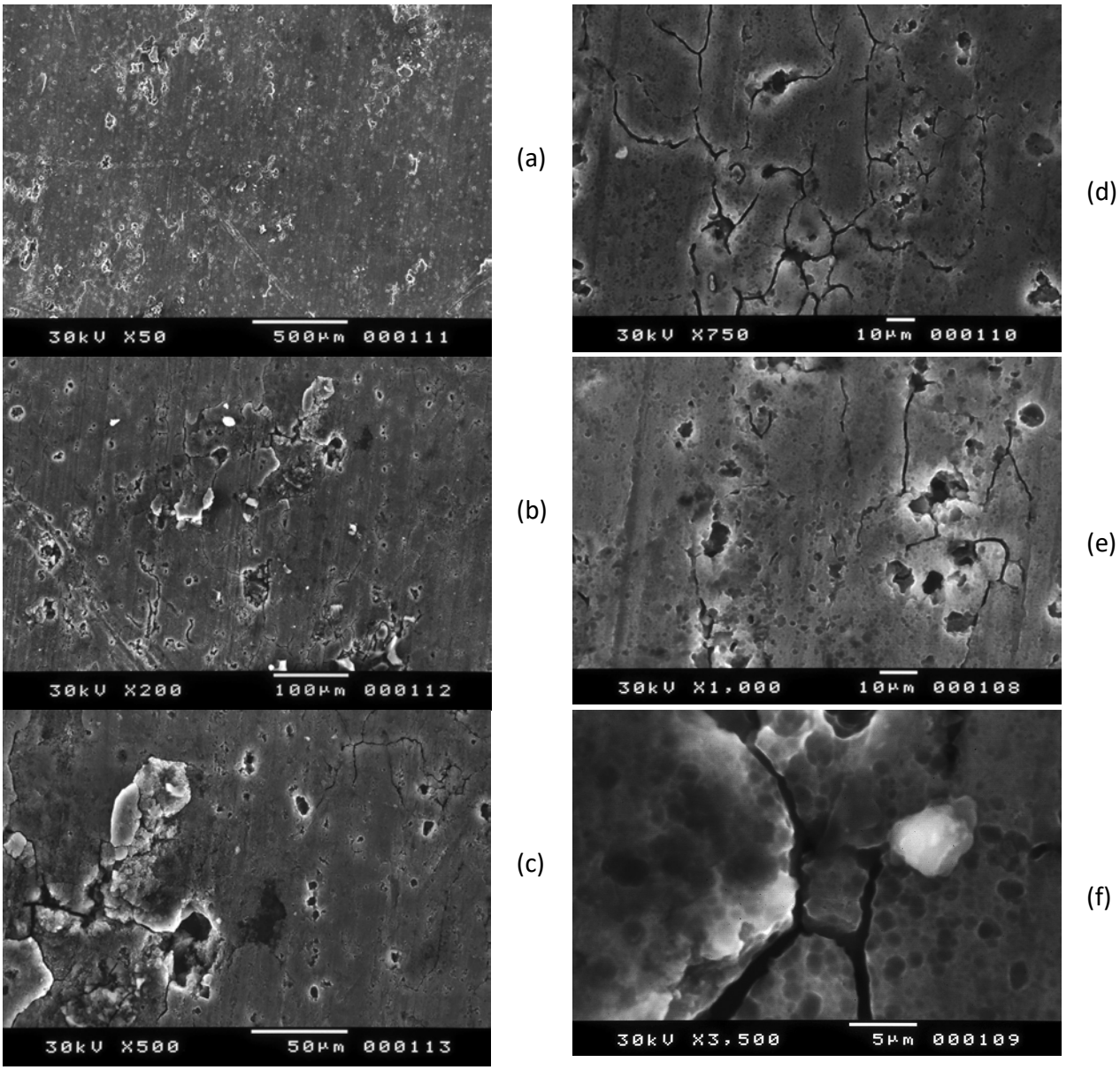

Fig. 4.47: SEM topographies of alloy 2024-T351 after aging for 1 h at T=170^{o}C and 24 hours exposure in the EXCO solution. Magnification is (a) x50, (b) x200, (c) x500, (d) x750, (e) x1000 and (f) x3500 respectively.

2 hours aging

In Fig 4.48 there are some areas were pitting is the main corrosion mechanism but mainly a more severe attack is present. Pits have connected along intergranular paths.

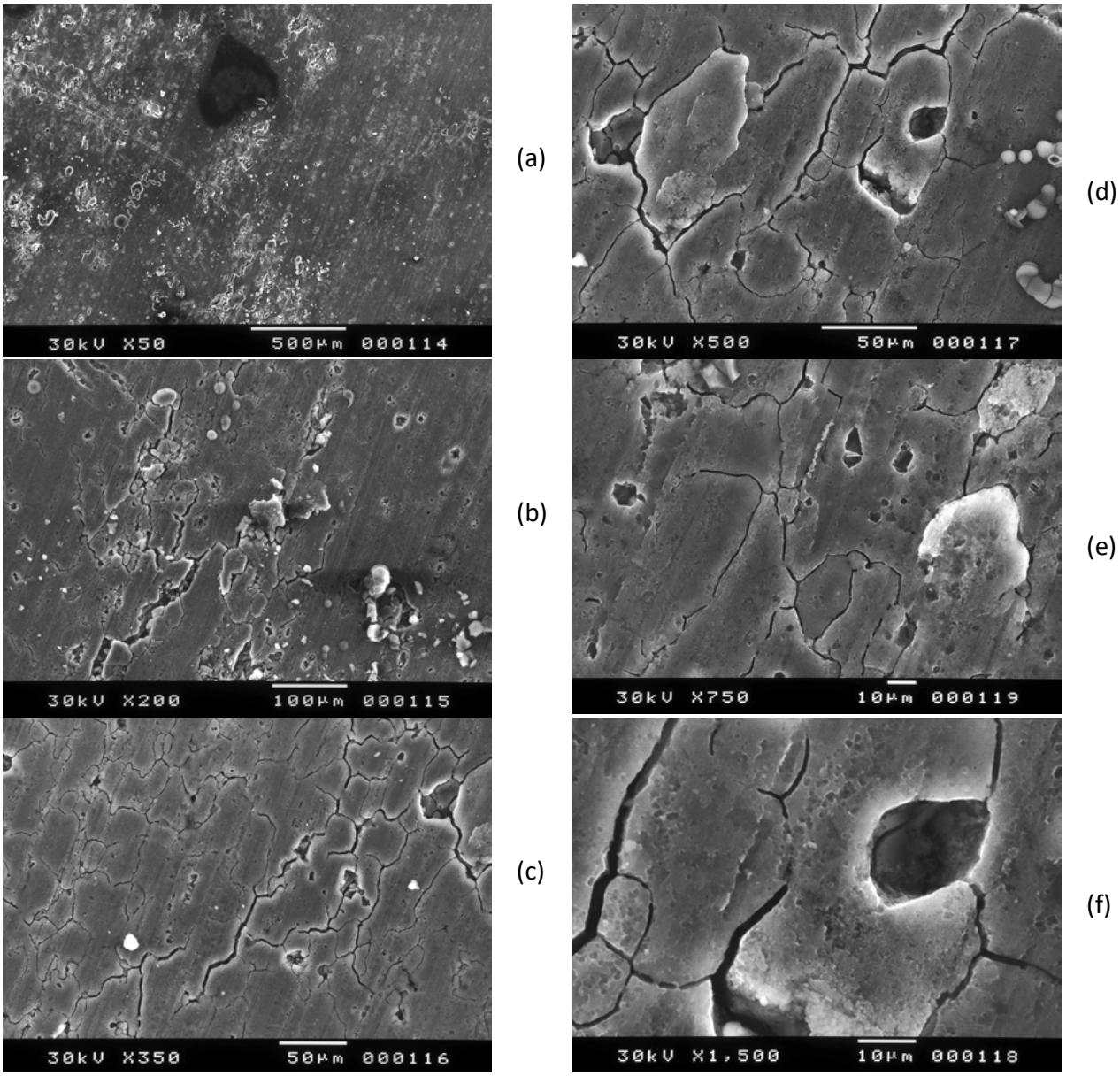

Fig. 4.48: SEM topographies of alloy 2024-T351 after aging for 2 h at T=170°C and 24 hours exposure in the EXCO solution. Magnification is (a) x50, (b) x200, (c) x350, (d) x500, (e) x750 and (f) x1500 respectively.

4 hours aging

In Fig 4.49 the main corrosion mechanism is intergranular corrosion.

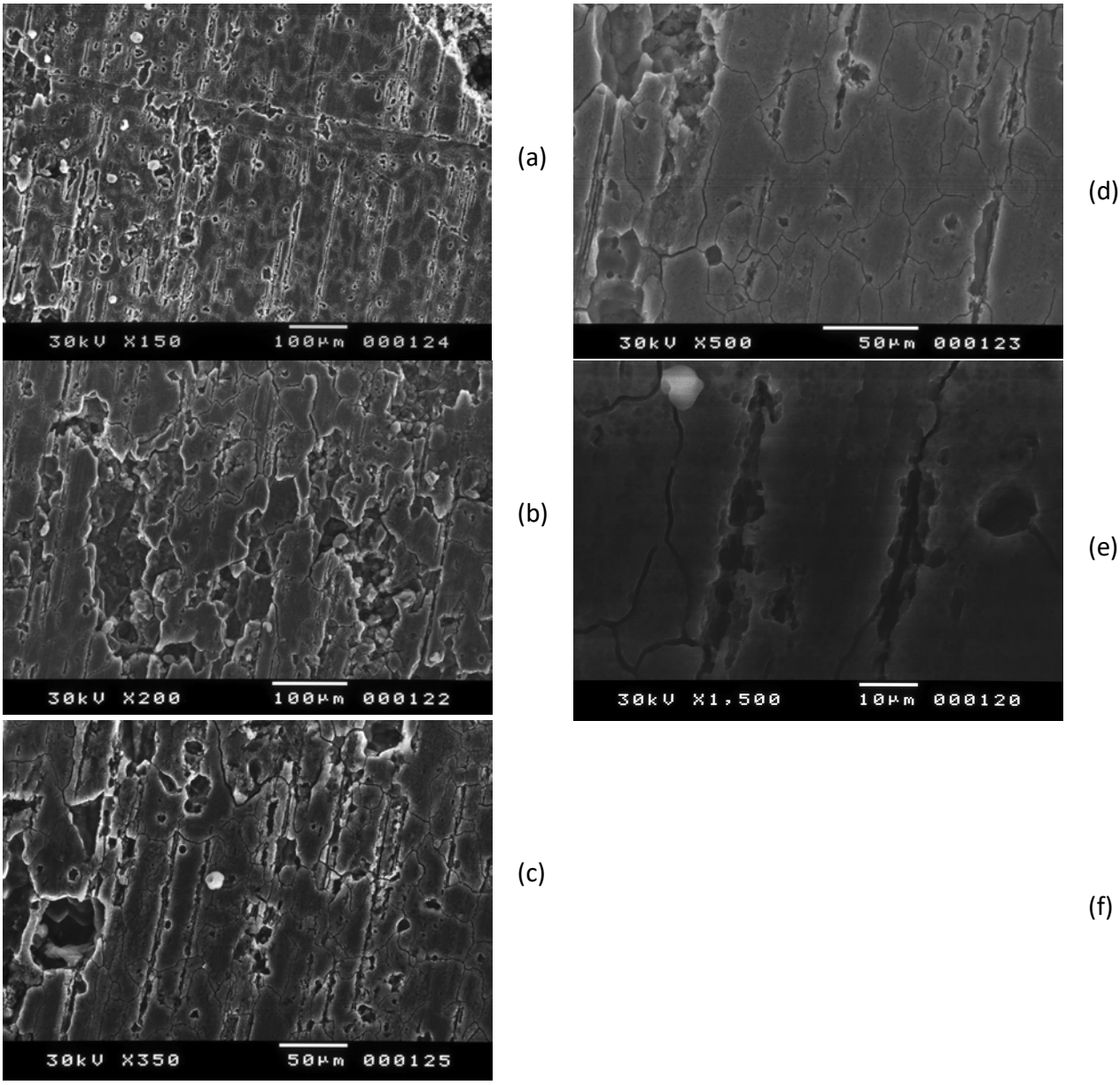

Fig. 4.49: SEM topographies of alloy 2024-T351 after aging for 4 h at T=170^{o}C and 24 hours exposure in the EXCO solution. Magnification is (a) x150, (b) x200, (c) x350,(d) x500 and (e) 1500 respectively.

With the increase in aging time the corrosion mechanism changes from pitting to intergranular corrosion and finally exfoliation.

4.6 Microhardness measurements

Specimens of dimensions 5x10mm^2 were cut out of 2024 plate. The small size of the specimen was necessary for the uniform transport of heat into the sample during thermal treatment.

First, the specimens were surface-cleaned with alcohol according to ASTM G1 and then were heat treated. The specimens were artificially aged, after solid solution at 490^{o}C for **30 min**, at 170 ^{o}C, in an electric oven with ±5 ^{o}C temperature control. The aging times were: 30 min, 1 h, 2 h, 4 h,6 h, 9 h, 15 h , 24 h, 48 h, 63 h and 98 hours.

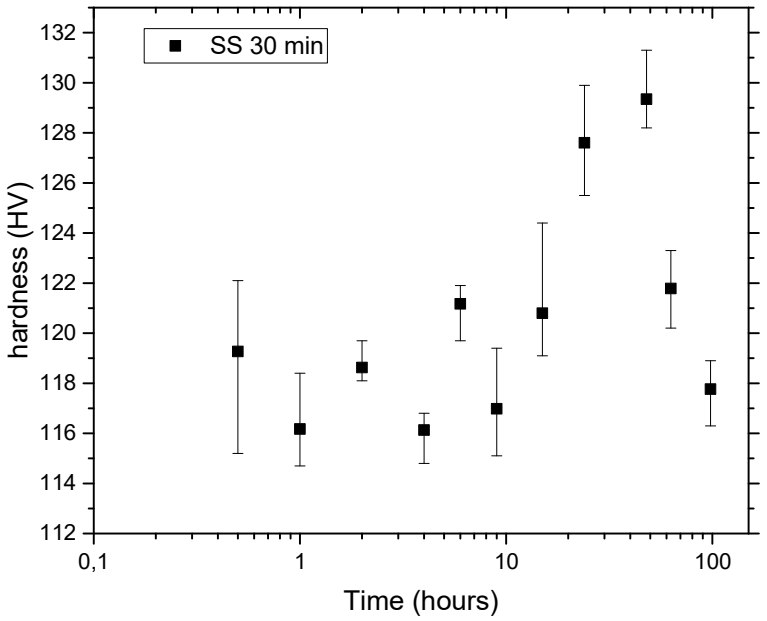

Fig. 4.50: Microhardness profile of 2024-T351 versus time of aging. The aging was performed at T=170^{o}C for duration of 30 min, 1 h, 2 h, 4 h,6 h, 9 h, 15 h , 24 h, 48 h, 63 h and 98 respectively.

The study of artificial aging for alloy 2024 (Fig 4.50) revealed that after solid solution and aging at 170^{o}C the maximum microhardness of the alloy is reached after aging between 24 and 48 hours. A less prominent peak is also apparent after 6h of aging.

Alexopoulos et al. (85) performed mechanical testing on similarly aged aluminum alloy 2024 they measure yield strength and elongation to fracture for aging at 170^{o}C for 9 h, 15 h , 24 h, 48 h, 63 h and 98. Their results are plotted in the figure below along with the microhardness measurements of this thesis. It is evident that the microhardness measurements are in accordance with the mechanical properties. Yield strength is maximized between 24 and 48 hours of aging, while elongation to fracture present a minimum for the corresponding times.

This is attributed to coherent and semi-coherent particles of S'' and S' phases that are present at small aging times. As aging time progresses the particles increase in size, thus increasing the hardness of the material due to coherency hardening. After the peak S'' and S' phases are no longer present as they are gradually replaced by the incoherent S phase, the interfaces loose coherency. The hardness drops and follows Orowan-mechanism as S phase increases in size.

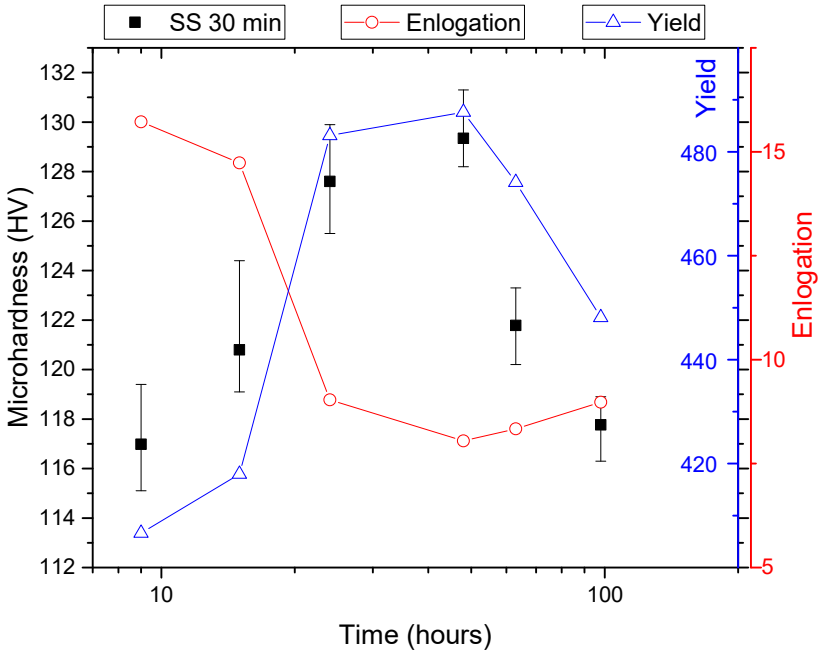

Fig. 4.51: Microhardness profile of 2024-T351 versus time of aging. The aging was performed at T=170°C for duration of 30 min, 1 h, 2 h, 4 h,6 h, 9 h, 15 h , 24 h, 48 h, 63 h and 98 respectively.

4.7 Hydrogen measurements

A main part of this thesis consists of the determination of hydrogen concentration and it's trapping states in the material after corrosion. The determination of these states was conducted by using a thermal desorption technique.

The results reported in the next section are presented as hydrogen mass flow rate (in μg/min) versus specimen temperature. If the heating rate is sufficiently low, each trapping site produces an independent peak. The temperature of the onset of peak growth is characteristic of the energy needed to release hydrogen from the respective trapping site. Thus, low temperature peaks are related to weakly bonded hydrogen and high temperature peaks to strongly bonded

hydrogen. Calculation of the total hydrogen quantity in each trapping site is performed by integrating the area under the respective peak.

Experiments concerning hydrogen desorption from alloy 2024-T351 after exposure to the EXCO corrosive solution for the duration of 12, 24, 48 and 72 hours, were performed and the results are presented in the figure below. In accordance with previous work four distinct trapping states are observed.

Hydrogen is produced during the corrosion process and is being trapped in distinct energy states, which correspond to different microstructural traps. These traps are activated and liberate hydrogen at different temperatures. In alloy 2024, four traps T1 to T4 were identified. Trap T1 is considered to be a reversible trap, which liberates hydrogen continuously at low temperatures. Traps T2, T3 and T4 saturate with exposure time and are considered to be irreversible.

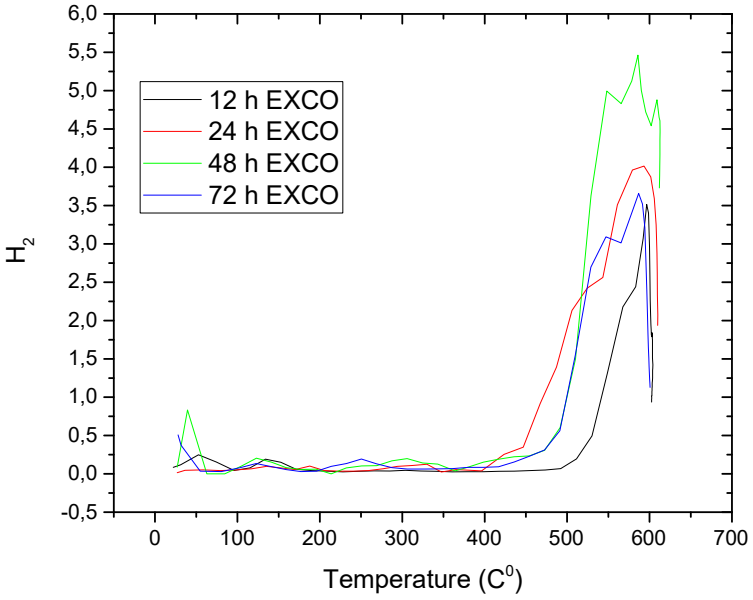

Fig. 52 : Spectrum of hydrogen evolved from the specimens in the T351 condition after (a) 12 h (b)24 h, (c) 48 h and (d) 72 h exposure to the EXCO solution.

As exposure time to the corrosive solution is increases so does the hydrogen trapped in each state up to 48h of exposure. For 72 h of exposure less hydrogen is trapped in the material, this is attributed to the loss of material for the high exposure time.

Hydrogen measurements were performed for specimen subjected to artificial aging as described in the previous chapter. Hydrogen absorption behavior is similar as in the case of

plane 2024-T351 aluminum alloy exposed to the EXCO solution. Hydrogen is produced during the corrosion process and is being trapped in distinct energy states, which correspond to different microstructural traps. These traps are activated and liberate hydrogen at different temperatures. The same four traps T1 to T4 were identified.

The major difference as made evident by the following figure is that with different aging times the resulting spectrum of hydrogen changes. As aging time increases there is an increase in the hydrogen trapped in the material. Different trapping states trap hydrogen in a different manner, thus giving evidence for microstructural characteristic connected with the respective trap.

Trapping state T1 corresponds to hydrogen at interstitial sites. While trapping state T4 which is the strongest trap and its temperature range corresponds to the dissolution of the strengthening precipitate in alloy 2024, is associated with S particles.

The behavior of the T2 trapping state is connected to the peak hardness of the materials. Hydrogen is attracted to the strain fields associated with coherent and semi-coherent interfaces. As the particle size increases with aging time, the hardness increases due to coherency hardening, at the same time H_2 increases. After the peak, the interfaces loose coherency and the strain fields diminish. The hardness drops and follows Orowan-mechanism. At the same time, H_2 drops since H2 is absorbed to the T4 state.

It has been discussed in previous work that, T3 is associated with dislocation. Coherent / semicoherent interfaces are made up of dislocation arrays. As the particle size increases with aging time, the density of interfacial dislocation increases leading to increase in H2 with aging time. After the peak, the coherency is lost and the density of interfacial dislocation is reduced leading to a reduction of trapping hydrogen.

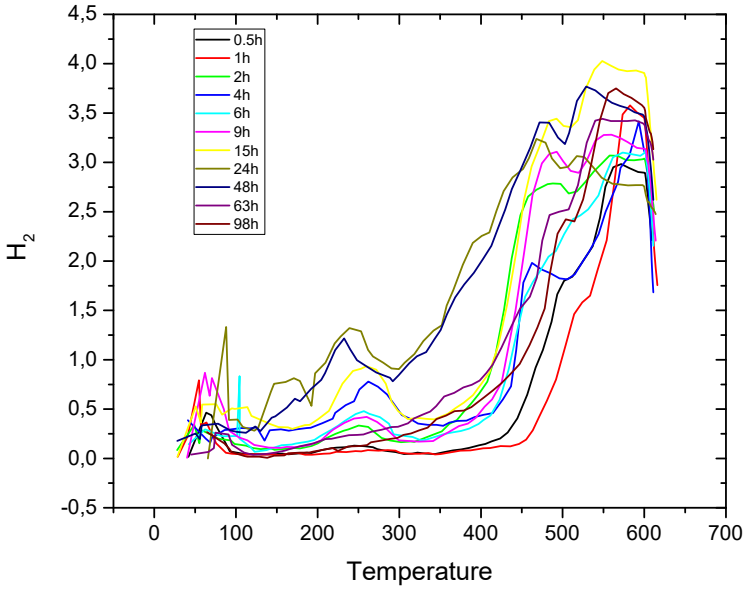

Fig. 53: Spectrum of hydrogen evolved from the solution treated, quenched and aged (SQA) specimens after 24 h in the EXCO solution. The specimens were artificially aged for 30 min, 1 h, 2 h, 4 h, 6 h, 9 h, 15 h , 24 h, 48 h, 63 h and 98 respectively.

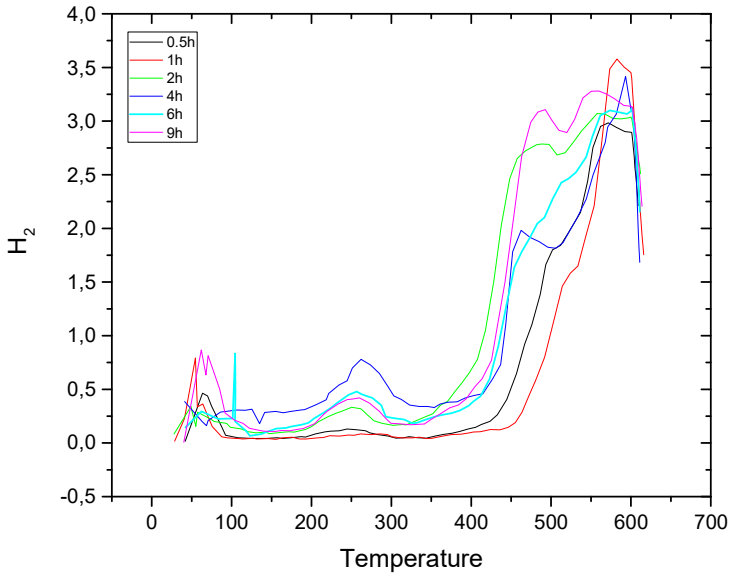

Fig. 54: Spectrum of hydrogen evolved from the solution treated, quenched and aged (SQA) specimens after 24 h in the EXCO solution. The specimens were artificially aged for 30 min, 1 h, 2 h, 4 h, 6 h, 9 h respectively.

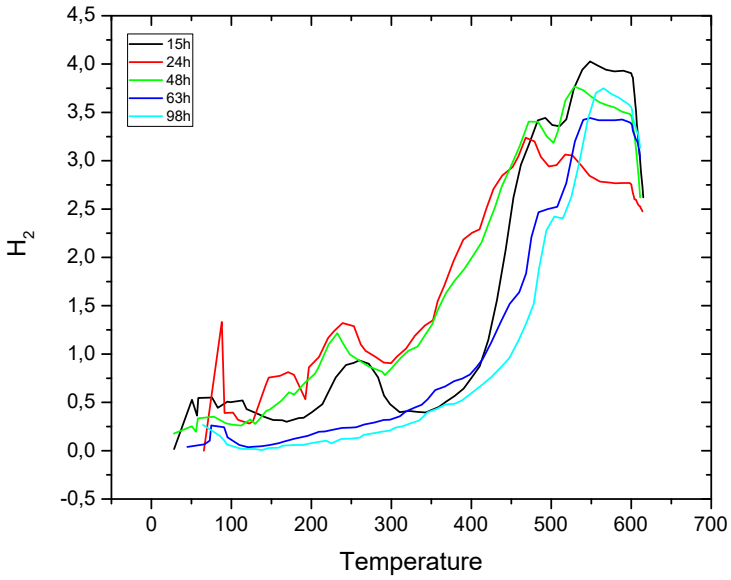

Fig. 55: Spectrum of hydrogen evolved from the solution treated, quenched and aged (SQA) specimens after 24 h in the EXCO solution. The specimens were artificially aged for 15 h, 24 h, 48 h, 63 h and 98 respectively.

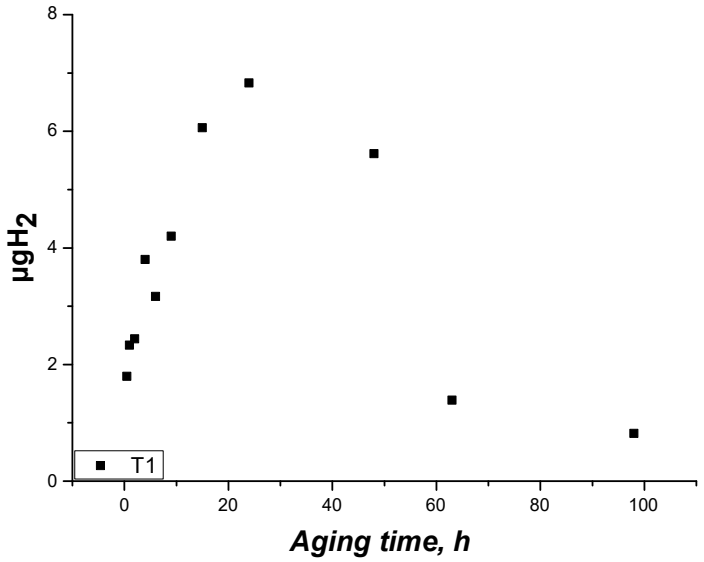

Fig. 56: Total hydrogen content of corroded specimens in the T1 trapping state as a function of aging time (24 hours in the exfoliation solution).

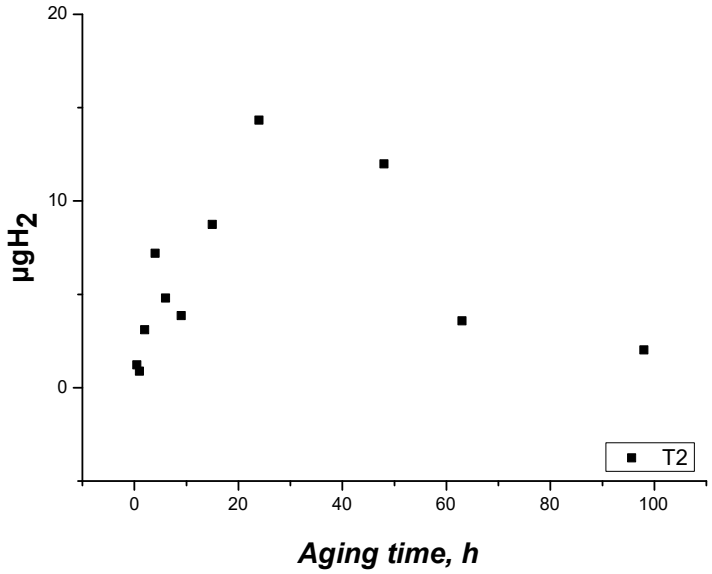

Fig. 57: Total hydrogen content of corroded specimens in the T2 trapping state as a function of aging time (24 hours in the exfoliation solution).

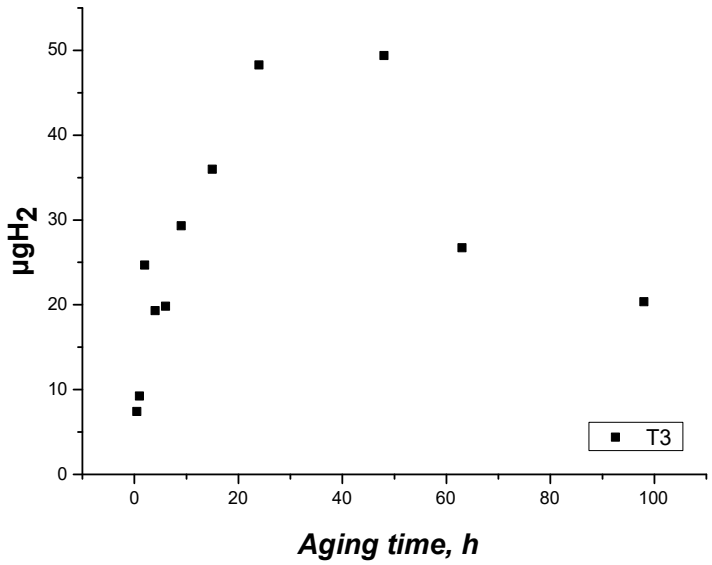

Fig. 58: Total hydrogen content of corroded specimens in the T3 trapping state as a function of aging time (24 hours in the exfoliation solution).

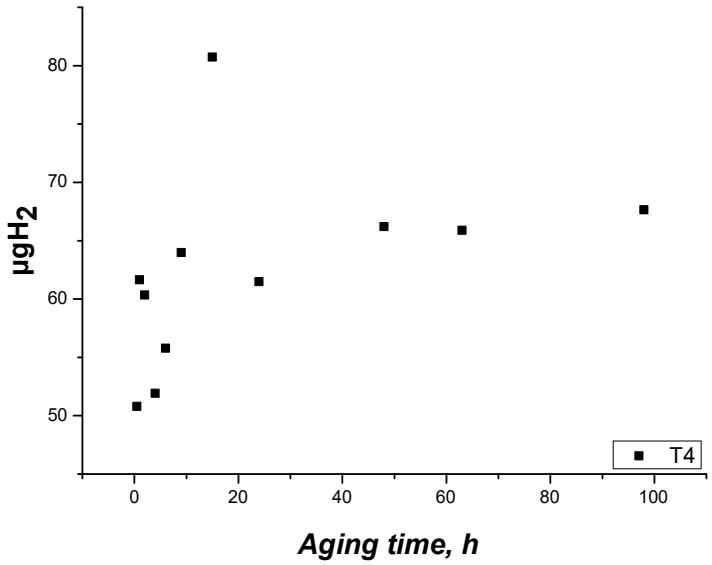

Fig. 59: Total hydrogen content of corroded specimens in the T4 trapping state as a function of aging time (24 hours in the exfoliation solution).

Chapter 5 - Conclusions

Several conclusions were reached after the analysis of results and the discussion in the previous chapter regarding corrosion-induced hydrogen embrittlement in Al-alloy 2024-T351:

1. Exposure to the corrosive solution results in more severe attack as exposure time to EXCO progresses. The same effect is observed with the increase of aging time at a stable time of exposure (2 or 24 hours). As the aging time increases the effect on the mechanism of corrosion changes and from pitting for aging up to 4hours it transforms to exfoliation corrosion for aging over 6 to 9 hours.

2. Corrosion damage in the alloy starts with pitting and develops to a network of intergranular corrosion leading to exfoliation of material. Pit-to-pit interaction and pit clustering are mechanisms aiding the development of corrosion damage. The depth of attack increases with exposure time.

3. Experiments concerning hydrogen desorption from alloy 2024-T351 after exposure to the EXCO corrosive solution for the duration of 12, 24, 48 and 72 hours, were in accordance with previous work and the results are reproducible. Hydrogen is produced during the corrosion process and is being trapped in distinct energy states, which correspond to different microstructural traps. These traps are activated and liberate hydrogen at different temperatures. In alloy 2024, four traps T1 to T4 were identified. Trap T1 is considered to be a reversible trap, which liberates hydrogen continuously at low temperatures. Traps T2, T3 and T4 saturate with exposure time and are considered to be irreversible.

4. The study of artificial aging for alloy 2024 revealed that after solid solution and aging at 170^{o}C the maximum peak for the mechanical properties (microhardness, yield) of the alloy is reached after aging between 24 and 48 hours. A less prominent peak is also apparent after 6h of aging.

5. Trapping state T1 corresponds to hydrogen at interstitial sites. Trapping state T4 is the strongest trap and its temperature range corresponds to the dissolution of the strengthening precipitate in alloy 2024.

6. The behavior of the T2 trapping state is connected to the peak hardness of the materials. Hydrogen is attracted to the strain fields associated with coherent and semi-coherent interfaces. As the particle size increases with aging time, the hardness increases due to coherency hardening, at the same time H_2 increases. After the peak, the interfaces loose coherency and the strain fields diminish. The hardness drops and follows Orowan-mechanism. At the same time, H_2 drops since H2 is absorbed to the T4 state.

7. It has been discussed in previous work that, T3 is associated with dislocation. Coherent / semicoherent interfaces are made up of dislocation arrays. As the particle size increases with aging time, the density of interfacial dislocation increases leading to increase in H2 with aging time. After the peak, the coherency is lost and the density of interfacial dislocation is reduced leading to a reduction of trapping hydrogen.

Chapter 6 – Proposed Future Work

Taking into consideration the conclusions reached with this thesis the following items are proposed for further investigation:

1. Corrosion-induced hydrogen embrittlement study of the same artificial aging treatment studied in the present work for 2h EXCO exposure.

2. Corrosion-induced hydrogen embrittlement study of aging heat-treatments, for example aging at 190^{o}C or 210^{o}C, which would result in different precipitate combinations.

3. Corrosion-induced hydrogen embrittlement study of other heat-treatable Al-alloys of the 6xxx and 7xxx series

4. Hydrogen embrittlement study using a more mild accelerated corrosion test procedure, such as cathodic charging.

References

1. AGARD Workshop. Corfu, Greece, 1998, 5-9 October.
2. BRITE / EURAM No. 1053. In *ICAF '99 Conference*. Bellevue, WA, 1999.
3. FAA-NASA. Atlanta, Georgia, 1996; F.C.o.E.i.C.M.o.A. Structures,Eds.; National Technical Information Service, Springfield.
4. Chang, J.B.; Szamossi, M.; Lin, K.W., *Methods and Models for Predicting Fatigue Crack Growth under Random Loading*, in *ASTM STP 748*, ASTM, Editor. 1981: Philadelphia. p. 115.
5. Zhang, X.; Chan, A.S.L.; Davis, G.A.O. Eng. Mech., **1992,** *42*, 305.
6. Sih, G.C.; Jeong, D.Y. *Fatigue load sequence effect ranked by critical available energy density.* J. Theor. Appl. Fract. Mech, **1990,** *14*, 141-151.
7. Pantelakis, S.G.; Kermanidis, A.T.; Daglaras, P.G. *Crack-growth analysis code for assessing fatigue life of 2219-T851 aluminum specimens under aircraft structure service spectra.* J. Theor. Appl. Fract. Mech., **1997,** *28*, 1-12.
8. Speidel, M.O., *Hydrogen embrittlement and stress corrosion cracking of aluminum alloys*, in *Hydrogen Embrittlement and Stress Corrosion Cracking*, R. Gibala and R.F. Heheman, Editors. 1992, ASM: Materials Park, OH,. p. 271-296.
9. De Jong, H.F. *Influence of environmental and temperature on the stress corrosion crack growth rate of aluminum 7075.* Aluminum, **1982,** *58*, 526-531.
10. Inman, M.E.; Kelly, R.G.; Willard, S.A.; Piascik, R.S. In *FAA-NASA Symposium on the Continued Airworthiness of Aircraft Structures*. Atlanta, Georgia, 1996; National Technical Information Service, Springfield, Virginia:129-146.
11. Pantelakis, S.G.; Vassilas, N.I.; Daglaras, P.G. *Effect of corrosive environment on the mechanical behavior of the advanced Al-Li alloys 2091 and 8090 and the conventional aerospace alloy 2024.* METAL, **1993,** *47*, 135-141.
12. Pantelakis, S.G.; Daglaras, P.G.; Apostolopoulos, C.A. *Tensile and energy density properties of 2024, 6013, 8090 and 2091 aircraft aluminum alloy after corrosion exposure.* J. Theor. Appl. Mech., **2000,** *33*, 117-134.
13. Kamoutsi, H.; Haidemenopoulos, G.N.; Bontozoglou, V.; Pantelakis, S. *Corrosion-induced hydrogen embrittlement in aluminum alloy 2024.* Corrosion Science, **2006,** *48*(5), 1209-1224.
14. Kamoutsi, H.; Haidemenopoulos, G.N.; Bontozoglou, V.; Petroyiannis, P.V.; Pantelakis, S.G. *Hydrogen Trapping: Deformation and Heat Treatment Effects in 2024 Alloy.* **2006**, 1293-1294.
15. Kamoutsi, H.; Haidemenopoulos, G.N.; Bontozoglou, V.; Petroyiannis, P.V.; Pantelakis, S.G. *Effect of prior deformation and heat treatment on the corrosion-induced hydrogen trapping in aluminium alloy 2024.* Corrosion Science, **2014,** *80*, 139-142.
16. Shih, H.-C.; Ho, N.-J.; Huang, J.C. *Precipitaion behaviors in Al-Cu-Mg and 2024 aluminum alloys.* Metallurgical and Materials Transactions A, **1996,** *27A*, 2479-2494.
17. Bigot, A.; Danoix, F.; Auger, P.; Blavette, D.; Menand, A. *3D reconstruction and analysis of GP zones in Al-1.7Cu (at%): A tomographic atom probe investigation.* Applied Surface Science, **1996,** *94/95*, 261-266.
18. Karlik, M.; Jouffrey, B. *High resolution electron microscopy study of Guinier-Preston (GP1) zones in Al-Cu based alloys.* Acta Materialia, **1997,** *45*(8), 3251-3263.
19. Karlik, M.; Jouffrey, B.; Belliot, S. *The copper content of Guinier-Preston (GP1) zones in Al-1.84 at.% Cu alloy.* Acta Materialia, **1998,** *46*(5), 1817-1825.

20. Charai, A.; Walther, T.; Alfonso, C.; Zahra, A.-M.; Zahra, C.Y. *Coexistence of clusters, GPB zones, S''-, S'- and S-phases in an Al-0.9% Cu-1.4% Mg alloy.* Acta Materialia, **2000,** *48*(10), 2751-2764.
21. Radmilovic, V.; Kilaas, R.; Dahmen, U.; Shiflet, G.J. *Structure and morphology of S-phase precipitates in aluminum.* Acta Materialia, **1999,** *47*(15-16), 3987-3997.
22. Ringer, S.P.; Hono, K. *Microstructural evolution and age hardening in Aluminium Alloys; Atom Probe Field-Ion Microscopy and Transmission Electron Microscopy Studies.* Materials Characterization, **2000,** *44*(1-2), 101-131.
23. Ringer, S.P.; Muddle, B.C.; Polmear, I.J. *Effects of cold work on precipitation in Al-Cu-Mg-(Ag) and Al-Cu-Li-(Mg-Ag) alloys.* Metallurgical and Materials Transactions A, **1995,** *26A*, 1659-1671.
24. Skrotzki, B.; Shiflet, G.J.; Starke, E.A., JR. *On the effect of stress on nucleation and growth of precipitates in an Al-Cu-Mg-Ag alloy.* Metallurgical and Materials Transactions A, **1996,** *27A*, 3431-3444.
25. Ringer, S.P.; Hono, K.; Polmear, I.J.; Sakurai, T. *Precipitation processes during the early stages of ageing in Al-Cu-Mg alloys.* Applied Surface Science, **1996,** *94*(95), 253-260.
26. Ringer, S.P.; Polmear, I.J.; Sakurai, T. *Effect of additions of Si and Ag to ternary Al-Cu-Mg alloys in the á+S phase field.* Materials Science & Engineering A, **1996,** *217/218*, 273-276.
27. Ringer, S.P.; Sakurai, T.; Polmear, I.J. *Origins of Hardening in Aged Al-Cu-Mg-(Ag) Alloys.* Acta Materialia, **1997,** *45*(9), 3731-3744.
28. Ringer, S.P.; Quan, G.C.; Sakurai, T. *Solute clustering, segregation and microstructure in high strength low alloy Al-Cu-Mg alloys.* Materials Science & Engineering A, **1998,** *A250*, 120-126.
29. Polmear, I.J., *Light Alloys*. Third ed. Metallurgy and Materials Science Series, ed. R. Honeycombe and P. Hancock. 1995, London: Arnold. 362.
30. Blanc, C.; Lavelle, B.; Mankowski, G. *The role of precipitates enriched with copper on the susceptibility to pitting corrosion of the 2024 aluminium alloy.* Corrosion Science, **1997,** *39*(3), 495-510.
31. Guillaumin, V.; Mankowski, G. *Localized corrosion of 2024 T351 aluminium alloy in chloride media.* Corrosion Science, **1999,** *41*, 421-438.
32. Liao, C.-M.; Olive, J.M.; Gao, M.; Wei, R.P. *In-situ monitoring of pitting corrosion in aluminum alloy 2024.* Corrosion, **1998,** *54*(6), 451-458.
33. ASM, *Corrosion of Aluminum and Aluminum Alloys*, ed. J.R. Davis. 1999: ASM International.
34. Tanguy, D.; Bayle, B.; Dif, R.; Magnin, T. *Hydrogen effects during IGSCC of pure Al-5Mg alloy in NaCl media.* Corrosion Science, **2002,** *44*, 1163-1175.
35. Delafosse, D.; Magnin, T. *Hydrogen induced plasticity in stress corrosion cracking of engineering systems.* Eng. Fract. Mech, **2001,** *68*, 693-729.
36. Braun, R. *Comparison of accelerated SCC tests performed on the aluminium alloy 2014-T651.* Werkstoffe und Korrosion, **1992,** *43*, 453-458.
37. Braun, R. *Investigation of the SCC Behaviour of alloy 2024 using the slow strain rate technique.* Werkstoffe und Korrosion, **1993,** *44*, 73-82.
38. Braun, R. *Slow strain rate testing of high-strength aluminium alloy plate in an aqueous solution of 3% NaCl +0.3% H 2 O 2.* Werkstoffe und Korrosion, **1994,** *45*, 369-377.
39. Braun, R. In *Aluminium Alloys- Their physical and mechanical properties*. Atlanta, 1994; T.H. Sanders and E.A. Starke,Eds.
40. Braun, R. *Slow strain rate testing of aluminum alloy 7050 in different tempers using various synthetic enviroments.* Corrosion, **1997,** *53*(6), 467-474.
41. Braun, R. *Exfoliation corrosion testing of aluminium alloys.* British Corrosion Journal, **1995,** *30*(3).
42. Braun, R. Seville, Spain, 1994.
43. *ASTM G34-90*, in *Annual Book of ASTM Standards*, ASTM, Editor. 1994. p. 129.

44. Revie, R.W.; Sastri, V.S.; Hoey, G.R.; Ramsingh, R.R.; Mak, D.K.; Shehata, M.T. *Hydrogen-induced cracking of linepipe steels Part 1-threshold hydrogen concentration and pH.* Corrosion, **1993,** *49*(1), 17-23.
45. Chu, W.Y.; Huang, C.H.; Wang, Y.B.; Qiao, L.J. *Hydrogen embrittlement of rail steels.* Corrosion, **1999,** *55*(9), 892-897.
46. Symons, D.M. *The effect of hydrogen on the fracture toughness of alloy X-750 at elevated temperatures.* Journal of Nuclear Materials, **1999,** *265*, 225-231.
47. Cantwell, J.E. *High-Temperature hydrogen attack.* Materials Performance, **1994**, 58-61.
48. Nakamura, M.; Gao, K.W. *Hydrogen embrittlement of Ti-49Al at various strain rates.* Intermetallics, **2002,** *10*, 233-238.
49. Al-Anezi, M.A.; Frankel, G.S.; Agrawal, A.K. *Susceptibility of conventional pressure vessel steel to hydrogen-induced cracking and stress oriented hydrogen-induced cracking in hydrogen sulfide-containing diglycolamine solutions.* Corrosion, **1999,** *55*(11), 1101-1109.
50. Sofronis, P.; Robertson, I.M., *Atomistic scale experimental observations and micromechanical/continuum models for the effect of hydrgen on the mechanical behavior of metals*. 2001.
51. Robertson, I.M. *The effect of hydrogen on dislocation dynamics.* Eng. Fract. Mech, **2001,** *68*, 671-692.
52. Sofronis, P.; Robertson, I.M.; Liang, Y.; Teter, D.F.; Aravas, N., *Recent Advances in the study of hydrogen embrittlement at the University of Illinois*. 2001, University of Illinois, Technical Report.
53. Luu, W.C.; Wu, J.K. *Hydrogen transport and enviromental embrittlement effects in iron aluminades.* Journal of Materials Science, **2000,** *35*, 4121-4127.
54. Luu, W.C.; Kuo, H.S.; Wu, J.K. *Hydrogen permeation through nickel-plated steels.* Corrosion Science, **1997,** *39*(6), 1051-1059.
55. Young, G.A.; Scully, J.R. *Evidence that carbide precipitation produces hydrogen traps in Ni-17Cr-8Fe alloys.* Scripta Materialia, **1997,** *36*(6), 713-719.
56. Au, M.U. *A visible technology for display of hydrogen distribution in metals.* Journal of Alloys and Compounds, **1999,** *293-295*, 317-323.
57. Pressouyre, G.M. *A classification of hydrogen traps in steel.* Materials Transactions A, **1979,** *10A*, 1571-1573.
58. Pressouyre, G.M. *Trap theory of hydrogen embrittlement.* Acta Metallurgica, **1979,** *28*, 895-911.
59. Lee, S.-M.; Lee, J.-Y. *The trapping and transport phenomena of hydrogen in nickel.* Metallurgical Transactions A, **1986,** *17A*, 181-187.
60. Pound, B.G. *The effect of ageing on hydrogen trapping in precipitation- hardened alloys.* Corrosion Science, **2000,** *42*, 1941-1956.
61. Thomas, R.L.S.; Li, D.; Gangloff, R.P.; Scully, J.R. *Trap-governed hydrogen diffusivity and uptake capacity in ultrahigh-strength AERMET 100 steel.* Metallurgical and Materials Transactions A, **2002,** *33A*, 1991-2004.
62. Enos, D.G.; Scully, J.R. *A critical-strain criterion for hydrogen embrittlement of cold-drawn, ultrafine pearlitic steel.* Metallurgical and Materials Transactions A, **2002,** *33A*, 1151-1165.
63. Katano, G.; Ueyama, H.; Mori, M. *Observation of hydrogen distribution in high-strength steel.* Journal of Materials Science, **2001,** *36*, 2277-2286.
64. Eliaz, N.; Shachar, A.; Tal, B.; Eliezer, D. *Characteristics of hydrogen embrittlement, stress corrosion cracking and tempered martensite embrittlement in high-strength steels.* Engineering Failure Analysis, **2002,** *9*, 167-184.
65. Marrow, T.J.; Aindow, M.; Prangnell, P.; Strangwood, M.; Knott, J.F. *Hydrogen-assisted stable crack growth in iron-3wt% silicon steel.* Acta Materialia, **1996,** *44*(8), 3125-3140.

66. Chiang, W.C. *Hydrogen susceptibility of 17-4 Ph stainless steel.* Materials Letters, **2002,** (4186), 1-4.
67. McMahon Jr., C.J. *Hydrogen -induced intergranular fracture of steels.* Eng. Fract. Mech, **2001,** *68*, 773-788.
68. Birnbaum, H.K.; Buckley, C.; Zeides, F.; Sirois, E.; Rozenak, P.; Spooner, S.; Lin, J.S. *Hydrogen in aluminum.* Journal of Alloys and Compounds, **1997,** *253-254*, 260-264.
69. Christodoulou, L.; Flower, H.M. *Hydrogen embrittlement and trapping in Al-6%-Zn-3%-Mg.* Acta Metallurgica, **1980,** *28*, 481-487.
70. Pantelakis, S.G.; Kermanidis, A.T.; Daglaras, P.G.; Apostolopoulos, C.A. The Effect of Existing Corrosion on the Structural Integrity of Aging Aircraft. In *Fatigue in the Presence of Corrosion*. Corfu, Greece, 1998; AGARD Workshop.
71. Kermanidis, A.T., *Åðßäñáóç ôçò äéÜâñùóçò óôçí äïîéêÞ áêåñáéùôçôá åëáöñþí êáôáóêåõþí áðü êñÜìá áëïõìéíßïõ*, in *Department of Mechanichal Engineering and Aeronautics*. 2003, University of Patras: Greece.
72. Scamans, G.M.; Alani, R.; Swann, P.R. *Pre-exposure embrittlement and stress failure in Al-Zn-Mg alloys.* Corrosion Science, **1976,** *16*, 443-459.
73. Scamans, G.M.; Tuck, C.D.S. In *Environment- sensitive fracture of engineering materials*. New York, NY, 1979; A. Foroulis,Eds.; Metallurgical Sociaty AIME:464.
74. Speidel, M.O., *Hydrogen embrittlement and stress corrosion cracking of aluminum alloys*. 1974.
75. Itoh, G.; Koyama, K.; Kanno, M. *Evidence for the transport of impurity hydrogen with gliding dislocation in aluminum.* Scripta Materialia, **1996,** *35*(6), 695-698.
76. Saitoh, H.; Iijima, Y.; Hirano, K. *Behaviour of hydrogen in pure aluminium Al-4 mass% Cu and Al-1 mass% Mg_2Si alloys studied by tritium electron microautoradiography.* Journal of Materials Science, **1994,** *29*, 5739-5744.
77. Young, G.A.; Scully, J.R. *The diffusion and trapping of hydrogen in high purity aluminium.* Acta Materialia, **1998,** *46*(18), 6337-6349.
78. Tuck, C.D.S. In *On the effects of hydrogen on the behaviour of materials*. Wyoming, 1980; Jackson,Eds.;503.
79. Song, R.G.; Tseng, M.K.; Zhang, B.J.; Liu, J.; Jin, Z.H.; Shin, K.S. *Grain boundary segregation and hydrogen-induced fracture in 7050 aluminium alloy.* Acta mater., **1995,** *44*(8), 3241-3248.
80. Jang, W.; Kim, S.; Shin, K. *Hydrogen-assisted deformation and fracture behaviors of Al 8090.* Metallurgical and Materials Transactions A, **2002,** *33A*, 1755-1763.
81. Jang, W.; Kim, S. *Hydrogen-assisted fracture of Al 8090.* Journal of Materials Science Letters, **2000,** *19*, 447-450.
82. Haidemenopoulos, G.N.; Hassiotis, N.; Papapolymerou, G.; Bontozoglou, V. *Hydrogen absorption into aluminium alloy 2024-T3 during exfoliation and alternate immersion testing.* Corrosion, **1998,** *54*(1), 73-78.
83. EPETII/30, *Damage tolerance behavior of corroded aluminum structures*. 1999, General Secretariat for Research and Technology: Greece.
84. Scherer, J.; Mangnussen, O.M.; Ebel, T.; Behm, R.J. *Initial stages of the anodic etching of aluminium foils studied by atomic force microscopy.* Corrosion Science, **1999,** *41*, 35-55.
85. Alexopoulos, N.D.; Velonaki, Z.; Stergiou, C.I.; Kourkoulis, S.K. *The effect of artificial ageing heat treatments on the corrosion-induced hydrogen embrittlement of 2024 (Al–Cu) aluminium alloy.* Corrosion Science, **2016,** *102*, 413-424.